INVESTIGATION OF RESISTIVE GEODESIC ACOUSTIC MODE IN THE EDGE OF STOR-M TOKAMAK

A Thesis Submitted to the

College of Graduate Studies and Research

in Partial Fulfillment of the Requirements

for the Degree of Master of Science

in the Department of Physics and Engineering Physics

University of Saskatchewan

Saskatoon

By

Yue Ding

Permission to Use

In presenting this thesis in partial fulfilment of the requirements for a Postgraduate degree from the University of Saskatchewan, I agree that the Libraries of this University may make it freely available for inspection. I further agree that permission for copying of this thesis in any manner, in whole or in part, for scholarly purposes may be granted by the professor or professors who supervised my thesis work or, in their absence, by the Head of the Department or the Dean of the College in which my thesis work was done. It is understood that any copying or publication or use of this thesis or parts thereof for financial gain shall not be allowed without my written permission. It is also understood that due recognition shall be given to me and to the University of Saskatchewan in any scholarly use which may be made of any material in my thesis.

Requests for permission to copy or to make other use of material in this thesis in whole or part should be addressed to:

Head of the Department of Physics and Engineering Physics
116 Science Place
University of Saskatchewan
Saskatoon, Saskatchewan
Canada
S7N 5E2

Abstract

A new resistive Geodesic Acoustic Mode (GAM) theory is developed by two-fluids analysis and resistive gyro-kinetic formulation in this thesis. An analytical expression is obtained for the resistive GAM frequency. This theory suggests a large collision frequency will prohibit the parallel current in tokamak, which establishes the cross-field charge neutrality condition $\nabla \cdot \mathbf{J}_{\perp} = 0$ for the existence of GAM at the edge plasma of tokamak. Therefore, the resistive GAM theory provides a more plausible explanation to edge GAM phenomena. Various probe arrays are designed and installed in the STOR-M tokamak to search for the poloidal GAM phenomena. A series of experiments were conducted in the L-mode and RMP discharges. The FFT and wavelet analyses indicate the existence of GAM phenomena in STOR-M, and the observed GAM frequencies match the theoretical predication using the resistive GAM model.

Acknowledgements

I would like to express my sincere gratitude to all the people who made this thesis possible.

First of the all, it is difficult to overstate my gratitude to my supervisor, Prof. Akira Hirose. With his enthusiasm, his wisdom, and his great efforts to explain things clearly and simply, he helped to make mathematics fun for me. During all phases of this thesis, he is providing timely guides and sound advices and his demand for excellence is the chief motivation to me forever. Without him this work would not have been possible.

I especially thank Prof. C. Xiao for his insightful suggestions and comments on this research work. His untiring willingness to teach and encourage me made the whole course of this thesis work highly enjoyable. His dedication to high quality experimental plasma physics research has been a great inspiration. I am especially lucky to have Prof. Xiao's help for identifying important research problems and solving technical problems.

I am grateful to Dave McColl for his discussions, instruction, technical experience, and thoughtful supports and kindly solicitude whenever needed. The Physics Machine Shop (Ted Toporowski, Perry Balon, and Blair Chomyshen) deserves a special note of thanks for their assistance with all the hardware of this work.

I am also indebted to Dr. Takumi Onchi and Dr. Mykola Dreval for their expertise and lots of immediate help and suggestions.

I would also like to appreciate my fellow graduate students Michael Hubeny, Yelu Liu, Sayf Gamudi, Kyaw M. Hthu, Kurt Kreuger, Winston Frias, Sepehr Khatir and Sarah Purdy for their constant caring and friendly help in various forms during my research work.

I am grateful to Prof. Chary Rangacharyulu, Chairman, Department of Physics and Engineering Physics, for providing me the opportunity and making the department facilities available. The inspiration, help and suggestions received from Prof. Andrei I. Smolyakov, and all other faculty

members and research scientists are beyond evaluation.

I wish to thank all my friends and relatives around the world for providing a loving enviroment for me throughout my stay in Saskatoon and Canada.

Last but not least, I am forever grateful to my parents for their unconditional support, both financially and emotionally throughout my degree.

This work was supported by the grants from the Natural Sciences and Engineering Research Council of Canada and through financial aid from the University of Saskatchewan Graduate Scholarship and the Dr. Theodore R. Hartz Graduate Scholarship .

This work is dedicated to my parents.

CONTENTS

LIST OF TABLES

LIST OF FIGURES

LIST OF ABBREVIATIONS

Symbol	Definition
a	minor radius
AC	Alternating Current
DC	Direct Current
FFT	Fast Fourier Transform
LHS	Left-hand Side
RHS	Right-hand Side
RMP	Resonant Magnetic Perturbation
$\mathbf{B}$	magnetic field
β	beta factor
c	speed of light
$\mathbf{E}$	electric field
$\mathbf{J}$	plasma current
k	wave number
C_s	ion acoustic speed
k_B	Boltzmann constant
n_e	electron density
n_i	ion density
p	plasma pressure
q	safety factor
Q	fusion energy gain factor
R_0	major radius
$T_e(T_i)$	electron (ion) temperature
τ_E	energy confinement time
ω_D	magnetic drift frequency
ω_*	diamagnetic drift frequency
ω_{Ge}	classical GAM frequency
ω_{GR}	resistive GAM frequency
ν_e	ion-electron collision frequency
ρ	plasma mass density
ρ_s	Larmor radius with electron temperature
$\perp$	cross magnetic field
$\parallel$	along magnetic field

CHAPTER 1

INTRODUCTION

The energy crisis is an important and well-known issue for the generations in the 21st century. Research indicates that current fossil fuels will be consumed out within 100 years with the boosts of industrialization and populations around the world. The rapid deterioration of the environment has caused governments, organizations and institutions to make more efforts in search of solutions. Scientists and engineers are trying different ways to find replacements for fossil fuels, which can be used as sustainable energy resources in the future. Fusion energy is one of the best candidates because it has the following advantages [6]:

(1) It is nearly limitless.

(2) The same weight of fuel can generate much more energy in fusion reactions than in fission reactions.

(3) There is no carbon emissions or other hazardous air pollutants generation.

(4) It is relatively safe with less radioactivity compared to fission energy.

1.1 Fusion Energy

Fusion Energy is the most powerful energy source known to us. It actually powers the Sun and other stars. It is fusion energy that supports life on Earth. From a long term perspective, fusion can provide a large enough scale of energy with vast and widely distributed fuel reserves, and it is a safe energy with low impact on the environment [7]. Scientists and engineers aim to reproduce fusion energy for civilian usage on Earth to benefit society. The related research has been in the progress for over 60 years, since the hydrogen bomb was developed.

1.1.1 Fusion Reaction and Confinement

Fusion is a process whereby light nuclei collide and join together to form a heavier nucleus. When this happens, a large amount of energy arising from the binding energy due to the strong nuclear force gets released. In a fusion reactor, fuels need to be heated to 100 million degrees Celsius. At such extreme temperature, electrons are separated from nuclei, and the fuel gas becomes a plasma - a hot, ionized gas.

The least demanding fusion reaction is the reaction between two hydrogen isotopes: deuterium, extracted from water, and tritium, produced through the interaction between neutron, a fusion reaction product, and lithium in blankets. When deuterium and tritium nuclei fuse, they form a helium nucleus, a neutron and a significant amount of energy (Figure 1.1):

$$ {}^{2}_{1}\mathrm{D} + {}^{3}_{1}\mathrm{T} \rightarrow {}^{4}_{2}\mathrm{He} + {}^{1}_{0}n(+17.6\,\mathrm{MeV}) \tag{1.1} $$

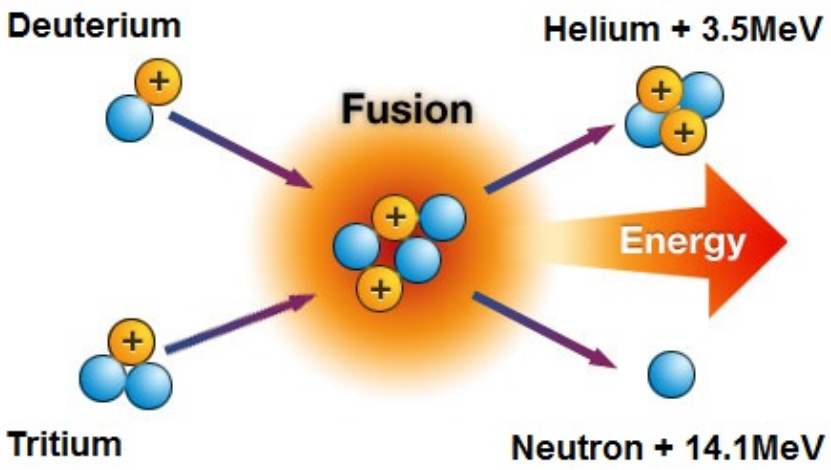

Figure 1.1: Diagram of the D-T reaction

The D-T reaction is considered to be clean and efficient because the generated neutrons can be reused to react with lithium to create more tritium. This strategy also protects the outer portions of the reactor from the neutron flux. The required fuel resources, lithium and water, are abundant on Earth and non-radioactive. The maximum energy outputs from the fusion reaction is over 180 times of uranium fission reaction with the same weight of fuel [8].

The condition of fusion ignition is the "Triple product", which is

$$n_e T \tau_E \geq 10^{21} \text{ keV} \cdot \text{ s/m}^3, \tag{1.2}$$

where n_e is the plasma electron density, T is the plasma temperature, and τ_E is the energy confinement time. Inside the Sun, the fusion reaction is in the form of

$$4^1_1\text{H} + 2\text{e} \rightarrow^4_2 \text{He} + 2\text{neutrinos} + 6\text{photons}(+26 \text{ MeV}) \tag{1.3}$$

This reaction needs temperature as high as about 15 million degrees Celsius to overcome the repulsion of equally charged particles, even under the enormous gravitational pressure environment in the Sun [9]. However, at the much lower pressures (10 billion times less than in the Sun) that we can produce on Earth, the required temperature for D-T fusion reaction is nearly 150 million degrees Celsius [10]. To reach and keep such high temperatures for the fusion, the hot plasma must be kept away from the reactor wall. How to confine such plasma and get continuously stable fusion energy outputs is still a significant scientific and engineering challenge.

At present, two main experimental approaches for fusion are being studied: magnetic confinement and inertial confinement. The first method uses strong magnetic fields to confine the hot plasma which is more highly developed and usually considered more promising for energy production. The second involves compressing a small pellet containing fusion fuel to extremely high densities using strong lasers or particle beams. This method still needs significant research for commercialization. For the magnetic confinement method, the most important types of reactors are tokamaks and stellarators. Numerous fusion experiments are aiming to improve their performance, especially tokamaks, for the commercial fusion energy production plants in the future. More and more challenges have come out in physics and engineering fields, but great improvements have been achieved over the existing devices compared to other energy techniques (Figure 1.2).

1.1.2 Magnetic Confinement

Magnetic fields are ideal for confining a plasma because the separated ions and electrons of a plasma can follow magnetic field lines due to the Lorentz force(Figure 1.3):

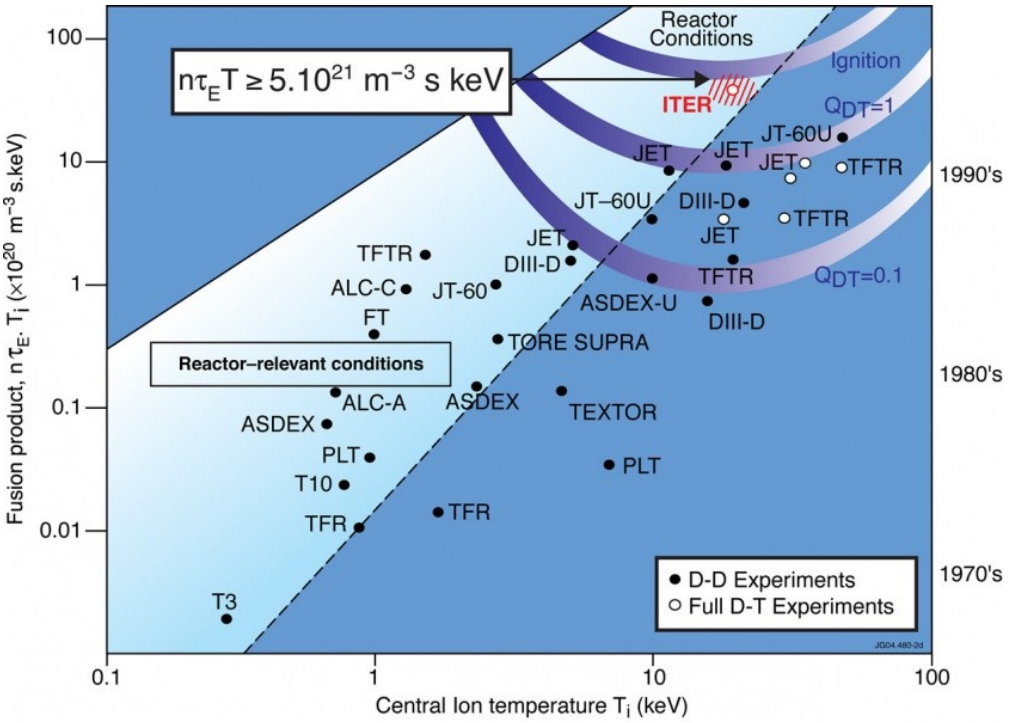

Figure 1.2: Progress of fusion research. Fusion product= Density $\times$ Energy confinement time $\times$ Temperature [11].

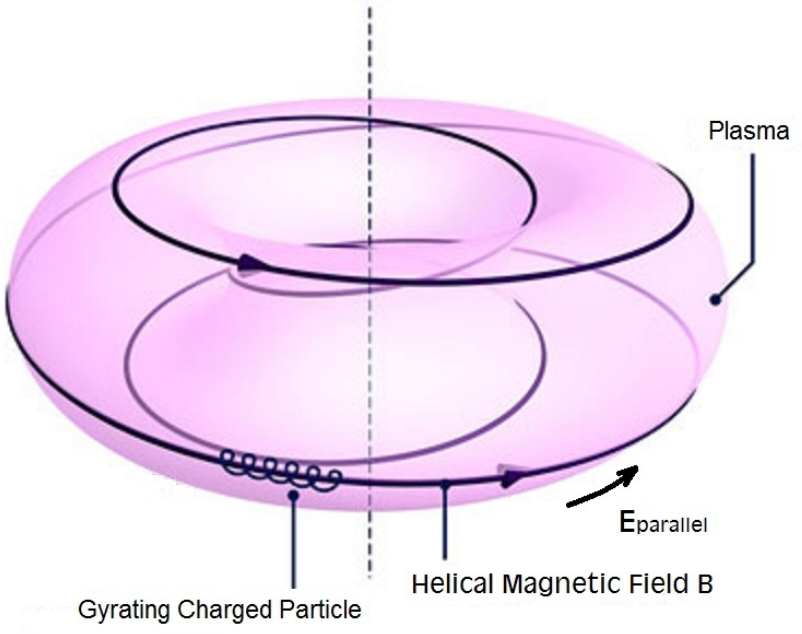

Figure 1.3: Charged particle gyrates around helical magnetic field lines with parallel electric field [12].

$$\mathbf{F} = q(\mathbf{E} + \frac{1}{c}\mathbf{v} \times \mathbf{B}), \tag{1.4}$$

where $\mathbf{E}$ is the electric field, $\mathbf{B}$ is the magnetic field, q is the particle charge, $\mathbf{v}$ is the particle's instantaneous velocity, and c is the speed of light. The magnetic force component, $q\mathbf{v} \times \mathbf{B}/c$, will always act perpendicular to the particles' movement direction. It causes the particles to gyrate around the magnetic field line, and thus the charged particles can be confined by the magnetic fields. If we connect the two ends of magnetic field line together as a ring, the charged particles in plasma will gyrate along the magnetic field lines and be restricted in toroidal space. However, particles will drift across the magnetic field slowly due to other forces generated by electric fields, the magnetic gradient ∇B, the magnetic curvature $\mathbf{R}_c \times \mathbf{B}/R_c^2 B$ and so on. So a simple toroidal magnetic field configuration is unable to confine the plasma stably.

1.2 Tokamak Concept

Tokamak is the most developed magnetic confining fusion device at present. It uses magnetic fields to confine a plasma in the shape of a torus. To achieve the plasma equilibrium, it requires a helical magnetic field moving around the torus, as shown in Figure 1.4. Such helical fields can be formed by the combination of toroidal fields (traveling around the torus in circles) and poloidal fields (traveling in circles orthogonal to the toroidal fields).

The confining magnetic fields (toroidal and poloidal fields) are generated by coils around the 'doughnut-shaped' reactor chamber and by the current flowing in the plasma itself. This current will heat the plasma (called Ohmic heating), and is normally induced by a transformer: The solenoid coils at the center of the torus is the primary winding of a transformer, and the plasma ring acts as the secondary winding [11]. The resulting helical magnetic fields keep the hot plasma away from the reactor wall.

However, the tokamak can only operate in pulsed mode because:

(1) There is a limit to the magnetic flux that can be driven through the primary coils.

(2) When the plasma temperature rises, the plasma resistance decreases and ohmic heating becomes less effective.

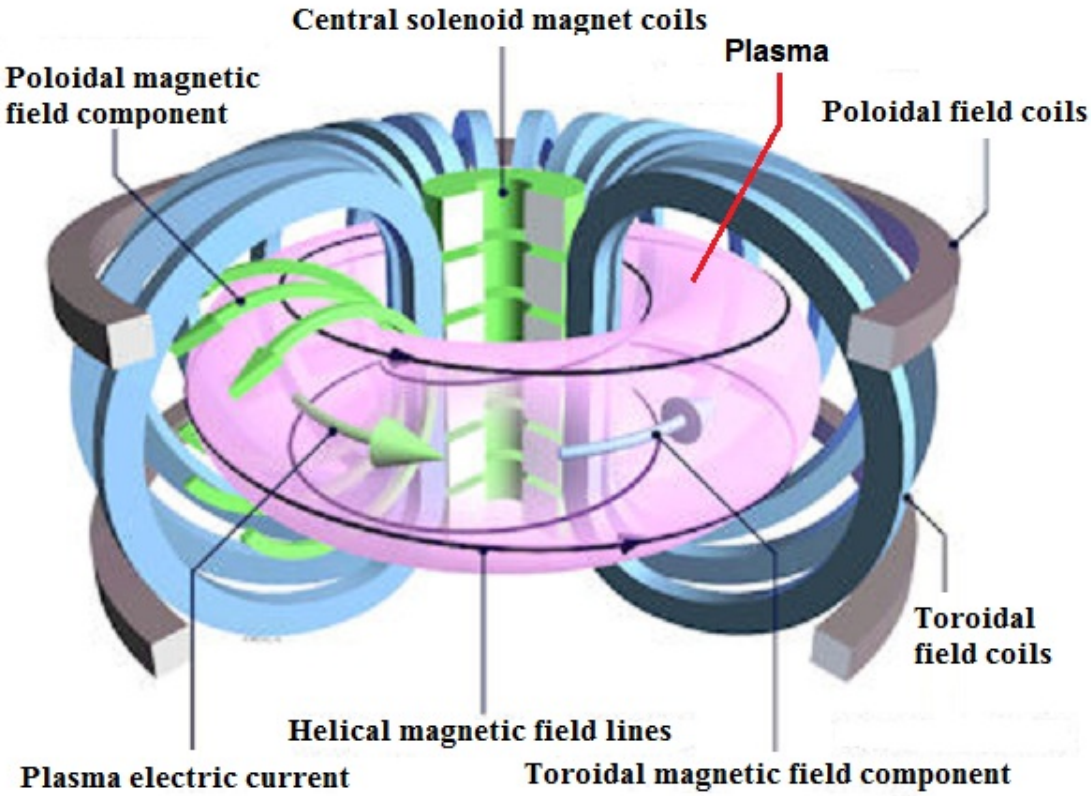

Figure 1.4: Diagram of the tokamak [13].

In order to meet the high temperature condition for fusion, additional heating is needed, such as the ion cyclotron resonance heating (ICRH), using microwaves at ion cyclotron resonant frequency for the energy absorption, and the neutral-beam injection (NBI), injecting high-energy atoms into the plasma to increase the temperature through collisions.

1.2.1 Fusion Energy Gain Factor Q

The future commercial fusion reactors need net energy outputs. To achieve efficient energy generation, it is necessary to increase the fusion energy gain factor Q to:

$$Q = \frac{P_F}{P_H} \geq 1, \tag{1.5}$$

where P_F is the produced fusion power and P_H is the external heating power ($Q = 1$ is called breakeven). The commercial reactors with ignition Q value is supposed to be $Q \to \infty$, which is a quite big challenge . The progress to approach this target is slow, yet significant. Several tokamaks have been able to approach and even pass the breakeven limit: in 1997, JET achieved Q = 0.65 with 16 MW output power [7]; in 1998, JT-60U achieved the current world record of Q = 1.25 [14]. The next generation tokamak, ITER(International Thermonuclear Experimental Reactor), is designed to achieve $Q \simeq 10$ with power production of 500 MW. ITER is the largest scientific project on Earth that involves international collaboration: China, the EU, India, Japan, Korea, Russia, and the USA. It is being built in Cadarache, France, and is expected to have a lifetime of 35 years. It will, for the first time, enable scientists to study the physics of a burning plasma from fusion reactions. ITER provides the link between scientific experimental studies on plasma physics and future commercial fusion-based power plants. Its main purpose is to demonstrate the feasibility of "tokamak" principles and to integrate the technologies essential for a future fusion reactor. Heating systems, control, diagnostics and remote maintenance systems, all important for a commercial power station, will be tested in ITER. It will also investigate systems to refuel plasma and extract impurities. The main purpose of current tokamak research around the world is to improve the design and construction of the ITER project.

1.2.2 Rotational Transform ι and Safety Factor q

Rotational transform, ι, is commonly used in stellarators and other toroidal plasma confinement systems besides the tokamak. It is the inverse of the safety factor, $q = 2\pi/\iota$. On a toroidally nested magnetic flux surfaces, the rotational transform angle can be defined as:

$$\frac{\iota}{2\pi} = \frac{R}{r}\frac{B_\theta}{B_\varphi} \tag{1.6}$$

where r is the local minor radius, and R is the local major radius (Figure 1.5). B_θ and B_φ are the poloidal and toroidal magnetic field, respectively.

The plasma safety factor, q, is another important parameter in toroidal magnetic confinement devices like the tokamak. It is defined as the mean number of poloidal transits, m, divided by the

mean number of toroidal transits, n, of the magnetic field lines on a toroidal rational flux surface:

$$q = \frac{m}{n} =< \frac{d\varphi}{d\theta} >, \tag{1.7}$$

where φ and θ are the toroidal and poloidal angles of the magnetic field lines, respectively. In fact, it denotes the number of times a magnetic field line goes around a torus "the long way" (toroidally) for each time around "the short way" (poloidally). In a circular cross-section tokamak, a magnetic field line on a flux surface approximately satisfies:

$$\frac{rd\theta}{B_\theta} = \frac{Rd\varphi}{B_\varphi}, \tag{1.8}$$

Accordingly, the safety factor q can be approximated by:

$$q \approx \frac{rB_\varphi}{RB_\theta}. \tag{1.9}$$

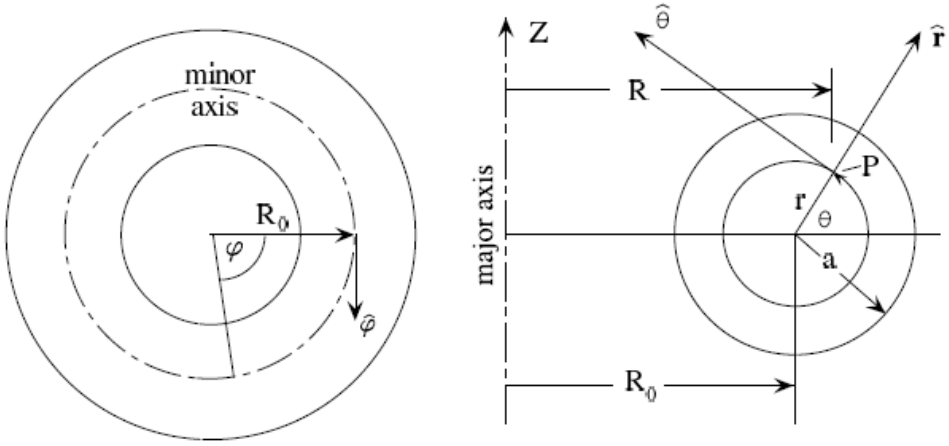

Figure 1.5: Cylindrical and local coordinates for a tokamak.

In a tokamak, for example, the safety factor q profile depends on the plasma current profile. q typically ranges from near unity in the center to 2-8 at the plasma edge of the tokamak. It is named the "Safety Factor" because larger q values are associated with higher ratios of toroidal field to poloidal field, and consequently indicating a lower risk of (current-driven) kink instabilities. The Kruskal-Shafranov limit states that if $q \leq 1$ at the last closed flux surface (the plasma edge), the plasma is magnetohydrodynamically unstable to the external kink mode [15]. Therefore, a safe

operation of a tokamak (stable plasma) requires the edge safety factor $q_{\text{edge}} > 2 \sim 3$.

1.2.3 Beta β

Confining the hot dense plasma in the tokamak consumes energy. An effective magnetic confinement fusion reactor is supposed to get more fusion energy output while requiring less energy input. The plasma density and temperature contribute to produce the plasma pressure naturally, and the input energy is mainly cost in heating the plasma and generating the confinement magnetic fields. However, if the superconducting coils are used, the electric cost in magnetic fields generation is significantly reduced. The ratio of magnetic pressure to the plasma pressure becomes a helpful index representing the effectiveness of a device. This ratio, symbolized by β, is defined by

$$\beta = \frac{p}{p_B} = \frac{nk_B(T_i + T_e)}{B^2/8\pi}, \tag{1.10}$$

where $p = nk_B(T_i + T_e)$ is the plasma pressure, $p_B = B^2/8\pi$ is the magnetic field pressure, n is plasma density, k_B is Boltzmann constant, $T_e(T_i)$ is the electron(ion) temperature, and B is the magnetic field. It turns out that the external magnets system's cost is the major cost of a tokamak reactor. An economically efficient reactor needs $\overline{\beta}$ (average β) higher than 5% [16]. Plasma instabilities, like ballooning modes, often limit the tokamak β value. With a better understanding of plasma behavior, the optimization of configuration parameters and operational process of the tokamak may improve β in the future.

1.3 Motivation and Objective

Although the tokamak configuration is promising for a fusion plant, stable confinement of a hot plasma is still an active research subject. The confinement times currently achievable in large tokamaks are much shorter than expected from the neoclassical theory [16]. Plasma turbulence is believed to be a major cause of heat loss in the tokamak. Such heat loss must be reduced sufficiently to achieve burning plasma and eventually ignition.

Turbulence phenomena are observed ubiquitously in laboratory. Numerous experimental observations and studies have demonstrated that the strong drift-wave-induced turbulence and flows

are major factors of enhancing plasma transport and limiting the quality of confinement in the tokamak. Abundant research on diverse tokamaks over the last half century have been aiming at understanding the fundamental process of those phenomena, especially the physics of mesoscale plasma sheared flows and fluctuations at the tokamak edge. The research will contribute to understanding turbulence and transport, the blanket design for the D-T reaction, the confinement improvements and other key issues for a tokamak fusion plan.

Since Winsor et al. predicted Geodesic Acoustic Mode (GAM) as an electrostatic oscillation of a toroidal plasma with rotational transform in 1968 [17], researchers have been investigating this special plasma oscillations phenomena theoretically and experimentally. Lin et al. applied three-dimensional gyrokinetic simulations to the zonal flows dynamics investigation in 1998 [18]. It turns out that the turbulence driven $\mathbf{E} \times \mathbf{B}$ zonal flows significantly reduce the turbulent transport [19]. However, the lower frequency zonal flow is expected to be more important in regulating plasma turbulence. GAM, as the high frequency oscillatory branch of zonal flows, has been observed in many tokamaks, such as T-10 [20] and ASDEX Upgrade [21]. The experimental results from different devices by various diagnostics revealed a fact that GAM can only be observed at the tokamak edge region ($\rho \approx 0.8 \sim 1$). But the theory investigation suggests the collisionless damping is exponentially small when the resonant condition is not satisfied, and the corresponding eigenmode (GAM) can be excited by a rather weak, high-frequency force [22]. Obviously, the experimental results cannot be explained well by Winsor's classical GAM theory and other relevant theory. Therefore, GAM needs to be re-examined by taking into account the distinguishing feature of the edge plasma in tokamak - collisional and resistive.

Density fluctuation feature is an important aspects of turbulence and fluctuations studies, especially for GAM. GAM has $m = 1, n = 0$ mode structure of the density fluctuations, and $m = 0, n = 0$ mode structure of the plasma potential fluctuations, where m and n are poloidal and toroidal mode numbers, respectively. This determines that the density fluctuation characteristics of GAM can provide a easier perspective to identify it and investigating the related physics. Exploring those features can help us understand the GAM phenomena and associated plasma turbulence process in the tokamak. The objective of this thesis is to investigate GAM from theoretical and experimental aspects and try to build a more plausible theory explanation for the GAM.

1.4 Outlines

Chapter one has presented a brief overview of fusion energy and its potential application, the basic tokamak configuration and concept, and a basic physics background for the work to come in this thesis.

Chapter two is dedicated to describing the fundamental classical physics theory for plasma fluctuations like GAM and MHD.

Chapter three reinvestigates the classical GAM theory with the invalid condition issue. A better explanation of the fact that GAM are only be observed at the tokamak edge is provided via a resistive GAM theory.

Chapter four introduces the structure and principle of the STOR-M tokamak with various diagnostic systems.

Chapter five gives a detailed description of the design and construction of different Langmuir probe array systems for monitoring the plasma fluctuations (i.e. density) behaviors in the STOR-M tokamak.

Chapter six presents the experimental analysis results, compared to the theoretical predicted results. Discussions on those results are addressed in details.

Chapter seven summarizes the current work results and provides suggestions for the future developments on both theory and experiments study of GAM.

CHAPTER 2

THEORY OF FLUCTUATIONS IN TOKAMAK

Investigation of the plasma fluctuations is a key subject in current fusion research, which can help us understand the plasma turbulence and transport in tokamaks. In this Chapter, the classical theory of typical plasma fluctuations like Zonal Flows and Magnetohydrodynamics(MHD) instabilities will be reviewed. Emphasis will be given to the edge fluctuations, like Geodesic Acoustic Mode(GAM) and MHD Resistive Wall Modes.

2.1 Zonal Flows and Geodesic Acoustic Mode (GAM)

Zonal flow is a toroidally symmetric electric field perturbation in a toroidal plasma. The zonal flows are ubiquitously observed in nature and in the laboratory. In magnetically confined fusion devices, the discovery of the zonal flows and the subsequent studies established the modern paradigm shift of plasma turbulence. At the end of the 20th century, researchers recognized the role of the mutual interactions between zonal flows and turbulences in the tokamak turbulence and transport study. According to the findings, those processes can determine the turbulence saturation and transport levels: First, the time-dependent sheared flow can develop from drift waves and generate the secondary instabilities; second, the formation of the sheared flow structure in the mesoscale, i.e. zonal flows, can give back-reactions on the co-existing micro-scale drift wave turbulence. Currently, it is widely accepted that zonal flows are a critical agent of self-regulation for drift wave transport and turbulence. Some works indicated that a significant portion of the available free energy is ultimately deposited in the zonal flows in the low collisionality plasmas. At the same time, zonal flows have a strong influence on the formation of transport barriers, the dynamics of barriers and transitions involving the $\mathbf{E} \times \mathbf{B}$ flows [23]. The understanding of the turbulence-zonal flows

system can advance the understanding of self-organization processes. So the study of zonal flows, including GAMs, continues to be active.

2.1.1 Zonal Flows in Tokamak

In case of tokamak plasmas, zonal flows are referred to the low frequency zonal flows and the high frequency GAMs. The low frequency zonal flow has poloidal and toroidal symmetries, with the poloidal (m) and toroidal (n) mode numbers of (m, n)=(0,0). (The mode number means the azimuthal wave number in a certain direction.) It has a finite radial wavenumber and near-zero real characteristic frequency. The associated $\mathbf{E} \times \mathbf{B}$ flow is in the poloidal direction, and its sign changes with radius in oscillatory manner(Figure 2.1).

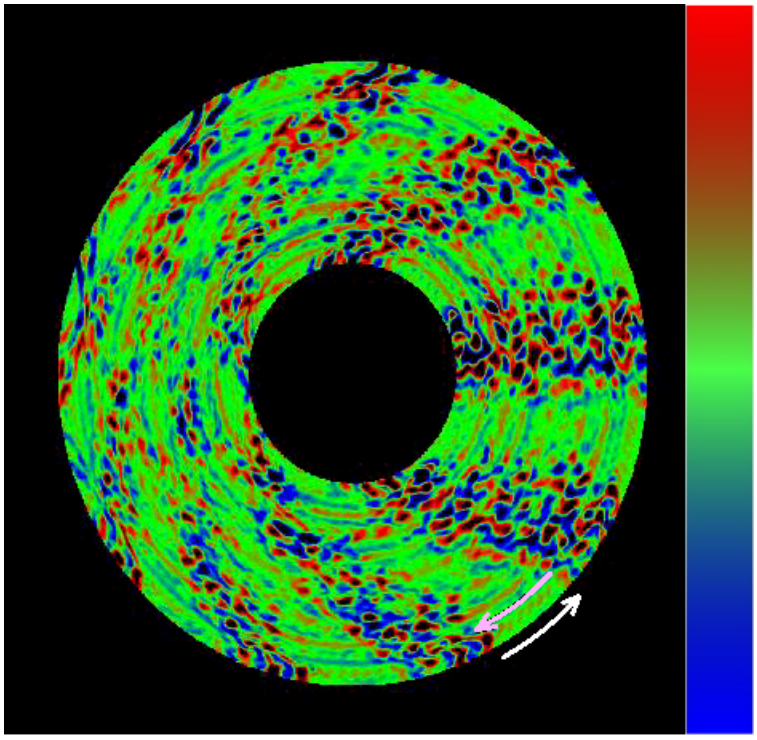

Figure 2.1: Illustration of zonal flows in poloidal cross-section of a tokamak with shearing turbulent eddies based on a computer simulation [24]. The pink and white arrows show that the directions of the poloidal flows change with radius.

The key element of the dynamic low frequency zonal flows is the shearing process of turbulent eddies caused by flows in a larger scale (Figure 2.2). In late 1990s, it was found that a turbulent plasma consists of eddies, or small vortices. Those eddies can increase the energy leaking rate. At

the same time, the experiments demonstrated that the turbulence suppression could be achieved by ramping the current peak towards the plasma edge rather than in the center [25].

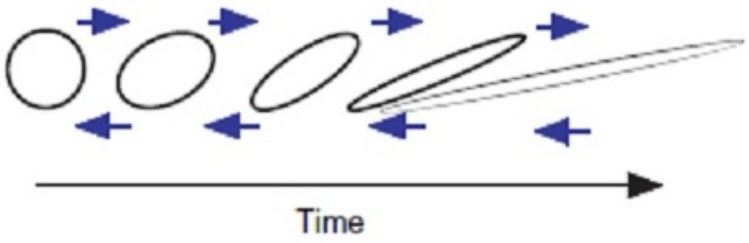

Figure 2.2: Shearing of the vortex [23].

When such current interacts with the magnetic field in a turbulent tokamak plasma, it can generate certain electric fields to drive plasma zonal flows. Consequently, the $\mathbf{E}\times\mathbf{B}$ flow is sheared. The sheared layers will strain and distort the drift waves, in which the drift wave eddies is pulled apart and break up (Figure 2.3). In this way, the shearing acts to reduce the turbulence and the transport that can drive the strong current interests in the flows. The energy loss is eliminated as a result. It was found that the low frequency zonal flows can keep irrelevant turbulent vortices for a long time and then suppress the turbulent transport effectively [26].

2.1.2 Geodesic Acoustic Mode (GAM)

The Geodesic Acoustic Mode (GAM) is a high frequency oscillatory branch of the zonal flows. In tokamaks, zonal flows may oscillate over time by coupling with poloidally asymmetric pressure perturbations, (m, n)=(1,0). The coupling is due to a geodesic curvature of magnetic field, which makes the cross-field $\mathbf{E} \times \mathbf{B}$ drifts (Figure 2.4) compressible, $\nabla \cdot \mathbf{v}_{\mathbf{E}\times\mathbf{B}} \neq 0$. GAM has the (m, n)=(0,0) electrostatic potential mode structure linearly coupling to the (m, n)=(1,0) edge density perturbation.

Winsor's Classical GAM Theory

GAM was first predicted by Winsor et al. in 1968 [17] for a toroidal plasma with rotational transform ι. It is a low frequency electrostatic cross-field plasma oscillation, which involves $m = 1$

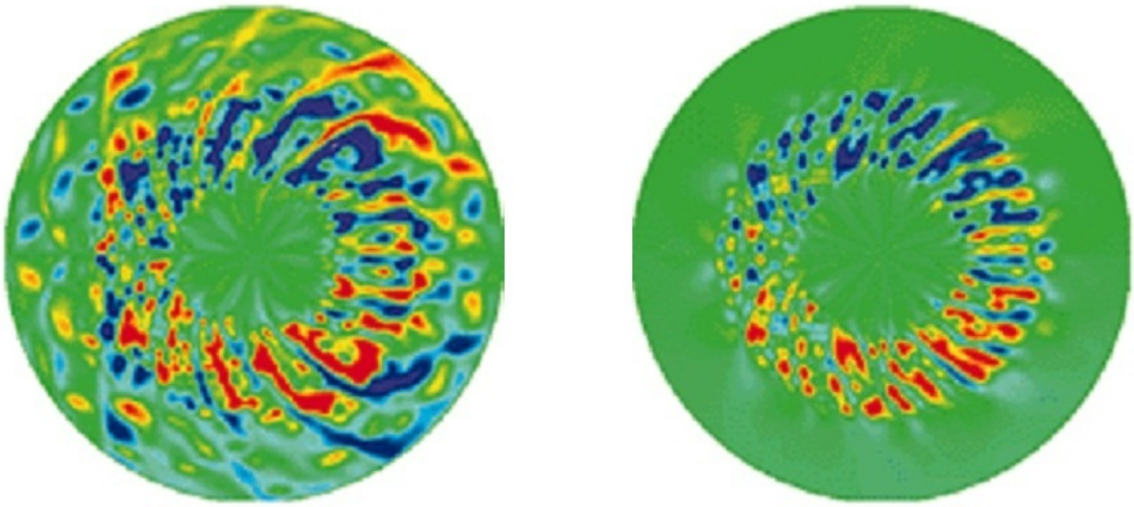

(a) Fully developed turbulence just before a transition. (b) Suppression of turbulence at the edge due to zonal flows.

Figure 2.3: Simulation illustration of the potential turbulence at the DIII-D tokamak edge. Potential turbulence at the DIII-D tokamak edge amplifies zonal flows that, in turn, suppresses turbulence at the plasma edge [25].

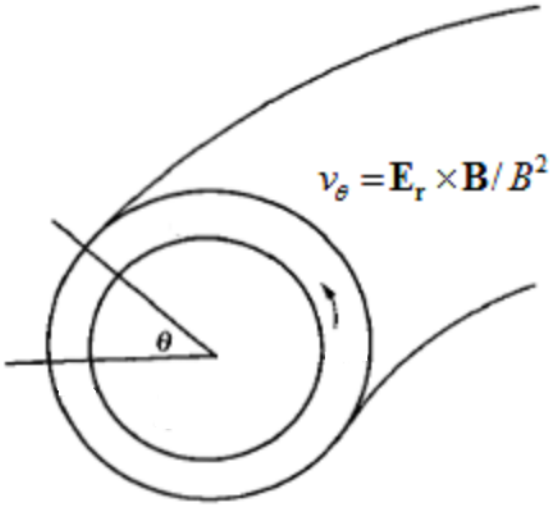

Figure 2.4: Illustration of GAM mechanism in tokamak: $\mathbf{E} \times \mathbf{B}$ drifts.

pressure disturbance and $n = 0$ potential perturbation with an azimuthal cross-field plasma flow $c\mathbf{E} \times \mathbf{B}/B^2$. In a tokamak, the typical frequency for the idea GAM is

$$\omega \approx \frac{\sqrt{2}c_s}{R_0}, \tag{2.1}$$

where $c_s = \sqrt{\frac{\gamma P}{\rho}}$ is the sound speed of plasma, and R_0 is the curvature radius of the toroidal magnetic field. Here, P is the plasma pressure and ρ is the mass density of a plasma. The classical theory of GAM is reviewed briefly below.

The plasma behaviors follow a set of key equations, namely the equation of continuity,

$$\frac{\partial n}{\partial t} + n_0 \nabla \cdot \mathbf{v} = 0, \tag{2.2}$$

and the single fluid equation of motion, given by

$$\rho_0 \frac{\partial}{\partial t}\mathbf{v} = \frac{1}{c}\mathbf{J} \times \mathbf{B} - \nabla p, \tag{2.3}$$

where n is the perturbed plasma density, n_0 is the local averaged plasma density, $\mathbf{v}$ is the plasma flow velocity, p is the the perturbed plasma pressure, $\mathbf{J}$ is the plasma current, and $\mathbf{B}$ is the local magnetic field.

In tokamak, the magnetic field is dominated by the toroidal field which is intrinsically nonuniform,

$$B = B_\phi = B_0 \left(1 + \frac{r}{R}\cos\theta\right)^{-1} \simeq B_0 \left(1 - \frac{r}{R}\cos\theta\right), \tag{2.4}$$

where B_0 is the magnetic field strength on the magnetic axis. The gradient of the toroidal magnetic field is

$$\nabla B \approx -\frac{B_0}{R}(\cos\theta \mathbf{e}_r - \sin\theta \mathbf{e}_\theta), \tag{2.5}$$

where $\mathbf{e}_r$, $\mathbf{e}_\theta$ are the radial and poloidal unit vector, respectively. The magnetic gradient makes the cross-field $\mathbf{E} \times \mathbf{B}$ drift compressible,

$$\begin{aligned} \nabla \cdot \mathbf{v}_{\mathbf{E}\times\mathbf{B}} &\approx -2c\frac{\mathbf{E} \times \mathbf{B}}{B^3} \cdot \nabla B \\ &= 2c\frac{\mathbf{E} \times \mathbf{B}}{B^2 R} \cdot (\cos\theta \mathbf{e}_r - \sin\theta \mathbf{e}_\theta). \end{aligned} \tag{2.6}$$

GAM is induced by the cross-field flow, so the single fluid equation of motion becomes

$$\rho_0 \frac{\partial \mathbf{v}_{\mathbf{E}\times\mathbf{B}}}{\partial t} = \frac{1}{c}\mathbf{J}_\perp \times \mathbf{B} - \nabla p, \tag{2.7}$$

where $\mathbf{v}_{\mathbf{E}\times\mathbf{B}}$ is the $\mathbf{E}\times\mathbf{B}$ drift velocity. $(\mathbf{B}/B^2)\times$ Eq. 2.7 yields the cross-field current

$$\mathbf{J}_\perp = \frac{c^2\rho_0}{B^2}\frac{\partial \mathbf{E}_\perp}{\partial t} + \frac{c\mathbf{B}\times\nabla p}{B^2}, \tag{2.8}$$

where $\mathbf{E}_\perp = \mathbf{E}_r = -\nabla_\perp \phi$ is the radial electric field normal to the magnetic field $\mathbf{B}$ and ϕ is the scalar potential. The first term in RHS is the ion polarization current caused by the oscillatory electric field, and the second term is called the diamagnetic current due to the plasma pressure gradient.

A physical mechanism put forward for GAM by Winsor et al. is that the charge separation caused by the ion polarization current is neutralized by the diamagnetic current (which is due to the pressure gradient in the poloidal θ direction). When $J_\parallel$ is negligible, the charge neutrality can be imposed by

$$\nabla \cdot \mathbf{J}_\perp = 0, \tag{2.9}$$

as assumed by Winsor et al.

Substituting Eq. 2.8 into Eq. 2.9, it yields

$$\frac{c^2\rho_0}{B^2}\frac{\partial}{\partial t}(-\nabla_\perp^2\phi) + c\nabla\cdot\left(\frac{\mathbf{B}\times\nabla p}{B^2}\right) = 0. \tag{2.10}$$

Because

$$\begin{aligned}
\nabla\cdot\left(\frac{\mathbf{B}\times\nabla p}{B^2}\right) &= -2\frac{\nabla B}{B^3}\cdot(\mathbf{B}\times\nabla p) \\
&= -2\frac{1}{B^2}\nabla(1-\frac{r}{R}\cos\theta)\cdot(\mathbf{B}\times\nabla p) \\
&= -2\frac{\sin\theta}{B^2 R}(\mathbf{B}\times\nabla p)_\theta + 2\frac{\cos\theta}{B^2 R}(\mathbf{B}\times\nabla p)_r.
\end{aligned} \tag{2.11}$$

Considering only radial electrical field, the time derivative of Eq. 2.10 turns into

$$\frac{c^2\rho_0}{B^2}k_r^2\frac{\partial^2\phi}{\partial t^2} = 2c\frac{\sin\theta}{B^2R}\left(\mathbf{B}\times\nabla\frac{\partial p}{\partial t}\right)_\theta. \tag{2.12}$$

Here, the geodesic curvature operator for GAM appears in the form

$$\nabla_\theta = -2\frac{\sin\theta}{R}\mathbf{e}_\theta. \tag{2.13}$$

According to Eq.2.2, the density perturbation obeys

$$\frac{\partial\rho}{\partial t} + \rho_0\nabla_\theta\cdot\mathbf{v}_{\mathbf{E}\times\mathbf{B}} = 0, \tag{2.14}$$

where $\rho_0 = Mn_0$ is the unperturbed mass density. Applying the geodesic curvature operator on it,

$$\begin{aligned}\frac{\partial\rho}{\partial t} - 2\rho_0\frac{\sin\theta}{R}\mathbf{v}_{\mathbf{E}\times\mathbf{B}}\cdot\mathbf{e}_\theta &= 0\\ \frac{\partial\rho}{\partial t} &= 2c\rho_0\frac{\sin\theta}{R}\frac{ik_r\phi}{B}.\end{aligned} \tag{2.15}$$

Therefore, in terms of the poloidal mode number, the GAM is supposed to have $m = 1$ mode structure for the plasma density perturbation ($n \propto \sin\theta$). This is because the pressure asymmetry on a flux surface are induced by the compressibility of $\mathbf{E_r}\times\mathbf{B}$ flows. The toroidal mode number of the plasma density perturbation for GAM is $n = 0$.

The ideal gas law determines

$$p = \frac{\gamma p_0}{\rho_0}\rho, \tag{2.16}$$

where γ is the adiabatic index. Substituting Eq.2.15 and Eq.2.16 into Eq.2.12, we can obtain

$$\omega^2 = 4\sin^2\theta\frac{1}{R^2}\frac{\gamma p_0}{\rho_0}. \tag{2.17}$$

Averaging it over the magnetic surface

$$\langle\ldots\rangle = \frac{1}{2\pi}\int_0^{2\pi}(\ldots)\left(1+\frac{r}{R}\cos\theta\right)d\theta,$$

and

$$\langle \sin^2 \theta \rangle = \frac{1}{2}. \tag{2.18}$$

So the dispersion relation of GAM in the Winsor's model is

$$\omega_G^2 = \frac{2\gamma P_0}{\rho_0 R^2} = \frac{2C_s^2}{R^2}, \tag{2.19}$$

where $C_s = \sqrt{\gamma P_0/\rho_0}$ is the sound speed of plasma.

Subsequent theoretical studies on GAM have revealed ion Landau damping of GAM, which is enhanced by trapped electrons [27]. It has also been shown that GAM modifies the Alfvén mode [28].

2.2 Magnetohydrodynamic (MHD) Fluctuation Modes

Magnetohydrodynamics refers to the magneto fluid dynamics or hydromagnetics. Its fundamental concept is that magnetic fields can induce currents in a moving conductive fluid. In turn, the current creates forces on the fluid and also changes the magnetic field itself. In a magnetic confined plasma, MHD fluctuation is a very common and important feature. In order to confine a plasma by a magnetic field, the stability of the equilibrium against the possible MHD instabilities must be ensured. In this section, the theory behind the MHD equilibrium and instabilities in tokamak will be introduced.

2.2.1 Ideal MHD Equilibrium

The ideal MHD is the simplest form of MHD, which assumes that the plasma is perfectly conducting with a high degree of charge neutrality without the resistivity, thermal conductivity, and viscosity. The ideal MHD assumed that the ions are relative static and only the electrons move in plasma as a single fluid. Due to the incomparable mass of electron to that of an individual ion, the contribution of the electrons to the fluid inertia is negligible for simplification. This MHD approximation is valid for the phenomena of interest among certain range: the spatial scale lengths is sufficiently large that $k_\perp r_{ci} < 1$ ($k_\perp$ is the cross-field wavelength and r_{ci} is the ion Larmor radius),

and the characteristic frequency or growth rate is sufficiently slow that $|\partial/\partial t \ll \Omega_i|$, where Ω_i is the ion cyclotron frequency.

In single-fluid MHD model for a fully ionized hydrogen plasma,$n_{i0} = n_{e0} = n_0$,(0 stands for unperturbed case). The basic equations for ideal MHD model are:

$$\frac{\partial \rho}{\partial t} + \nabla \cdot (\rho \mathbf{v}) = 0, \text{ continuity equation} \tag{2.20}$$

$$\rho_0 \left(\frac{\partial \mathbf{v}}{\partial t} + \mathbf{v} \cdot \nabla \right) \mathbf{v} = \frac{1}{c} \mathbf{J} \times \mathbf{B} - \nabla p, \text{ equation of motion} \tag{2.21}$$

$$\nabla \cdot \mathbf{J} = \nabla \cdot \mathbf{J}_\perp + \nabla \cdot \mathbf{J}_\parallel = 0, \text{charge neutrality} \tag{2.22}$$

$$\mathbf{E} + \frac{1}{c} \mathbf{v} \times \mathbf{B} = \eta \mathbf{J} \simeq 0, \text{Ohm's law} \tag{2.23}$$

$$\nabla \times \mathbf{E} = -\frac{1}{c} \frac{\partial \mathbf{B}}{\partial t}, \text{Faraday's law} \tag{2.24}$$

$$\nabla \times \mathbf{B} \simeq \frac{4\pi}{c} \mathbf{J}, \text{Ampere's law} \tag{2.25}$$

$$\nabla \cdot \mathbf{B} = 0, \text{Absence of magnetic monopoles} \tag{2.26}$$

$$p \rho^{-\gamma} = const., \text{equation of state} \tag{2.27}$$

where the resistivity $\eta \simeq 0$ for the ideal MHD, and γ is the adiabatic index. $\perp$ ($\parallel$) stand for the vector component perpendicular(parallel) to the magnetic field. In Eq.2.25, the displacement current is ignored. The average plasma flow velocity $\mathbf{v}$ can be approximated by the ion velocity $\mathbf{v} = (M\mathbf{v}_i + m\mathbf{v}_e)/(M+m) \simeq \mathbf{v}_i$, and the plasma mass density can be estimated by $\rho = (M + m)n_0 \simeq M n_0$.

In MHD equilibrium, there is no time variation item ($\partial/\partial t = 0$), and the plasma flow term

$\rho\mathbf{v}\cdot\nabla\mathbf{v}$ is ignorable. Therefore, Eq.2.21 becomes a force balance equation between magnetic and pressure forces with an isotropic plasma pressure:

$$\nabla p = \frac{1}{c}\mathbf{J}\times\mathbf{B}. \tag{2.28}$$

Together with Eq.2.25 and Eq.2.26, the force balance equation Eq.2.28 can be expressed as:

$$\nabla\left(p+\frac{B^2}{8\pi}\right) = \frac{1}{4\pi}\mathbf{B}\cdot\nabla\mathbf{B}. \tag{2.29}$$

This is a nonlinear differential equation of **B** for the MHD equilibrium and the solutions may not be unique.

For axially symmetric toroidal equilibrium plasma like tokamak, Grad [29] and Shafranov [30] derived the following equation, known as the Grad-Shafranov equation,

$$\left(\frac{\partial^2}{\partial r^2}-\frac{1}{r}\frac{\partial}{\partial r}+\frac{\partial^2}{\partial z^2}\right)\psi = -\frac{8\pi^2}{c}\left(2\pi c r^2\frac{dp}{d\psi}+\frac{1}{c}\frac{dI^2}{d\psi}\right), \tag{2.30}$$

where the cylindrical coordinates (r,ϕ,z) is used, $\psi = 2\pi r A\phi$ is the magnetic flux, $I = I(\psi)$ is the equi-poloidal current surface, and $p = p(\psi)$. The axisymmetric nature of tokamak determines that

$$\psi = \oint \mathbf{A}\cdot d\mathbf{l} = 2\pi r A_\phi, \tag{2.31}$$

where **A** is the vector potential of the magnetic field. A surface where $\psi =$ constant is called a magnetic surface. On such a surface, p and I satisfy

$$\frac{\partial p}{\partial r} = \frac{\partial\psi}{\partial r}\frac{dp(\psi)}{d\psi}, \tag{2.32}$$

and

$$\frac{\partial I}{\partial r} = \frac{\partial\psi}{\partial r}\frac{dI(\psi)}{d\psi}. \tag{2.33}$$

Generally, Eq.2.30 is nonlinear. Solving this equation requires computationally expensive numerical analysis. However, if the toroidal current

$$J_\phi = 2\pi cr\left(\frac{dp}{d\psi} + \frac{1}{2\pi c^2 r^2}\frac{dI^2}{d\psi}\right) \tag{2.34}$$

is a linear function of ψ, approximate analytic solutions may be found. Based on the ideal MHD equilibrium model, certain operation limits can be derived. One example is the ideal MHD beta limit [31], which is

$$\beta_{max} \simeq 2.2\frac{I\,[\mathtt{MA}]\,R\,[\mathtt{m}]}{a\,[\mathtt{m}]}.$$

2.2.2 MHD Instabilities

MHD instabilities are dangerous phenomena for the tokamak operation that can drive the destruction of magnetic surfaces, severely degrade energy confinement and even terminate plasma discharge. MHD instabilities are globe modes, which can be characterized by large spatial scales and short time scales. Investigating the physics nature of MHD instabilities will benefit finding approaches to actively control and prevent the MHD instabilities, and thereby enhance the performance at high beta and mitigate the violation consequences.

MHD instabilities can be classified into two categories according to their driving source: One is the current-driven instabilities triggered by the nonuniformity in the plasma current; the other one is the pressure-driven instabilities which are proportional to the pressure gradient ∇p_0. [32]

In tokamak, the plasma is vulnerable to the pressure-driven instabilities, such as the ballooning modes. As a result of balancing magnetic pressure and plasma pressure, the toroidal geometry of magnetic field lines drives the plasma to expand outwards. If the plasma pressure gradient exceeds a certain limit, or the unfavorable curvature effect is appreciable, the most dangerous MHD instabilities occur. The lowest order dispersion relation of the ballooning mode is given by [33]

$$\omega^2 \simeq k_\parallel^2 V_A^2 - \frac{2k_B[T_e(1+\eta_e) + T_i(1+\eta_i)]}{L_n RM}, \tag{2.35}$$

where $k_\parallel \simeq 1/qR$ is the wavenumber along the magnetic field, $V_A = \sqrt{B^2/4\pi n_0 M}$ is the Alfvén velocity, L_n is the density gradient scale length, and $\eta_e(\eta_i)$ is the electron(ion) temperature gradi-

ent.

For current-driven MHD instabilities, the most dangerous one is the kink mode. The kink mode is caused by the radial gradient of the plasma current. The kink instabilities occur in plasma when the plasma current exceeds a critical value (threshold). The twisting of poloidal magnetic field produced by the excessive current causes the helical deformation to trigger the kink modes. In the lower order, the kink mode dispersion relation is determined by [32]

$$\omega^2 \simeq \frac{2V_A^2}{(qR)^2}(m - nq)(m - nq - 1), \tag{2.36}$$

where q is the safety factor, and the most dangerous instabilities occur when the mode numbers are as low as $m = n = 1$. The stability condition for this mode is $q(a) > 1$, which imposes a limit to the plasma total current:

$$I_0 < \frac{c}{2}\frac{a^2}{R_0}B_0, \tag{2.37}$$

where a and R_0 is the minor radius and major radius of a tokamak separately. This threshold current was derived by Kruskal and Shafranov first, and thus called the Kruskal-Shafranov current.

The high order of the ballooning modes will dominate the edge MHD fluctuation activities. They relate to the edge localized modes (ELMs) in H-mode condition as well.

2.2.3 MHD Resistive Wall Modes

An important instability that limits plasma performance in tokamaks is the resistive wall modes (RWM). RWM is a special form of the ideal external kink mode with the growth rate slowing down to τ_W^{-1}, the rate of flux diffusion through a nearby resistive wall. Theoretically, the presence of a perfectly conducting wall can significantly improve the ideal kink mode stability in tokamak. However, since real walls have finite conductivity, the kink mode is instead converted to a slowly growing RWM, which is unstable [34]. The resistive wall mode has been observed in tokamak experiments recently. It was found that the pressure and current gradients at the plasma edge can drive the RWM. RWM stability already becomes a key issue for many magnetic confinement devices, including the tokamak. It has now been demonstrated that both rotation and magnetic feedback can stabilize the RWM [35, 36]. In order to understand the physics of the RWM and developing

better means to stabilize it. A closely related issue is to understand plasma rotation, its sources and sinks, and its role in stabilizing the RWM.

There are other types of MHD modes in tokamak, such as neoclassical tearing modes. However, We are not going to introduce them here.

CHAPTER 3

COUPLING OF GAM WITH ALFVÉN MODE AND RESISTIVE GAM

In the last chapter, the classical GAM theory was simply described based on Winsor's analysis 50 years ago. However, several limitations of this classical theory have emerged recently. First, the analysis based on the neoclassical theory found the GAM is coupled with the Alfvén mode [28], which is unpredictable with Winsor's model; Second, The recent experiments reports in T-10 [20] and ASDEX Upgrade [21] showed that the GAMs can only be observed in the edge of tokamak. Those limitations make the validity of the classical theory doubtable. Alternative theories of GAM are given in this chapter [37], and a resistive GAM theory is put forward as a better explanation to the experimental observations.

3.1 Electromagnetic Two-fluid Analysis for GAM

As pointed out before, GAMs are low frequency acoustic type mesoscale modes at the edge area of tokamaks. This indicates the finite parallel wavenumber $k_{\|}$ and low temperature background. Accordingly, the electron adiabatic assumption $\omega \ll k_{\|} v_{Te}$ should be satisfied in a common sense, where v_{Te} is the electron thermal velocity. However, at the tokamak edge, ion contribution to the parallel current $J_{\|}$ is not negligible anymore, so the single fluid analysis is not accurate enough for the GAM study. Instead, the two-fluid approach and the gyro-kinetic formulation [37–39] are required to reinvestigate GAM. (In the following two sections analyses, $k_B T$ is simplified to T.)

Following the procedure developed in Ref. [37], the gyro-kinetic formulation is used for solving

Vlasov equation,

$$\frac{\partial f}{\partial t} + \mathbf{v} \cdot \nabla f + \frac{e}{m}\left(\mathbf{E} + \frac{1}{c}\mathbf{v} \times \mathbf{B}\right) \cdot \frac{\partial f}{\partial \mathbf{v}} = 0, \tag{3.1}$$

where f is the velocity distribution function. The density perturbation can be evaluated from the distribution function by

$$n = \int f d^3 v. \tag{3.2}$$

Assuming $f = f_0 + f_1$, in which the unperturbed distribution $f_0(\mathbf{v})$ obeys Maxwellian distribution $f_M(v^2)$. This is a reasonable assumption when the confinement time far exceeds the collision time. For low-frequency modes of interest, $\omega \ll \Omega_i (\ll \Omega_e)$. Considering the zeroth order harmonic only, the desired perturbed distribution function can be approximated by

$$f = -\frac{e\phi}{T} f_M + \frac{\omega - \hat{\omega}_*}{\omega - \hat{\omega}_D - k_\parallel v_\parallel}\left(\phi - \frac{v_\parallel}{c} A_\parallel\right) J_0^2(\Lambda) \frac{e}{T} f_M, \tag{3.3}$$

with

$$\Lambda = k_\perp v_\perp / \Omega$$

and J_0 is the zeroth order Bessel function, where Ω is the charged particle's gyrofrequency. The energy dependent diamagnetic drift frequency operator and the nonuniformity induced magnetic drift frequency operator can be written as

$$\begin{aligned} \hat{\omega}_*(v^2) &= \frac{cT}{eB^2}(\mathbf{B} \times \nabla \ln f_M) \cdot \mathbf{k} \\ &= \frac{cT}{eB^2}(\mathbf{B} \times \nabla \ln n_0) \cdot \mathbf{k} \left[1 + \eta(\frac{mv^2}{2T} - \frac{3}{2})\right], \end{aligned} \tag{3.4}$$

and

$$\hat{\omega}_D(\mathbf{v}) = \frac{cm}{eB^3}(\frac{1}{2}v_\perp^2 + v_\parallel^2)(\nabla B \times \mathbf{B}_0) \cdot \mathbf{k}_\perp, \tag{3.5}$$

where

$$\eta = \frac{d \ln T}{d \ln n_0}$$

is the temperature gradient relative to the density gradient.

For adiabatic electrons, the finite Larmor radius effect can be ignored, because

$$J_0(\Lambda_e) = J_0\left(\frac{k_\perp v_\perp}{\Omega_e}\right) = 1.$$

Then from Eq. 3.3, the perturbed electron distribution function becomes

$$f_e = \frac{e\phi}{T_e} f_{Me} - \frac{\omega - \hat{\omega}_{*e}}{\omega - \hat{\omega}_{De} - k_\parallel v_\parallel}\left(\phi - \frac{v_\parallel}{c}A_\parallel\right)\frac{e}{T_e} f_{Me}. \tag{3.6}$$

In the low frequency limit, $|\omega| \ll k_\parallel v_{Te}$, the parallel current is largely carried by the electrons. Taking the 1st order moment integration of the perturbed electron velocity distribution function, the electron parallel current can be evaluated by

$$\begin{aligned} J_{\parallel e} &= -e\int v_\parallel f_e d^3v \\ &= \frac{n_0 e^2}{k_\parallel T_e}\left[(\omega_{*e} - \omega)\phi + \frac{(\omega - \omega_{*e})(\omega - \omega_{De}) + \eta_e \omega_{*e}\omega_{De}}{ck_\parallel}A_\parallel\right], \end{aligned} \tag{3.7}$$

where ω_{*e} is the electron diamagnetic drift frequency as defined by

$$\omega_{*e} = \frac{cT_e}{eB^2}(\nabla \ln n \times \mathbf{B})\cdot\mathbf{k}_\perp, \tag{3.8}$$

and ω_{De} is the electron magnetic drift frequency with thermal approximation,

$$\begin{aligned} \omega_{De} &= \frac{mc}{eB^3}\langle\frac{1}{2}v_\perp^2 + v_\parallel^2\rangle(\nabla B \times \mathbf{B})\cdot\mathbf{k}_\perp \\ &\simeq \frac{2cT_e}{eB^3}(\nabla B \times \mathbf{B})\cdot\mathbf{k}_\perp, \end{aligned} \tag{3.9}$$

where $\langle\ldots\rangle = \int \ldots f_e d^3v$ represent Maxwellian average. If GAM is an electromagnetic mode, in the low frequency limit ($\omega \ll k_\parallel v_{Te}$), the electron density perturbation can be assessed by

$$\begin{aligned} n_e = \int f_e d^3v &= \frac{e\phi}{T_e}n_0 - \left\langle\frac{\omega - \hat{\omega}_{*e}(v^2)}{\omega + \hat{\omega}_{De}(\mathbf{v}) - k_\parallel v_\parallel}\left(\phi - \frac{v_\parallel}{c}A_\parallel\right)\right\rangle_{\mathbf{v}}\frac{e}{T_e}n_0 \\ &\simeq \left(\phi - \frac{\omega - \omega_{*e}}{ck_\parallel}A_\parallel\right)\frac{e}{T_e}n_0. \end{aligned} \tag{3.10}$$

Meanwhile, the ion transit effect is negligibly small when $\omega \gg k_\parallel v_{Ti}$. This assumption ensures that the ion density perturbation is electrostatic and the parallel ion current $J_{\parallel i}$ can be ignored. In the case of tokamak, $k_\parallel v_{Ti}/\omega$ is of $\sqrt{\beta}$ order, which is indeed small (β is a few percent normally). Therefore, the ion density perturbation may be qualitatively approximated by [38]

$$n_i = \frac{(\omega + \frac{5}{3}\omega_{Di})[\omega_{*e} - \omega_{De} - (k_\perp \rho_s)^2(\omega + \omega_{*i} + \eta_i \omega_{*i})] + (\frac{2}{3} - \eta_i)\omega_{*e}\omega_{Di}}{\omega^2 + \frac{10}{3}\omega\omega_{Di} + \frac{5}{3}\omega_{Di}^2} \frac{e\phi}{T_e} n_0, \tag{3.11}$$

where

$$\eta_i = \frac{d \ln T_i}{d \ln n_0}$$

is the ion temperature gradient. The ion diamagnetic drift frequency ω_{*i} and the ion magnetic drift frequency ω_{Di} can be expressed as

$$\omega_{*i} = \frac{cT_i}{eB^2}(\nabla \ln n \times \mathbf{B}) \cdot \mathbf{k}_\perp \tag{3.12}$$

and

$$\omega_{Di} \simeq \frac{2cT_i}{eB^3}(\nabla B \times \mathbf{B}) \cdot \mathbf{k}_\perp \tag{3.13}$$

Substituting the parallel electron current as Eq. 3.7 into Ampere's law,

$$\nabla_\perp^2 A_\parallel = -\frac{4\pi}{c} J_{\parallel e}, \tag{3.14}$$

along with the charge neutrality condition,

$$n_e = n_i, \tag{3.15}$$

the mode equation can be obtained as follows,

$$k_\parallel k_\perp^2 k_\parallel \frac{A_\parallel}{k_\parallel} = \frac{k_{De}^2}{c^2}\left[-\frac{(\omega - \omega_{*e})^2}{G} + (\omega - \omega_{*e})(\omega - \omega_{De}) + \eta_e \omega_{*e}\omega_{De}\right]\frac{A_\parallel}{k_\parallel}, \tag{3.16}$$

where

$$k_{De}^2 = \frac{4\pi n_0 e^2}{T_e} \tag{3.17}$$

and

$$G = 1 - \frac{(\omega + \frac{5}{3}\omega_{Di})[\omega_{*e} - \omega_{De} - (k_\perp \rho_s)^2(\omega + \omega_{*i} + \eta_i \omega_{*i})] + (\frac{2}{3} - \eta_i)\omega_{*e}\omega_{Di}}{\omega^2 + \frac{10}{3}\omega\omega_{Di} + \frac{5}{3}\omega_{Di}^2}. \tag{3.18}$$

Assuming that $T_i = T_e$ and ignoring the density and temperature gradients ($\omega_* = 0$). Since $(k_\perp \rho_s)^2 \ll 1$, Eq. 3.16 can be reduced to

$$\begin{aligned} k_\parallel k_\perp^2 k_\parallel &= \frac{k_{De}^2}{c^2}\left[\frac{\omega^4 (k_\perp \rho_s)^2 - \frac{8}{3}\omega^2\omega_D^2 - \frac{10}{3}\omega\omega_D^3}{\omega^2}\right] \\ &\simeq \frac{k_{De}^2}{c^2}\left[\omega^2 (k_\perp \rho_s)^2 - \frac{8}{3}\omega_D^2\right], \end{aligned} \tag{3.19}$$

when $|\omega| \gg \omega_D$.

According to Eq. 3.9, ω_D is subject to $\sin\theta/R$ due to the geodesic curvature of tokamak. With the finite $k_\parallel$ in GAM as

$$k_\parallel = -i\frac{1}{qR}\frac{d}{d\theta} \tag{3.20}$$

Eq. 3.19 can be rewritten as below,

$$\begin{aligned} -k_\perp^2 \frac{d^2}{d\theta^2} &= (qR)^2\left[\frac{k_{De}^2 (k_\perp \rho_s)^2}{c^2}\omega^2 - \frac{8}{3}\frac{k_{De}^2\omega_D^2}{c^2}\right] \\ &= (qR)^2\left[\frac{k_\perp^2}{v_A^2}\omega^2 - \frac{8}{3}\frac{2c_s^2}{R^2}(1 - \cos 2\theta)\frac{k_\perp^2}{v_A^2}\right] \\ &= \frac{k_\perp^2}{\omega_A^2}\left(\omega^2 - \frac{8}{3}\frac{2c_s^2}{R^2} + \frac{8}{3}\frac{2c_s^2}{R^2}\cos 2\theta\right), \end{aligned} \tag{3.21}$$

where

$$v_A = \frac{B}{\sqrt{4\pi n_0 m_i}}$$

is Alfvén velocity, and $\omega_A = \frac{v_A}{qR}$ is the Alfvén frequency. The mode equation Eq. 3.21 is a standard Mathieu equation,

$$\left(\frac{d^2}{d\theta^2} + a + b\cos 2\theta\right) f(\theta) = 0, \tag{3.22}$$

in which

$$a = \frac{1}{\omega_A^2}\left(\omega^2 - \frac{8}{3}\frac{2c_s^2}{R^2}\right) \tag{3.23}$$

and

$$b = \frac{8}{3}\frac{2c_s^2}{\omega_A^2 R^2}. \tag{3.24}$$

The calculation results of eigenvalues a and b in the Mathieu equation Eq. 3.22 for quasi-sine solution $f(\theta) \propto \sin\theta$ and quasi-cosine solution $f(\theta) \propto \cos\theta$ are shown in Figure 3.1.

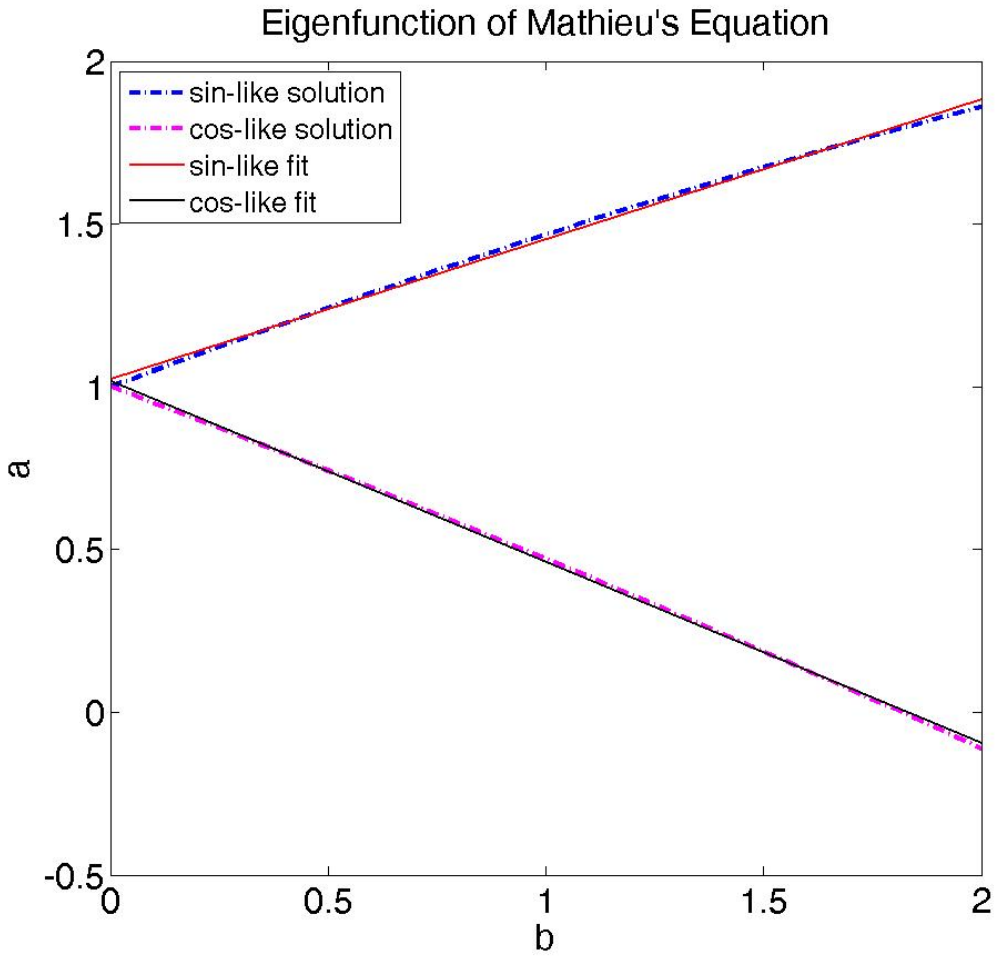

Figure 3.1: Eigenvalues of mathieu equation. Dashed line: calculation results. Solid line: linear fitting of the calculation results.

Clearly, a has a quasi-linear relationship with b when $f(\theta)$ is proportional to $\sin\theta$ or $\cos\theta$. In GAM, density has (m, n)=(1,0) mode structure, which means $f(\theta) \propto \sin\theta$. After linear fitting of the eigenvalues a and b as in Fig. 3.1, the obtained a and b for quasi-sine solution approximately satisfy

$$a = 0.430293b + 1.02344 \simeq 1 + \frac{b}{2}. \tag{3.25}$$

Substituting Eq. 3.23 and Eq. 3.24 into Eq. 3.25, then we can get the dispersion relation for the electromagnetic GAM as

$$\omega^2 = \omega_A^2 + 4\frac{2c_s^2}{R^2}. \tag{3.26}$$

It shows that the electromagnetic GAM only modifies the Alfvén frequency. If in the ballooning mode, we consider such GAM effects, then the lowest order dispersion relation of the ballooning mode can be modified as

$$\omega^2 \simeq k_\parallel^2 V_A^2 - \frac{2c_s^2}{L_p R} + 4\omega_G^2, \tag{3.27}$$

where $\omega_G^2 = 2c_s^2/R^2$ is the classical GAM frequency, and the second term in RHS is the growth rate of the interchange mode. It is evident that GAM has a stabilizing effect on the ballooning mode.

3.2 Resistive GAM

Due to the experimental facts that GAMs were only be observed at the tokamaks' edge, the resistivity could be crucial to the GAM theory. In this section, the method for the resistive ballooning mode analysis [38, 39] is applied for developing the resistive GAM theory in the tokamak geometry. The numerical calculation for resistive GAM characteristic frequency provides a reliable explanation for the edge GAM phenomena.

In tokamak collisional edge region, the electron-ion collision frequency usually satisfies

$$\nu_e \gg \omega, \omega_{*e}, \omega_{De},$$

and nonadiabatic electron condition

$$\nu_e \gg k_\parallel v_{Te}.$$

Considering the collision term in the kinetic equation, there is

$$\frac{\partial f_e}{\partial t} + (\mathbf{v}_{De} + \mathbf{v}_\parallel)\cdot\nabla f_e + \nabla\cdot(\mathbf{v}_e f_m) + \frac{e}{T_e}E_\parallel v_\parallel f_M = -\nu_e f_e + \frac{n_e}{n_0}f_M, \tag{3.28}$$

where

$$\mathbf{v}_{De} = \frac{mc}{eB^3}\left(\frac{v_\perp^2}{2} + v_\parallel^2\right)\nabla B \times \mathbf{B}$$

is the electron magnetic-drift velocity. As a result, the electron density perturbation can be approximated by

$$\begin{aligned} n_e &= \int f_e d^3v \\ &= \frac{1 + \frac{\omega + i\nu_e - \omega_{*e}}{\omega_{Te}} Z(\zeta_e)}{1 + \frac{i\nu_e}{\omega_{Te}} Z(\zeta_e)} \frac{e\phi}{T_e} n_0 \\ &\simeq \frac{(\omega_{*e} - \omega_{De})(\omega + i\nu_e - \omega_{De})^2 - i\nu_e v_{Te}^2 k_\parallel^2}{(\omega - \omega_{De})(\omega + i\nu_e - \omega_{De})^2 - i\nu_e v_{Te}^2 k_\parallel^2} \frac{e\phi}{T_e} n_0 \\ &\approx \frac{\omega_{*e} - \omega_{De} + i\omega_\chi}{\omega - \omega_{De} + i\omega_\chi} \frac{e\phi}{T_e} n_0, \end{aligned} \tag{3.29}$$

where

$$\omega_{Te} = |k_\parallel| v_{Te} \tag{3.30}$$

is the electron transit frequency. $Z(\zeta_e)$ is the plasma dispersion function with the argument $\zeta_e = (\omega + i\nu_e - \omega_{De})/\omega_{Te}$. When the collision frequency ν_e is large enough, $|\zeta_e| \gg 1$ for resistive modes. ω_χ is the electron thermal-diffusion rate along the magnetic field, which follows

$$\omega_\chi = \frac{k_\parallel^2 T_e}{m_e \nu_e} = \frac{\omega_{Te}^2}{\nu_e} \tag{3.31}$$

For the ion density, the perturbed ion distribution function f_i can be found from Eq. 3.3, then

$$f_i = -\frac{e\phi}{T_i} f_{Mi} + \frac{\omega - \hat{\omega}_{*i}}{\omega - \hat{\omega}_{Di} - k_\parallel v_\parallel} \left(\phi - \frac{v_\parallel}{c} A_\parallel\right) J_0^2 \left(\frac{k_\perp v_\perp}{\Omega_i}\right) \frac{e}{T_i} f_{Mi}. \tag{3.32}$$

For resistive GAM, we may assume that the mode frequency is much larger than the ion transit frequency $\omega \gg k_\parallel v_{Ti}$. In addition, GAM is independent to the nonuniformity of plasma density.

Integrating Eq. 3.32 over the velocity, then the ion density perturbation becomes

$$\begin{aligned} n_i &= \int f_i d^3v \\ &\simeq \frac{e\phi}{T_i} n_0 \left[-1 + \int \frac{\omega + \hat{\omega}_{*i}}{\omega + \hat{\omega}_{Di}} J_0^2 \left(\frac{k_\perp v_\perp}{\Omega_i} \right) f_{Mi} d\mathbf{v} \right] \\ &\simeq \left[-1 + \frac{\omega}{\omega + \omega_{Di}} \exp^{-b_i} I_0(b_i) \right] \frac{e\phi}{T_i} n_0, \end{aligned} \tag{3.33}$$

where I_0 is the modified Bessel function, and $b_i = (k_\perp \rho_i)^2 = k_\perp^2 T_i / M\Omega_i^2$ is the finite ion Larmor radius parameter.

Substituting Eq. 3.29 and Eq. 3.33 into the charge neutrality condition

$$n_i = n_e,$$

it yields the resistive Geodesic Acoustic Mode equation

$$\omega^2 + \left[i\omega_\chi \left(1 + \frac{\iota_T}{D} \right) - \omega_{De} \right] \omega + \frac{\iota_T}{D}(1 + \iota_T)(i\omega_\chi \omega_{De} - \omega_{De}^2) = 0, \tag{3.34}$$

where $D = 1 - \exp^{-b_i} I_0(b_i)$ and $\iota_T = \frac{T_i}{T_e}$ is the ion-electron temperature ratio. Eq. 3.34 is a quadratic euqation, and its positive real solution part will be the resistive GAM frequency ω_{GR}.

For the case that $b_i \ll 1$ (long cross-field wavelengths), ion viscosity can be neglect, and ions can be treated as collisionless. The Eq. 3.34 can be simplified into

$$\omega^2 + \left[i\omega_\chi \left(1 + \frac{1}{b_s} \right) - \omega_{De} \right] \omega + \frac{1}{b_s}(1 + \tau)(i\omega_\chi \omega_{De} - \omega_{De}^2) = 0. \tag{3.35}$$

In addition, if $b_s \ll 1$, $\iota_T = 1$, and $\omega \gg \omega_{De}$ for acoustic type modes, the Eq. 3.35 can be further reduced to

$$\omega^2 + i\frac{\omega_\chi}{b_s}\omega - 2\frac{\omega_D^2}{b_s} = 0, \tag{3.36}$$

which predicts a damped GAM oscillation characteristic. However, when collision is strong (high collision frequency ν_e), ω_χ is small. Consequently, the solution of Eq. 3.36 is approximately

$$\omega = \sqrt{2}\frac{\omega_D}{\sqrt{b_s}} = \omega_{Ge}. \tag{3.37}$$

This is exactly the lowest order GAM frequency we got from the Winsor's (classical) model. Therefore, the electrostatic GAM can exist in tokamak collisional edge region. In this case, the resistivity (strong collision) suppresses the parallel current $J_{\|e}$.

The collision also induces damping as a consequence based on the descriptions above. Some further investigations of the damping and the resistive GAM mode frequency were conducted by the computation with the resistive GAM theory. In tokamaks, b_s values are usually in the range of $0.01 \sim 1$, while ω_χ/ω_{De} ratios are in the range of $0.01 \sim 1$. Based on the numerical calculation results of Eq. 3.34, Figure 3.2 shows the relative resistive GAM frequency ω_{GR}/ω_{Ge} in terms of b_s, ω_χ/ω_{De} and ι_T. b_s and ω_χ/ω_{De} have the values in the supposed ranges that mentioned above, and ratio $\frac{T_i}{Te}$ is assumed to be 1, 1.5 or 2.

In the figure, it is clear that if the collision is very intense, ω_χ goes close to 0, and ω_{GR} approaches ω_{Ge} with minimal damping. So the GAM can exist at the high collision region. But when the collision becomes weaker (collisionless), with small b_s value ($k_\perp$ or $T_e(T_i)$ is small), ω_χ/ω_{De} approaches to 1, and the real part of the solution $Re(\omega_{GR})$ decline sharply. At the same time, the imaginary part of the solution $Im(\omega_{GR})$ indicates severe damping of resistive GAM. Under the weak collision condition, if the b_s becomes larger (longer cross-field wavenumber $k_\perp$ or higher plasma temperature $T_e(T_i)$), the damping turns to be much weaker first then stronger, while the resistive GAM real frequency rises. On the other hand, with a fixed relative collision rate (ω_χ/ω_{De} holds), the larger b_s is, the higher resistive GAM real frequency Re(ω_{GR}) is, but weaker Im(ω_{GR}) damping is. In addition, T_i/T_e ratio can modify resistive GAM frequency ω_{GR} monotonously as well. Such calculation can be used as a reference for the further experiments investigation of GAM.

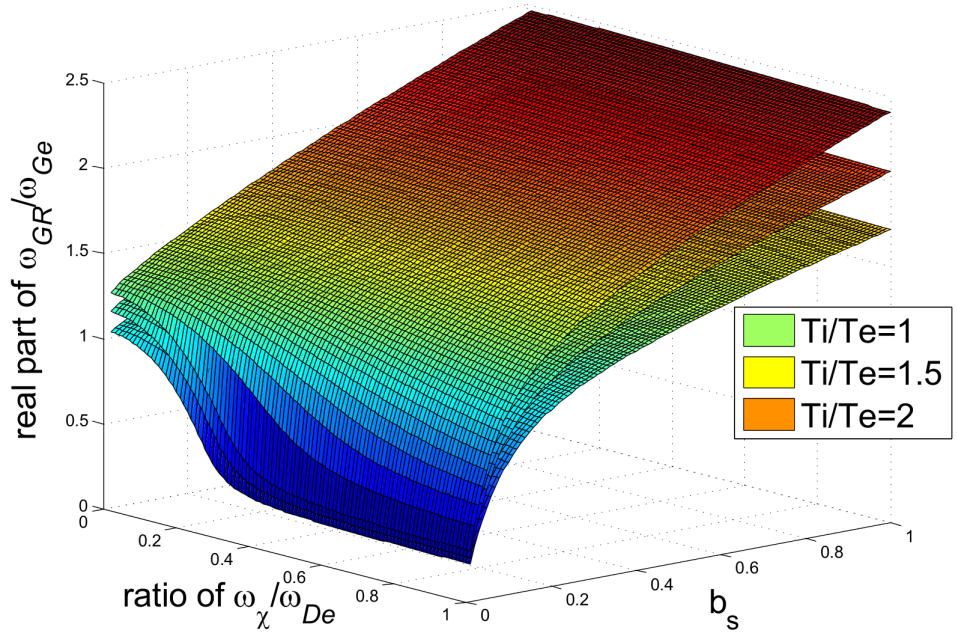

(a) Real solution part of the relative resistive GAM frequency ω_{GR}/ω_{Ge}.

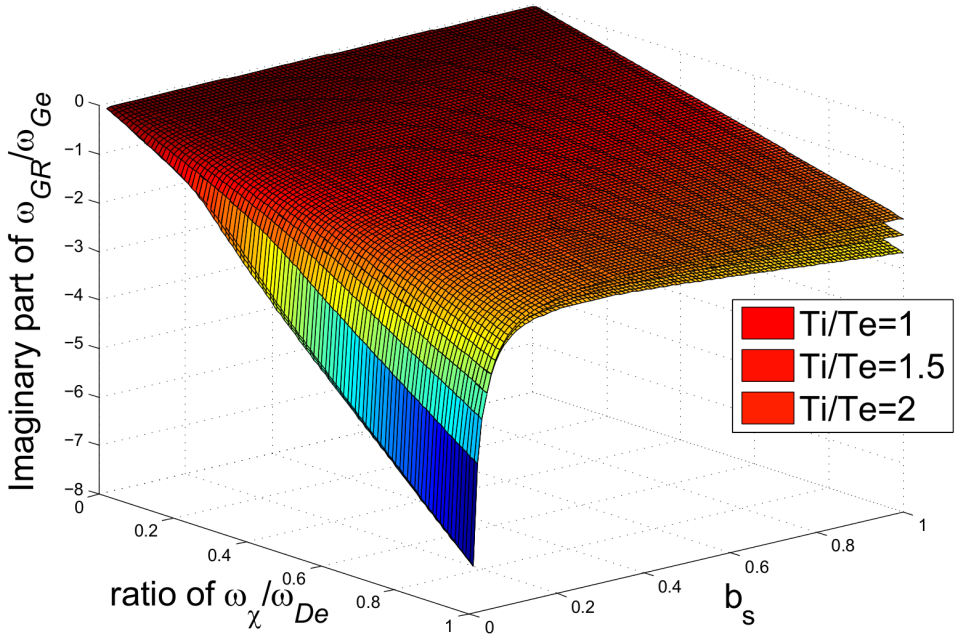

(b) Imaginary solution part of the relative resistive GAM frequency ω_{GR}/ω_{Ge}.

Figure 3.2: Relative resistive GAM frequency diagram. The ω_{GR}/ω_{Ge} ratio diagram in terms of b_s and ω_χ/ω_{De}.

CHAPTER 4

STOR-M TOKAMAK AND DIAGNOSTICS

The Saskatchewan Torus-modified (STOR-M) is a small plasma research tokamak designed and built at the University of Saskatchewan. It is the only active tokamak in Canada presently contributing to magnetic fusion research. It is the updated device following the plasma Betatron, STOR-1, and the STOR-1M. The completion of STOR-M construction can be dated back to 1987, and the first research experiments in STOR-M started in 1990. To this day, over 250,000 discharges have been performed for numerous experiments on various fusion research topics, such as turbulent heating operation, H-mode transitions, plasma biasing, Compact Toroid(CT) injection fueling, MHD and density fluctuations, plasma flow measurements, and alternating current (AC) operation. Table 4.1 lists the main parameters' typical values or maximum ranges of STOR-M.

Parameter Items	**Symbols**	**Values**(Maximum)
Major radius	R_0	46 cm
Minor radius	a	$12 \sim 13$ cm (depending on the vertical or horizontal direction.)
Toroidal B field	B_ϕ	1 T
Plasma current	I_p	$30 \sim 50$ kA
Electron density	n_e	$1 \sim 3 \times 10^{13} cm^{-3}$
Electron temperature	T_e	$2 \sim 300$ eV
Ion temperature	T_i	$50 \sim 100$ eV
Discharge duration	t_d	50 ms
Energy confinement time	τ_E	$1 \sim 5$ ms

Table 4.1: STOR-M Parameters

4.1 Introduction to STOR-M Tokamak

The STOR-M tokamak is equipped with ceramic breaks to separate the chamber electrically into 2 halves. The bellows are affiliated to release the mechanical stress on those breaks and facilitate examination to the inside of the chamber. A side view of STOR-M is shown in Figure 4.1.

The plasma boundary of the STOR-M tokamak is confined by two sets of stainless steel limiters. There are a set of horizontal rail limiters at the top and bottom of the tokamak cross-section with radial position $r = 12$ cm; alongside another set of partial circular limiters with $r = 13$ cm radius positioned as shown in Figure 4.2.

This configuration of limiters allows the plasma column to shift slightly (± 1 cm horizontally) without disturbing the plasma confinement. The inner minor radius of the STOR-M chamber is 15.8 cm with a 0.4 cm thick stainless steel wall. The space between the limiters outer side and the chamber wall is the cooler edge of plasma, called the scraped-off layer (SOL). In STOR-M, the SOL region is large enough for experimental studies.

The vacuum pumping system in STOR-M contains a rotary pump as the primary evacuation stage. This rotary pump is connected to a large turbo-molecular pump via a valve for advanced evacuating down to 1×10^{-7} Torr, the base pressure. In the normal operation status (after the glow discharge conditioning), the vacuum chamber will be filled with ultra pure hydrogen (99.999%) to 1.2×10^{-4} Torr pressure.

4.2 Diagnostics in STOR-M Tokamak

The STOR-M tokamak chamber has 16 ports for various diagnostics, gas feeding and pumping, including 9 horizontal ports, 6 sets of vertical ports and one tangential port (Figure 4.3). In 1995, an additional port connecting the Compact Torus Injector(CT),a new fueling technique presently in its experimental stage, was installed.

The recent diagnostic arrangements in the STOR-M tokamak experiments described in Table 4.2 correspond to the ports indicated in Figure 4.3. Detailed explanations of the major diagnostics principles will be introduced hereafter.

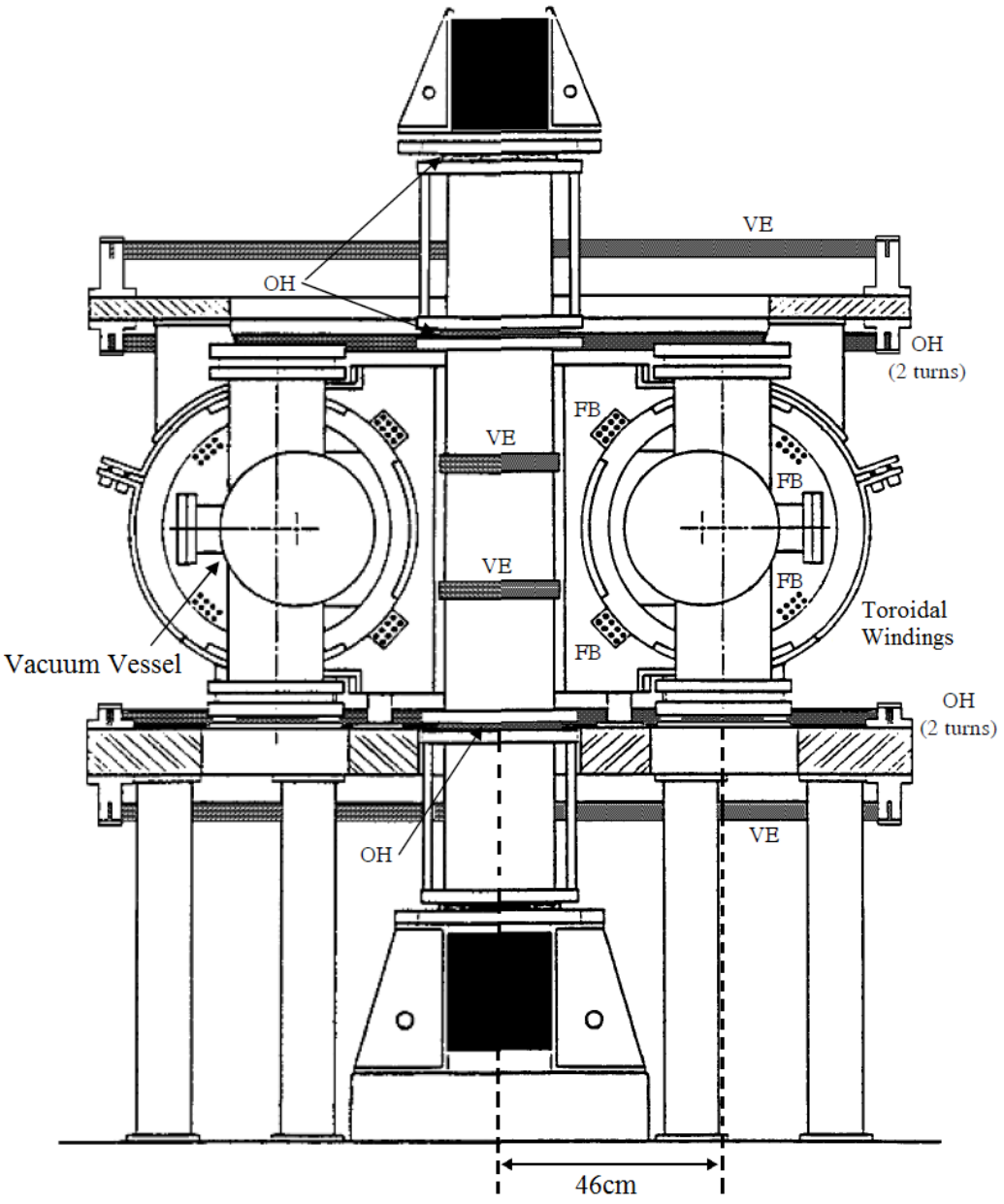

Figure 4.1: Side view of the STOR-M tokamak configuration [1]. OH: Ohmic primary coils (8 turns); VE: Vertical Equilibrium field coils; FB: coils for feedback plasma position control and induction coils for fast turbulent heating current.

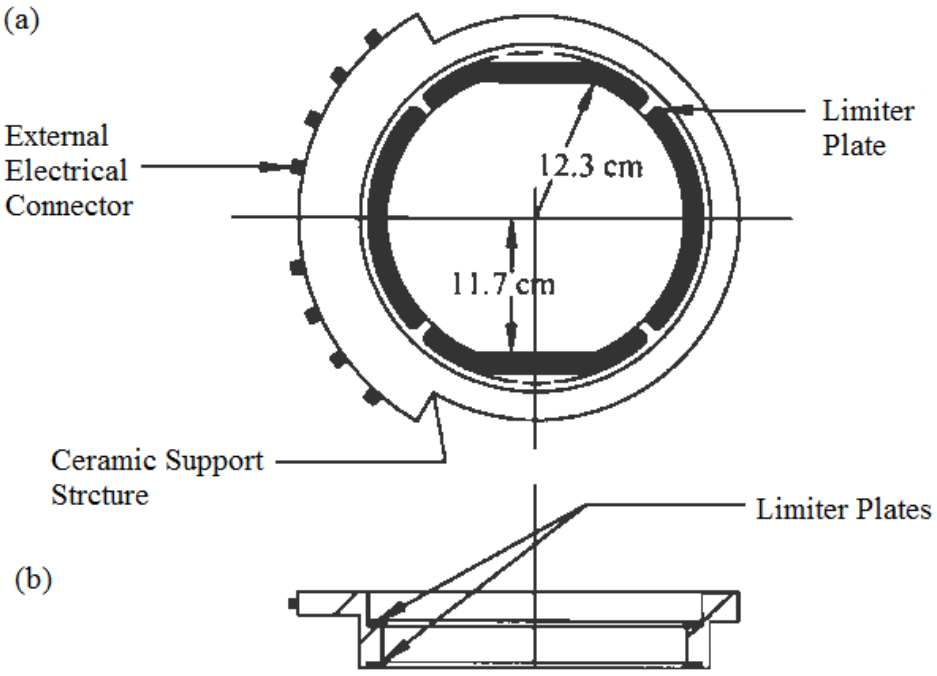

Figure 4.2: Limiter configuration in STOR-M [40]. (a) vertical cross-section view; (b) horizontal cross-section view.

Diagnostics/Subsidiary Devices	Ports Number
Glow discharge and biasing electrode	2
Spectroscopy	3
Soft X-ray camera	4
Microwave Interferometer	14
Probes	5,7-1,7-2,11
Ion Doppler Spectroscopy camera	10,3,11
PMT camera	13

Table 4.2: STOR-M Diagnostics Arrangement

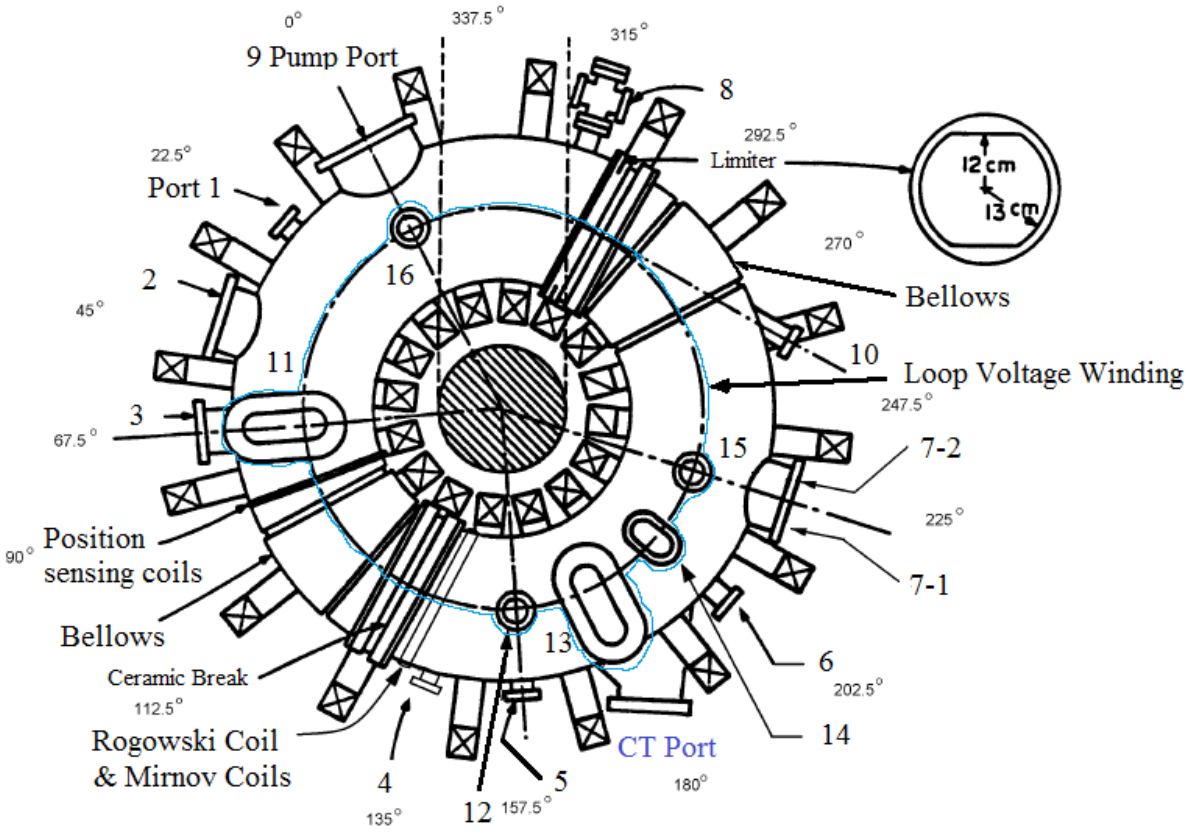

Figure 4.3: Top view of the STOR-M tokamak with the ports configuration.

4.2.1 Loop Voltage Measurement

Loop voltage is one of the basic operational parameters for takamaks. It monitors the total voltage arising from both the resistance and the inductance of plasma, which is given by:

$$V_p = I_p R_p + \frac{d}{dt}\left(I_p L_p\right), \tag{4.1}$$

where I_p is the plasma current, R_p is the average plasma resistance, and L_p is the plasma inductance. In a tokamak, the average plasma resistance R_p can be expressed as

$$R_p = \overline{\eta}\frac{2R_0}{a^2}, \tag{4.2}$$

where R_0 is the major radius of the plasma column, a is its minor radius and $\overline{\eta}$ is the average plasma resistivity. Meanwhile, the plasma inductance follows as:

$$L_p = \frac{4\pi}{c}R_0\left[\ln\left(\frac{8R_0}{a}\right) + \frac{l_i}{2} - 2\right], \tag{4.3}$$

where l_i is the plasma self inductance parameter. It is defined by

$$l_i = \frac{\overline{B_\theta^2}}{B_\theta^2(a)} = \frac{2\int_0^a (B_\theta^2(r) r dr}{a^2 B_\theta^2(a)}, \tag{4.4}$$

where $B_\theta(r)$ is the poloidal magnetic field as a function of radial distance, r, from the center of the plasma column, and $B_\theta(a)$ is the poloidal magnetic field at the plasma edge, $r = a$. When the plasma current is not varying rapidly, the inductance contribution to the loop voltage can be ignored, and then the loop voltage and the plasma current can be used to estimate the plasma resistivity η. Then the averaged electron temperature in tokamak can be expressed as [41]:

$$T_e \approx 4.64 \times 10^{-4}\frac{Z_{eff}\ln\Lambda}{\eta_s}[eV], \tag{4.5}$$

where the Spitzer resistivity $\eta_s \approx \eta$, Z_{eff} is the effective ion charge, and the Coulomb logarithm $\ln\Lambda \approx 15$ in STOR-M.

In the STOR-M tokamak, the plasma loop voltage is measured by a single loop on top of the

vacuum chamber (this is the blue loop shown in Figure 4.3). The loop is made of a RG 59/U coaxial cable with 1.2 Ω inner-resistance and 12 μH inner-inductance. The output voltage is attenuated by a $101:1$ voltage divider, and then sent to the data acquisition system in the control room. The schematic measurement diagram is shown in Figure 4.4.

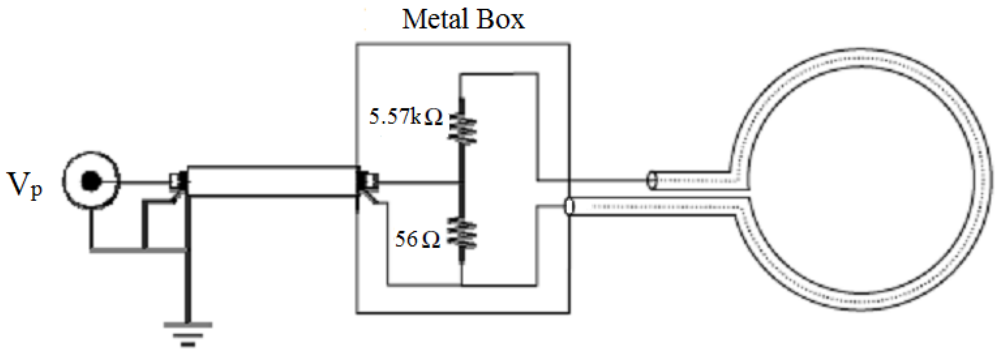

Figure 4.4: The schematic diagram of the loop voltage measurement in STOR-M [1].

4.2.2 Rogowski Coil

In the STOR-M tokamak, Rogowski coils are commonly used to measure the different AC currents in the plasma. Each coil has a frequency response up to 800 kHz, which far exceeds the measurement requirements in STOR-M. A Rogowski coil consists of N turns of wire wound around a circular non-magnetic insulator frame, such as Teflon. A typical Rogowski coil is illustrated in Figure 4.5, where A is the area of a small loop in the windings.

When a current I passes through the coil, the generated circular magnetic field B_θ is perpendicular to the small loop's cross section A. According to Faraday's law of induction:

$$\oint_{l_S} \mathbf{E} \cdot d\mathbf{l} = -\frac{1}{c} \int_{S_{tot}} \frac{\partial \mathbf{B}_\theta}{\partial t} \cdot d\mathbf{S}, \tag{4.6}$$

where

$$V_{Rog} = \oint_l \mathbf{E} \cdot d\mathbf{l}, \tag{4.7}$$

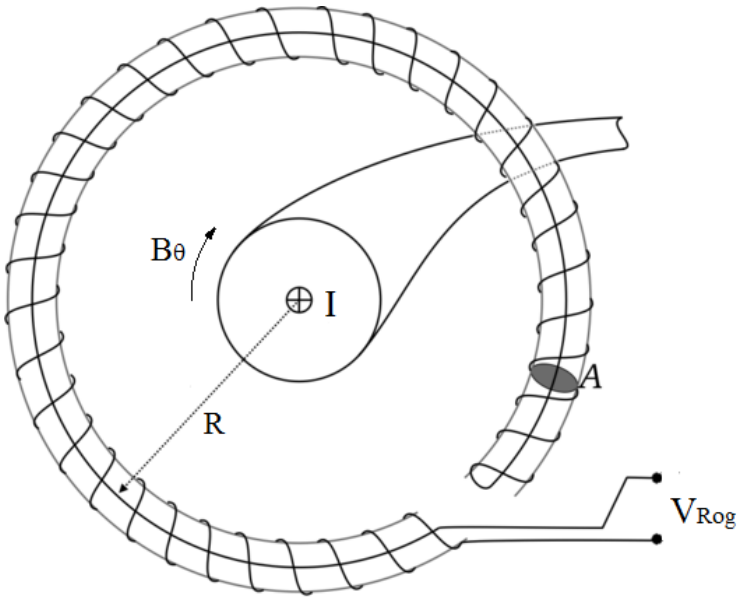

Figure 4.5: A typical Rogowski coil for current measurement.

and

$$-\frac{1}{c}\int_{S_{tot}} \frac{\partial \mathbf{B}_\theta}{\partial t} \cdot d\mathbf{S} = \frac{4\pi}{c^2}\frac{AN}{l}\frac{dI}{dt}. \tag{4.8}$$

where $l = 2\pi R$ if the current is at the center of the loop. Therefore, the voltage produced by a Rogowski coil is

$$V_{Rog} = \frac{4\pi}{c^2}\frac{AN}{l}\frac{dI}{dt}. \tag{4.9}$$

Then the current I enclosed by a Rogowski coil can be determined by integration of the induced Rogowski voltage V_{Rog}.

Table 4.3 shows the basic parameters of all the Rogowski coils installed in STOR-M, which were calibrated against a commercial Rogowski coil made by Pearson Electronics. The accuracy of each coil is within 5% [1].

4.2.3 Mirnov Coils

A Mirnov coil is a modified Rogowski coil with a specific spacial arrangement around the former, which makes the coils sensitive mainly to the specific modes of B_θ oscillations. This is

Measured Current	Resistance R [Ω]	Inductance L [mH]	N [turns]	Major Radius R R[cm]	A [cm^2]	Calibration [kA/V]
I_p	1.4	0.12	600	17	3.5	100
I_{BT}	70	7.5	1187	7	3.75	10
I_{OH}	37	5.3	750	7	3.75	10
I_{VE}	84	9.6	1187	7	4.95	10
I_{th}	4	0.02	180	17	3.5	100

Table 4.3: The STOR-M Rogowski Coils Parameters

because B_θ in tokamaks can be Fourier expanded as

$$B_\theta(\theta) = B_0 + \sum_{m=1}^{\infty}(C_m \cos m\theta + S_m \sin m\theta), \tag{4.10}$$

Figure 4.6 presents a Mirnov coil spacial configuration to measure $m = 2$ mode oscillations. Four coils are connected in series with certain polarities and separated evenly 90° apart in the poloidal direction for this case.

In the STOR-M tokamak, three sets of Mirnov coils are installed for up to $m = 6$ modes measurements (12 coils separated evenly in poloidal direction). The flat frequency response of those coils can reach 200 kHz, which is sufficient for MHD oscillations signals (<60 kHz). In MHD studies on STOR-M, we usually only consider up to $m = 3$ modes measurements, because they are the dominant modes of MHD oscillations.

4.2.4 Position Sensing Coils

In order to get a stable discharge in STOR-M for an experiment, the dedicated position control of the plasma within the vacuum vessel is essential. Four (two pairs) Mirnov coils are oriented in a circle of plasma radius r =17 cm to detect the poloidal magnetic field B_θ. They are separated poloidally by 90° as shown in Figure 4.7.

Each of the magnetic coils has 460 turns of 38 AWG enameled wire winding around a cylin-

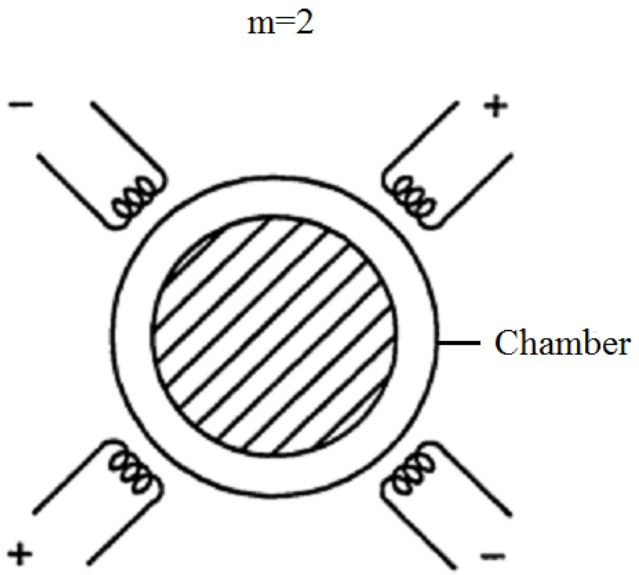

Figure 4.6: The spacial configuration for $m = 2$ mode Mirnov coil in STOR-M [2].

drical Teflon former. The resistance and the inductance of each coil is about 22 Ω and 1 mH. The frequency response of such coils can reach up to 20 kHz which is sufficient for the purpose of plasma position control. The coil signals are sent to the control room via RG 58U coaxial cable. After integration of those coil signals, the signals are proportional to the magnetic field at the probe location produced by the plasma current:

$$B_i = \frac{\Phi_i}{A_i} = \frac{-\int V_i dt}{\pi a_i^2}, \tag{4.11}$$

where a_i is the radius of the i^{th} coil's cross-section, and V_i is the voltage signal from the i^{th} coil. Each pair of the integrated signals (up-down, in-out) are compared via an analog circuit. The output signals will be proportional to the plasma displacement, which can be used as feedback signals for the plasma position control.

4.2.5 Soft X-ray (SXR) Imaging

In a high temperature plasma, such as a tokamak plasma, there are three radiation sources for the soft X-ray (SXR) emission - bremsstrahlung, recombination and line radiation. The bremsstrahlung radiation produced by the deceleration or acceleration of electrons when the electron-ion Coulomb

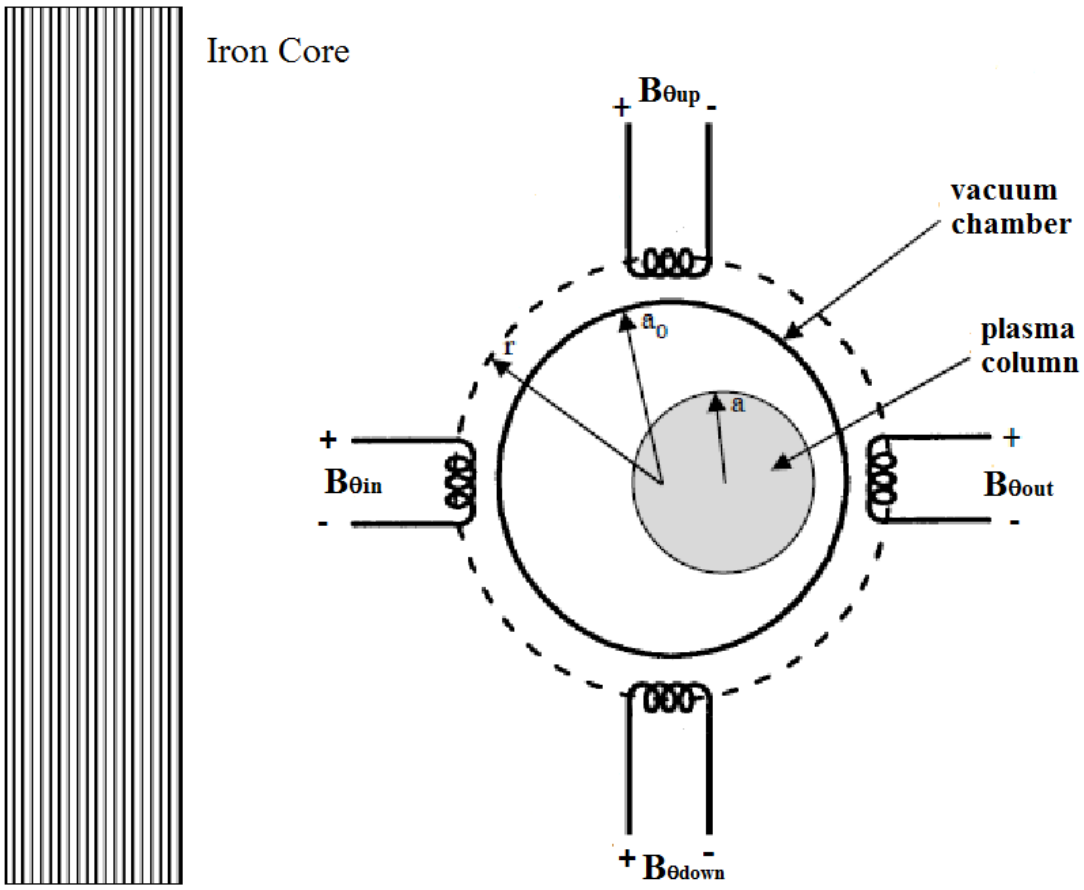

Figure 4.7: The orientation diagram of plasma position sensing coils in STOR-M [1].

collision occurs. While the recombination radiation is produced when a free electron in a plasma is captured by an ion. Both of them have the continuum SXR radiation spectrum, whose intensity relates to the plasma density n_e and electron temperature T_e as

$$I(E, T_e) \propto n_e^2 T_e^{-1/2} Z_{eff} \exp^{-E/k_B T_e}, \tag{4.12}$$

where E is the x-ray energy and Z_{eff} is the effective ion charge of the plasma. Obviously, the higher the density and electron temperature is, the stronger the SXR spectrum intensity is. This relationship can be used to estimate the local plasma density and the electron temperature information.

For the SXR line spectrum of plasma, the radiation is mainly generated by the inner shell transitions in partially ionized impurities. So the line radiation spectrum can be used to identify the species and ionization states of the impurities.

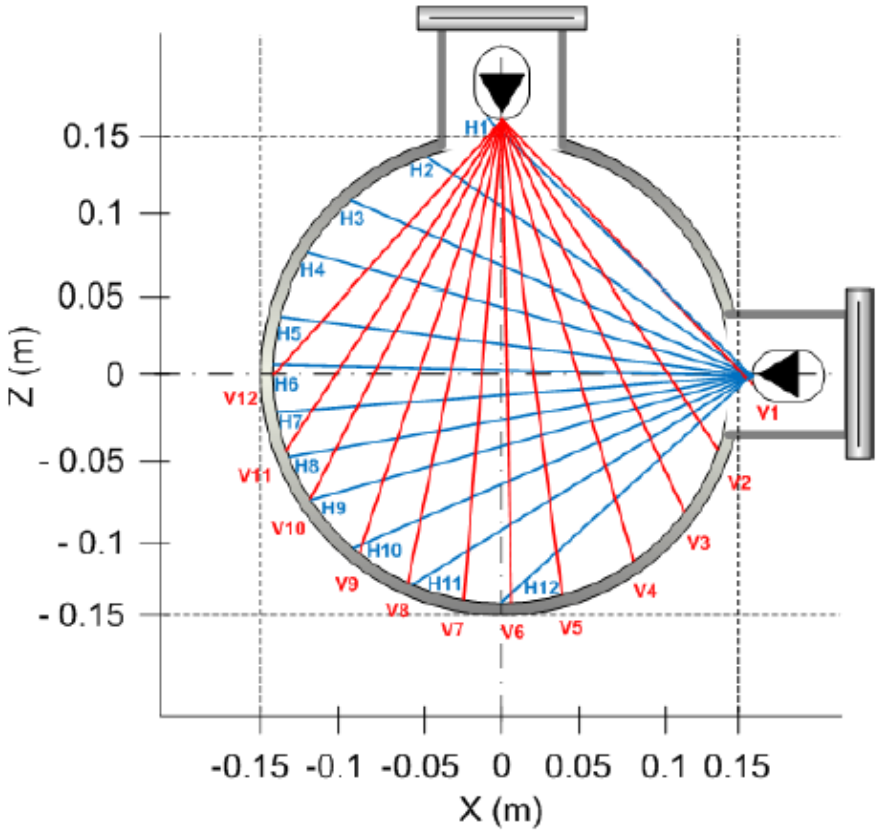

Figure 4.8: The schematic of soft X-ray imaging system in STOR-M [3].

In STOR-M, a SXR imaging system composed of two arrays of 12 detectors are installed to detect line integral radiation energy intensity from SXR emissions as Figure 4.8. Such configuration covers the whole poloidal cross section with good spatial resolution (2 cm) and minimum overlap. Owing to the plasma central region has higher density and electron temperature, the line integral SXR spectrum intensities reflect the central plasma information predominantly. The time resolution of this imaging system is in the order of a few μs, which is accurate enough to monitor plasma perturbations and movements in the central hot plasma region.

4.2.6 Spectrometer

Spectrometer is a common diagnostic to monitor the line emissions from impurities and hydrogen, which is a qualitative indicator of the confinement and purity states of plasma. In tokamak, the H_α emission line (6562.8 Å) is a good indicator of the recycling process of the plasma particles at the edge region. Low level H_α emission at the edge indicates the good plasma confinement status. In STOR-M, a 0.35 m focal length single-pass Czerny-Turner grating monochromator (Heath EU-700) is used to monitor the H_α emission line. The monochromator has a relative aperture of f/6.8 with 1 Å resolution in UV-VIS region. A fiber optical bundle with optical lenses is mounted on a horizontal port in the STOR-M mid-plane. which is used to collect and transmit the radiation light from plasma to the spectrometer's10 μ m $\times$ 3 mm entrance slit. Figure 4.9 shows the schematic of the H_α spectrometer system in STOR-M. In order to collect the dispersed emission light, a photomultiplier (RCA IP-28) is installed with μ-metal shield and the brass and copper housing from the magnetic field.

4.2.7 Microwave Interferometer

Microwave interferometer is used to detect the chord averaged plasma density evolution of a tokamak based on the electromagnetic wave propagation theory in plasma. In a plasma, the local refractive index μ for an O-mode electromagnetic wave (i.e. where the electric field of the wave is parallel to the magnetic field in the plasma), is determined by the local electron density n_e and the

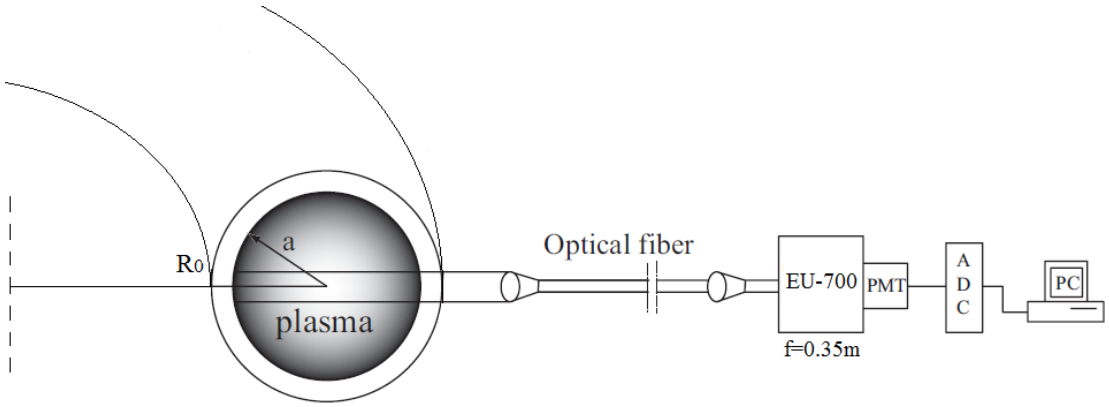

Figure 4.9: The schematic of H_α spectrometer system in the STOR-M tokamak.

wave frequency ω through the relationship,

$$\mu(r) \equiv \frac{k(r)c}{\omega} = \sqrt{1 - \frac{\omega_p^2(r)}{\omega^2}} = \sqrt{1 - \frac{n_e(r)}{n_c}} \approx 1 - \frac{n_e(r)}{2n_c}, \tag{4.13}$$

where ω_p is the plasma frequency, and the cutoff density of plasma n_c is

$$n_c = \frac{m_e \omega^2}{4\pi e^2}, \tag{4.14}$$

with m_e as the electronic mass. When an O-mode microwave signal passes through a plasma in a tokamak, it undergoes a phase shift $\triangle\phi$ due to the plasma, which can be approximated by:

$$\begin{aligned} \triangle\phi &= \int_{-a}^{a} (1 - \mu(r)) \frac{\omega}{c} dr \\ &= \frac{\omega}{c} \int_{-a}^{a} [1 - \sqrt{1 - \frac{n_e(r)}{n_c}}] dr \\ &\approx \frac{\omega}{2cn_c} \int_{-a}^{a} n_e(r) dr, \end{aligned} \tag{4.15}$$

If the plasma is assumed to be sufficiently stationary compared with the wave frequency, then the chord line averaged plasma electron density can be measured if the phase shift is detectable. This is because:

$$\overline{n_e} = \frac{1}{2a} \int_{-a}^{a} n_e(r) dr \approx \frac{cn_c}{\omega a} \triangle\phi, \tag{4.16}$$

In this theory, the cutoff frequency n_c should be large enough that $n_e \ll n_c$.

The microwave interferometer system in STOR-M uses 4 mm, 76 GHz microwaves generated by a 100 mW IMPATT oscillator (ELVA-1). The initial signal is split by 10 dB directional couplers into E_p, E_{R1} and E_{R2} to travel along three paths individually as shown in Figure 4.10.

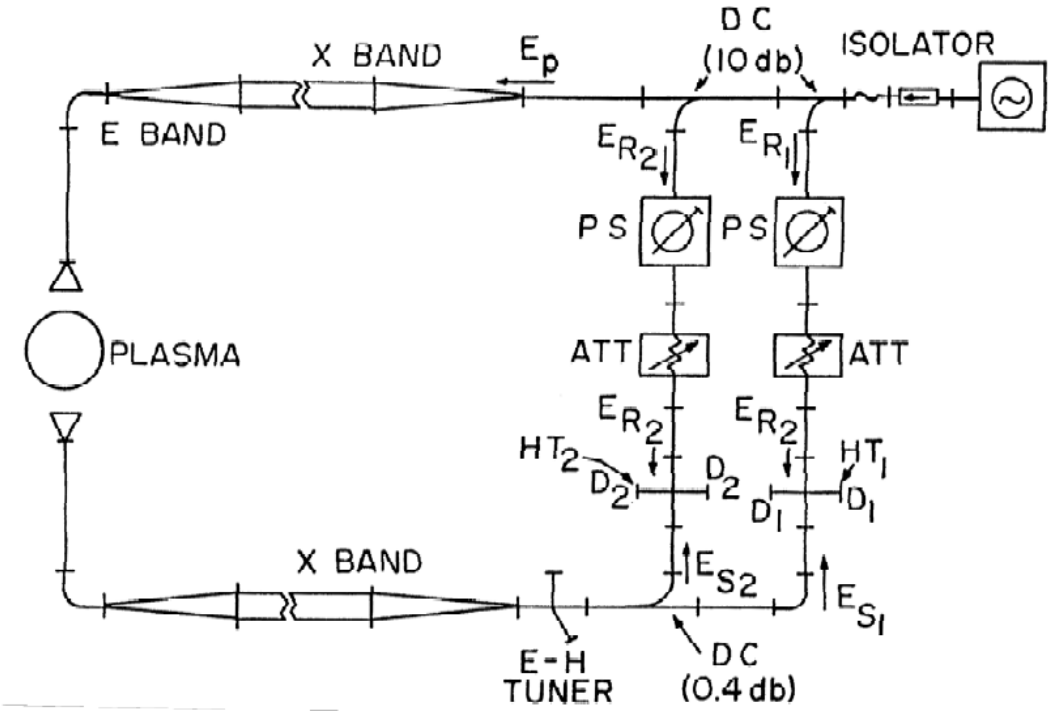

Figure 4.10: The schematic of microwave interferometer system in STOR-M [1].

After passing through the plasma in the tokamak, the E_p signal passes through an E-H tuner, and is then split into E_{S1} and E_{S2} signals. At the same time, the reference signals E_{R1} and E_{R2} are modulated by a phase sifter and an attenuator. After that, E_{S1} and E_{S2} signals are each mixed with modulated reference signals E_{R1} and E_{R2} in hybrid tees, respectively. The outputs are detected by 4 diodes and then fed into adjustable buffer amplifiers for compensation. The final output signal is given by:

$$V_{1,2} = K_{1,2} \cos \theta_{1,2}, \tag{4.17}$$

where $\theta_{1,2}$ are the phase difference of the detected microwaves. With proper adjustments of the modulators and circuits, the outputs can become:

$$V_1 = K_1 \sin(\triangle\phi), \tag{4.18}$$

and

$$V_2 = K_2 \cos(\triangle\phi), \tag{4.19}$$

where $\triangle\phi$ is the phase shift caused by the plasma. By measuring these two signals, the plasma phase shift $\triangle\phi$ is determined. A direct-reading fringe counting circuit [42] is used to measure $\triangle\phi$, and thus the line averaged plasma density is obtained according to Eq. 4.16.

4.2.8 Probes

Probes are one of the most widely used measurement tools in various plasma studies. They are favoured by researchers because: 1) They can be designed to measure a broad range of plasma parameters, such as the electron density, the electron/ion temperatures, the floating potential, and plasma flow velocities. 2) They are relatively inexpensive, simple to make and easy to use. 3) They have good spatial resolutions, and some of them have enough time sensitivity for plasma fluctuation studies as well. However, the probes are restricted to the cool edge plasma studies in tokamak due to the upper limit of high temperature resistant conducting material.

Single Langmuir Probe

In the STOR-M tokamak, the single Langmuir probe is most commonly used for measurements of electron density n_e, electron temperature T_e, floating potential V_f and plasma potential V_p in the cool edge region. As its name implies, the single Langmuir probe consists of one electrode with a biasing ramp voltage. The I-V curve is obtained by measuring the current through it, and the local plasma parameters can be extracted from the I-V curve, as shown in Figure 4.11.

Theoretically, the total current through the electrode is the sum of the ion and electron currents:

$$I = I_{is}(-1 + e^{e(V_b - V_p)/k_B T_e}), \tag{4.20}$$

where k_B is Boltzmann constant, V_b is the electrode potential with respect to ground, V_p is the local plasma potential with respect to ground, and T_e is the electron temperature. I_{is} is the ion saturation current, which is the limiting current when a large enough negative potential is applied

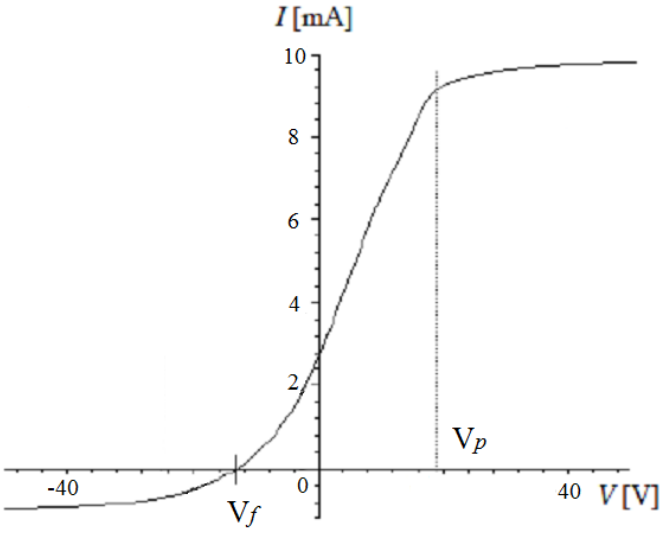

Figure 4.11: A typical single Langmuir probe I-V characteristics diagram.

on the electrode in a plasma. It is given by

$$I_{is} = e^{-1/2} q n_e \sqrt{\frac{k_B T_e}{m_i}} A_s, \tag{4.21}$$

where m_i is the ion mass, and A_s stands for the effective area of the probe sheath. The factor $e^{-1/2}$ is due to the reduction of the ion density in the pre-sheath when $T_e \gg T_i$ [43]. If T_e is comparable to T_i, then the factor becomes $\sqrt{1/2\pi}$.

From the floating potential V_f, we can calculate the electron temperature T_e, since

$$V_f = -\frac{k_B T_e}{2|e|} \ln \frac{m_i}{2.3 m_e}, \tag{4.22}$$

Assuming A_s is about the electrode tip's area, the electron density n_e can be assessed from Eq. 4.21.

However, the measured voltage V is usually the potential difference between the electrode and the reference ground, such as the vacuum chamber wall. Normally, $V = V_R + V_b$, where V_R is the potential difference between the plasma and the reference ground. V_R is changeable in different environments, so V varies with V_R, which reduces the accuracy of the single probe

method. Another disadvantage of the single probe is the poor time resolution. In order to avoid the possible smoothing out of plasma fluctuation signals, the instantaneous accurate I-V curve needs to be recorded, which requires the sweeping frequency to be greater than the fluctuation frequency but below the ion cyclotron frequency. However, the circuit for a fast sweeping probe is sophisticated, sensitive and expensive.

One application of single Langmuir probes in the STOR-M tokamak is Rake probe, which is an array of 16 single Langmuir tips made of tungsten. Figure 4.12 shows its basic structure. The rake probe is mounted on a linear and rotary manipulator to achieve plasma parameter profile measurements.

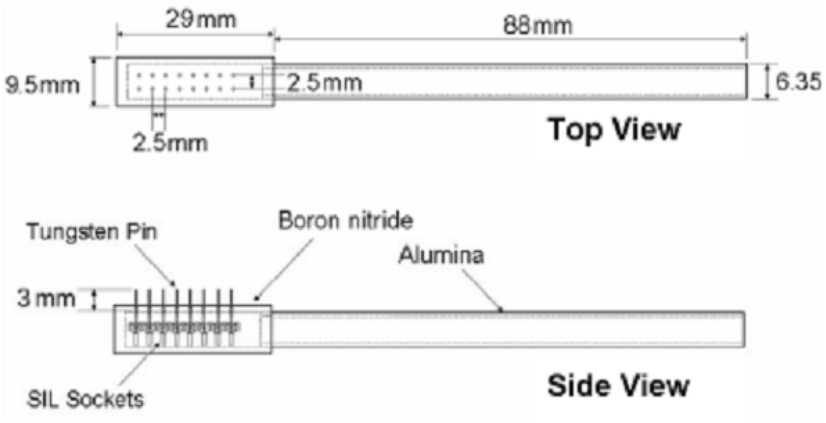

Figure 4.12: The structure of Rake probe in STOR-M [4].

Retarding Field Energy Analyzer (RFEA) Probe

The Retarding Field Energy Analyzer (RFEA) is a simple and reliable diagnostic technique to measure the ion temperature in the Scrape-Off Layer (SOL) and edge of magnetic fusion devices. The STOR-M RFEA consists of an electrode with an orifice, two grids and a collector plate. All conducting elements (orifice, grids and collector) are electrically isolated and can be biased independently, as shown in Figure 4.13.

The sheath of the entrance slit repels low energy electrons and accelerates ions into the analyzer. The voltage at grid 1, V_{G1}, is swept, only ions with energy greater than qV_{G1} will be collected. The lowest negative bias is applied to the grid 2, and it suppresses the secondary electrons emitted from the collector and the grids. It also repels residual high energy electrons coming

from the entrance slit. The collector is negative biased(but not as much as the grid 2) to ensure good ion collections. Assuming the velocity distribution is Maxwellian, the collected ion current I_i as a function of retarding potential V_{G1} for hydrogen plasma is given by

$$\begin{aligned} I_i(V_{G1}) &= I_{i0}, V_{G1} \leq V_{shift} \\ I_i(V_{G1}) &= I_{i0} e^{e(V_{G1}-V_{shift})/k_B T_i}, V_{G1} > V_{shift}, \end{aligned} \tag{4.23}$$

where I_{i0} is the current collected when none of the ions are repelled by the retarding potential V_{G1}, and V_{shift} is the potential difference between the plasma potential and the probe ground. So the logarithmic slope of the $\ln(I_i) - V_{G1}$ characteristic line can give the ion temperature T_i.

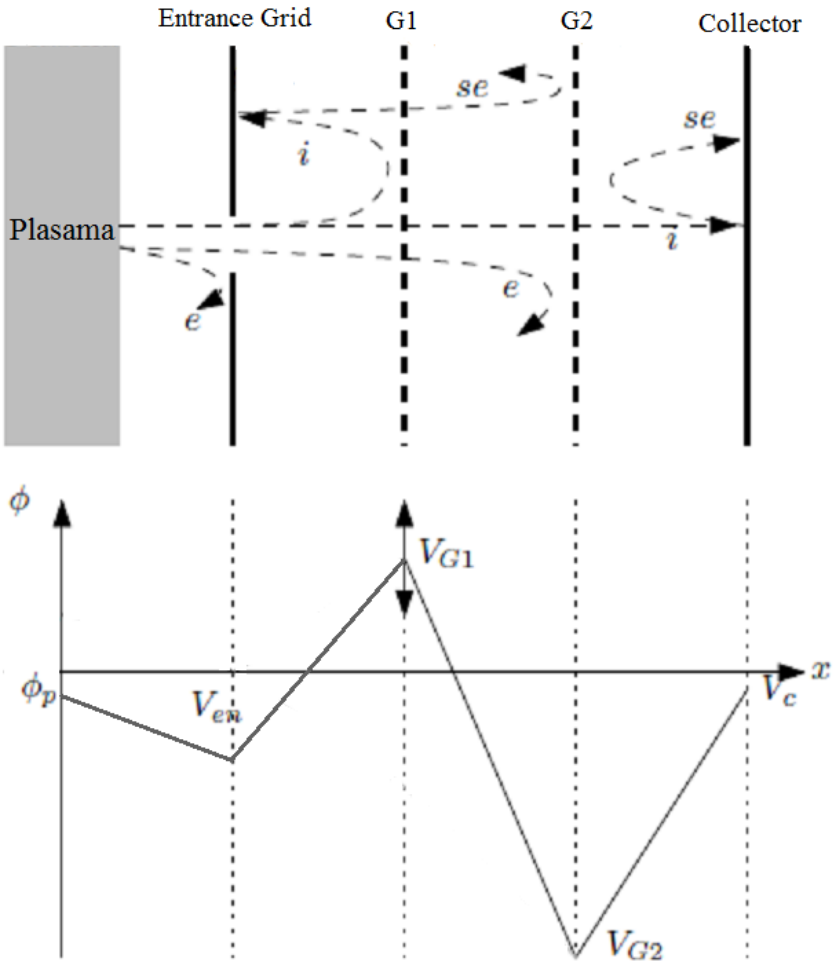

Figure 4.13: Configurations diagram of RFEA with biasing scheme in the STOR-M tokamak [5].

CHAPTER 5

EXPERIMENTAL DESIGN FOR GAM STUDY IN THE STOR-M TOKAMAK

As discussed in previous chapters, the classical Winsor's GAM theory has limitations in its assumption. It promoted the reinvestigation of the GAM theory in terms of two-fluid analysis, and a resistive GAM theory was proposed as a result. To confirm the validity of this new model, experimental proof is needed. In this chapter, a description of the experimental system design for the resistive GAM study in the STOR-M tokamak is addressed in detail.

The experiments for GAM study were carried out in STOR-M in 2006. However, the results are not conclusive with a GAM-like frequency at about 10 kHz, which is lower than the classical GAM theory prediction. The real GAM frequency is possibly higher than 10 kHz in STOR-M. Before a GAM study can be done on STOR-M, the GAM phenomenon itself must be seen experimentally.

5.1 Density Fluctuation Measurement Methods

From the descriptions in Chapter 2 and Chapter 3, we already know that GAM has a characteristic that its mode structure for density fluctuations is (m, n) =(1,0) (while the mode structure for the electrostatic potential is (m, n) =(0,0)). Meanwhile, the experimental reports from other large tokamaks reveal that GAM is an edge phenomena in L-mode operation. Those features make the accurate poloidal measurements of the density fluctuations at the tokamak plasma edge critical in the search of GAM.

There are several methods for the density fluctuation measurements in tokamaks, such as various Langmuir probes, Reflectometry, Heavy Ion Beam Probe (HIBP). For small tokamaks like

STOR-M with limited funding, the Langmuir probes seem to be a better choice for the first round of experiments, especially since GAMs usually appear in the edge plasma of tokamaks. In order to guarantee a good time resolution for the experiments, the measurements of electron temperature T_e and ion saturation current I_{is} need to be carried out simultaneously with a good time resolution. Therefore, it is necessary to use triple probes, and DC biased double probe or single probe to investigate the plasma density fluctuations.

5.1.1 Double Probe

If the electrode is biased relative to a second electrode instead of the ground, it becomes a basic double probe. Figure 5.1 represents the basic circuit and the typical I-V curve for a double probe. The principle of the double probe is similar to that of the single probe. However, since the whole circuit system is floating and the two electrodes are assumed identical to each other, the current through one electrode is the negative of the current through the second. This is why a typical I-V curve is symmetric with respect to the origin in Figure 5.1(a). It is noticed that the current is limited to the range $-I_{is} \sim I_{is}$, where I_{is} is the ion saturation current as Eq. 4.21.

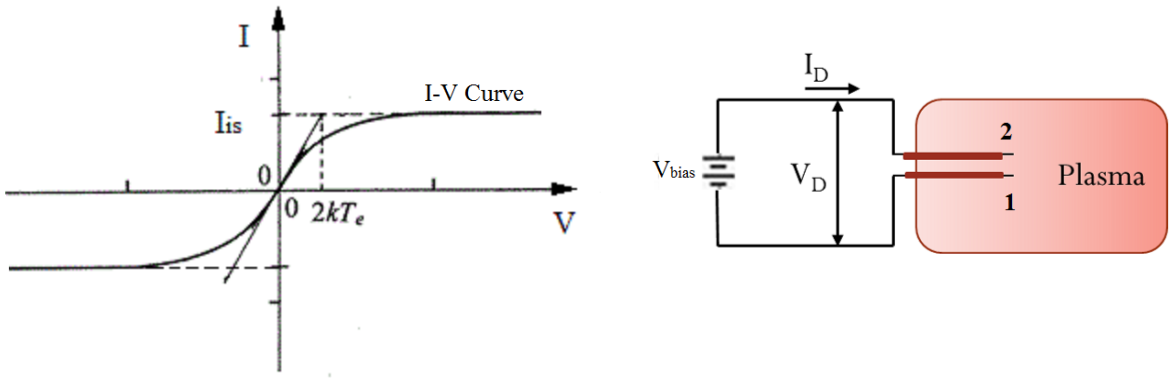

(a) Typical I-V curve. (b) Basic circuit configuration.

Figure 5.1: Ideal I-V curve and basic circuit for double probe.

The current through an electrode is given by

$$\begin{aligned} I_D &= I_{is}(-1 + e^{e(V_1 - V_p)/k_B T_e}) \\ &= -I_{is}(-1 + e^{e(V_2 - V_p)/k_B T_e}). \end{aligned} \tag{5.1}$$

If the plasma is uniform, the voltage difference between two electrodes is $V_D = V_2 - V_1$, and the detected current can be written as

$$I_D = I_{is} \tanh\left(\frac{1}{2}\frac{eV_D}{k_B T_e}\right). \tag{5.2}$$

Taking the derivative of Eq. 5.2 yields

$$\frac{dI_D}{dV_D}|_{I_D=0} = \frac{eI_{is}}{2k_B T_e}. \tag{5.3}$$

According to the Eq. 5.3, the electron temperature T_e can be obtained by the slope calculation of the I-V curve at the origin. After knowing the electron temperature T_e and the ion saturation current I_{is}, the electron density n_e can be calculated from Eq. 4.21. If the electron temperature T_e is known by another method, the electron density n_e can be measured simply by applying a large DC bias in the double probe circuit.

5.1.2 Triple Probe

The triple probe is developed from the double and single probes and combines the advantages of them both. The basic configuration consists of a double probe with a fixed DC bias and another floating electrode to measure the floating potential directly, as shown in Figure 5.2.

In order to obtain the electron density n_e, the fixed bias should be large enough to draw the ion saturation current I_{is} from the plasma. The rule of thumb is that the voltage bias V_{bias} is supposed to be at least 3 times of the expected electron temperature in eV, $-eV_R > 3k_B T_e$.

According to the single probe theory, the current of any electrode can be described as

$$I_p = -I_e e^{e(V_b - V_p)/k_B T_e} + I_{is}, \tag{5.4}$$

where V_b is the electrode potential with respect to ground, V_p is the local plasma potential with respect to ground, and the current I_e is the electron saturation current, which is given by:

$$I_e = A_s n_e e \sqrt{\frac{k_B T_e}{2\pi m_e}}, \tag{5.5}$$

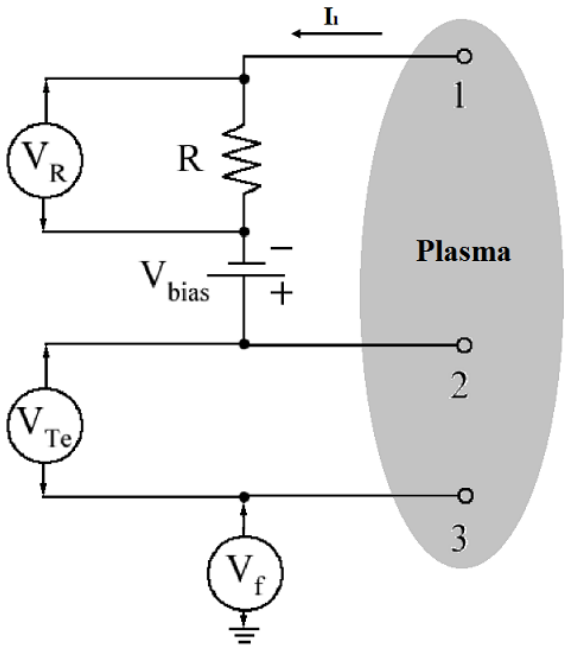

Figure 5.2: Configuration schematic for triple probe.

where A_s is the effective detecting surface (sheath surface) area of the probe.

Assuming three identical electrodes means each probe will have identical values for electron/ion saturation current and local electron temperature. The currents on each tip are

$$\begin{aligned} I_1 &= -I_e e^{e(V_1-V_p)/k_B T_e} + I_{is}, \\ I_2 &= -I_e e^{e(V_2-V_p)/k_B T_e} + I_{is}, \\ I_3 &= -I_e e^{e(V_3-V_p)/k_B T_e} + I_{is}. \end{aligned} \tag{5.6}$$

After substitution, their relationship can be expressed as

$$\frac{I_2 - I_3}{I_2 - I_1} = \frac{1 - e^{e(V_3-V_2)/k_B T_e}}{1 - e^{e(V_1-V_2)/k_B T_e}}. \tag{5.7}$$

If the double probe part is symmetric, accordingly, $I_2 = -I_1$ while $I_3 = 0$, Eq. 5.7 then can be simplified into

$$\frac{1}{2} = \frac{1 - e^{e(V_3-V_2)/k_B T_e}}{1 - e^{e(V_1-V_2)/k_B T_e}}, \tag{5.8}$$

where $V_D = V_2 - V_1$ is the voltage difference between the two biased electrodes. Considering the

bias rule, it is supposed that $eV_D \gg k_B T_e$, so Eq. 5.8 can be rewritten as

$$V_{T_e} = V_2 - V_3 = \ln 2 \frac{k_B T_e}{e}, \tag{5.9}$$

where V_{T_e} is the voltage difference between the positive biased electrode and the floating electrode. This equation is used to assess the local electron temperature T_e by measuring V_{T_e}.

Based on double probe theory, the current though the two biased the electrodes is given by

$$\begin{aligned} I_D &= I_{is}(-1 + e^{e(V_1 - V_p)/k_B T_e}) \\ &= -I_{is}(-1 + e^{e(V_2 - V_p)/k_B T_e}). \end{aligned} \tag{5.10}$$

If the plasma is uniform and $eV_D = e(V_2 - V_1) > 3k_B T_e$, the current becomes

$$I_D = I_{is} \tanh\left(\frac{1}{2}\frac{eV_D}{k_B T_e}\right) \simeq I_{is}. \tag{5.11}$$

Then the electron density n_e can be determined by measuring the current in the biased circuit $I_D \simeq I_{is}$, since the ion saturation current is proportional to the electron density n_e:

$$I_{is} = e^{-1/2} q n_e \sqrt{\frac{k_B T_e}{m_i}} A_s, \tag{5.12}$$

where m_i is the ion mass, and A_s stands for the effective detecting surface area of the probe. The factor $e^{-1/2}$ is due to the reduction of the ion density in the pre-sheath when $T_e \gg T_i$ [43].

Obviously, the instantaneous values of electron temperature T_e, electron density n_e and floating potential V_f can be obtained directly by the triple probe method. The plasma potential V_p can also be estimated simultaneously by [44]

$$V_p = V_f + \frac{1}{2}\left[\ln\left(\frac{1}{2\pi}\frac{m_i}{m_e}\right) + 1\right] T_e \approx V_f + 3.3 T_e. \tag{5.13}$$

The triple probe diagnostic just needs a large enough DC biasing circuit instead of the complex sweeping biasing system. It would also avoid systematic errors caused by the circuit sensitivity to potential fluctuations. With the advantage of good time resolution, the triple probe is widely used for fluctuation measurements. In the following GAM study, triple probes will be used to find

the electron temperature's influences on the plasma density fluctuation measurements, as well as searching for GAM and investigating the plasma fluctuation properties at the STOR-M edge.

5.2 Design of Triple Probes System for STOR-M

5.2.1 Design Parameters

Typical plasma parameters in the STOR-M edge region are listed in table 5.1:

Parameter Items	**Values**
Average electron density n_e	$0.1 \sim 2 \times 10^{12}$ cm^{-3}
Electron temperature T_e	$5 \sim 30$ eV (from RFEA measurements)

Table 5.1: STOR-M Edge Plasma Parameters in Records.

Accordingly, the expected Debye length λ_{De} can be estimated by:

$$\lambda_{De} = \sqrt{\frac{k_B T_e}{4\pi e^2 n_e}}. \tag{5.14}$$

As a result, the plasma Debye length at the STOR-M edge is below 0.1 mm. Based on the plasma sheath theory, the sheath thickness is a couple of the Debye lengths. In order to reduce impact of the plasma sheath on the measurements, the minimum gap between the probe tips needs to satisfy that $\triangle d \gg \lambda_{De}$. The bias potential V_{bias} should be large enough for the sake of drawing the saturated ion current from the plasma. With the rule described in section 5.1, V_{bias} should be larger than 90 V. Another significant design parameter is the sampling rate. Following the Nyquist-Shannon sampling theorem, the sampling frequency must be greater than twice the maximum frequency of the target signal to avoid aliasing.

The GAM frequency can be estimated by

$$f_{GAM} = \frac{\sqrt{2} c_s}{2\pi R_0} = 4.79\sqrt{\gamma T_e}\ \text{[kHz]}, \tag{5.15}$$

where T_e is in [eV]. In the STOR-M tokamak, the adiabatic index lies between 1 and 5/3. The

expected GAM frequency in STOR-M is supposed to be in the region of 10 kHz$\sim$ 34 kHz accordingly.

The electron and ion plasma frequencies in hydrogen plasma are

$$f_{pe} = \frac{1}{2\pi}\sqrt{\frac{4\pi n_e e^2}{m_e}} = 8.98\sqrt{n_e}\ [\text{kHz}], \tag{5.16}$$

and

$$f_{pi} = \frac{1}{2\pi}\sqrt{\frac{4\pi n_i e^2}{m_i}} = 0.21\sqrt{n_i}\ [\text{kHz}], \tag{5.17}$$

where n_e and n_i are in [cm^{-3}]. Thus, the electron plasma frequency is above 2.8 GHz, and the ion plasma frequency is above 65 MHz. Probe sheath theory indicates that the plasma sheath response frequency $\frac{1}{\tau}$ is between the electron plasma frequency f_{pe} and the ion plasma frequency f_{pi}, $f_{pe} \gg \frac{1}{\tau} \gg f_{pi}$ [45].

The ion gyrofrequency of hydrogen plasma is given by

$$f_{ci} = \frac{1}{2\pi}\frac{eB}{m_i c} = 1.52B\ [\text{kHz}], \tag{5.18}$$

where magnetic field B is in unit of [Gauss]. Usually B is set to 0.75 T=7500 Gauss during the normal operation of STOR-M, and the ion gyrofrequency $f_{ci} \simeq 11.4$ MHz. The plasma fluctuations are gyro-averaged plasma behaviors, so the circuits' cut-off frequencies need to be smaller than the the ion gyrofrequency f_{ci} to smooth out system noise caused by the particles' cyclotron. Consequently, the sampling rate must be higher than 68 kHz but slower than 11 MHz for the fluctuation measurements at the STOR-M edge. The typical MHD instabilities frequency is 20 kHz$\sim$ 40 kHz in STOR-M, which is very close to the GAM frequency. Therefore, in the GAM experiments, the MHD interferences to GAM signals should be considered. Methods of suppressing MHD or lowering the GAM frequency need to be tried respectively.

5.2.2 Mechanical Design

In the STOR-M edge plasma, the electron temperature can reach up to 30 eV (1 eV$\approx$11604 K), which is about 348120 K$\approx 3.5 \times 10^5$ °C. Any material in the world can be easily destroyed

in such high temperature plasma. However, the short-time contact with a limited amount of high temperature electrons can prevent the immediate melting of certain materials. But it still requires the material of the probe electrodes to have high electric conductivity, high temperature-resistivity and low secondary electron emission characteristics. Tungsten has the highest melting point among all metals, at 3683 K, which is a good candidate for the probe electrodes. But it still has the risk of melting in tokamak experiments. As for the electrical insulating housing material of the probe, alumina ceramic stands out because of its good thermal conductivity, high melting point($>$ 2000 °C), and good chemical and corrosion resistance.

The triple probe's head is composed of an alumina ceramic house with 3 tungsten rod tips going through. Figure 5.3 shows the structure of the triple probe head and tip. Each tip has a diameter of 0.089 cm with 3 mm in length outside of the ceramic housing. The minimum distance between two tips exceeds 1.2 mm, which is over ten times the Debye length at edge of the STOR-M plasma. The alumina ceramic housing is fixed by screws into a stainless steel tube. It is attached to a scalable manipulator with the feedthrough, as shown in Figure 5.3(c). The triple probe is installed on Port 7-2. The manipulator allows deep measurements, up to r=10.5 cm.

5.2.3 Electrical System

The schematic of the principle circuit for the triple probe is as shown previously in Figure 5.2. The ion saturation current $I_{is} = I_1$ can be obtained by measuring V_R and R. The voltage difference $V_{Te} = V_2 - V_f$ contributes to the electron temperature measurements, and V_f measurements can be used for plasma potential calculations. As mentioned before, V_{bias} needs to be larger than 90 V. A 120 V AC isolation transformer and a rectifier are used to get 180 V DC power supply for V_{bias}, and Figure 5.4 is the circuit diagram.

The ion saturation current measurements can be achieved by measuring the voltage drop V_R across the resistor R in Figure 5.2, and $I_{is} = \frac{V_R}{R}$. With the dimensions of the probe tips as stated in section 5.2.2, the current collecting area A_s is about 0.06 cm^2. In a hydrogen plasma, $m_i = m_p = 1.67 \times 10^{-27}$ kg and $q = e = 1.6 \times 10^{-19}$ C, so the expected ion saturation current is in the range from a few mA to 130 mA for STOR-M, calculated from Eq. 5.12. In order to prevent burning out the sampling resistors, 0.5 Ω sampling resistance is used for the measurements,

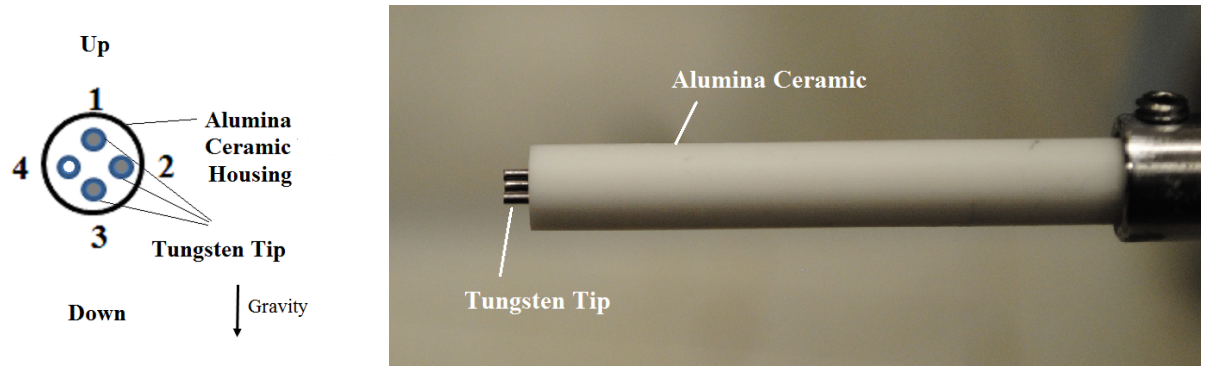

(a) Schematic of Triple Probe Tip.

(b) Picture of Triple Probe Head.

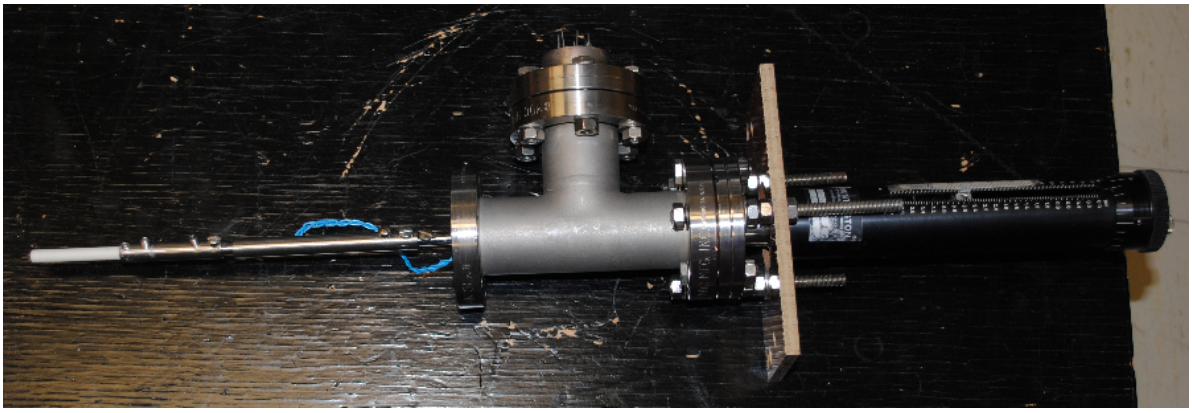

(c) Triple Probe with Feedthrough and Manipulator.

Figure 5.3: The triple probe in STOR-M.

achieved by two 1 Ω (3 W) resistors in parallel. The measurement circuit for V_R may generate current to interfere I_{is} signals. To avoid such interference, it requires the measurements of V_R are electrically isolated. However, the data acquisition (DAQ) system must be grounded at the end stage, so an isolation amplifier is employed (Figure 5.5) using a specially designed optocoupler.

V_f and V_2 are measured with regard to the ground. In order to limit the measurement circuits' interferences with the biasing circuit, a large load voltage divider needs to be used. The expected voltages are up to 200 V, so a 2.2 MΩ resistor and a 10 kΩ resistor make up the pre-voltage-divider. However, a long coaxial cable is needed to send the output signal to the DAQ system. This means the divided signal cannot be sent to the DAQ system directly because of the impedance mismatching. An LM6181 current feedback amplifier is applied to construct a cable driver circuit, which can drive a long 50 Ω cable without adding any extra load to the original circuit. Figure 5.6 shows the complete voltage divider circuit. The actual total divider ratio is 112.5:1.

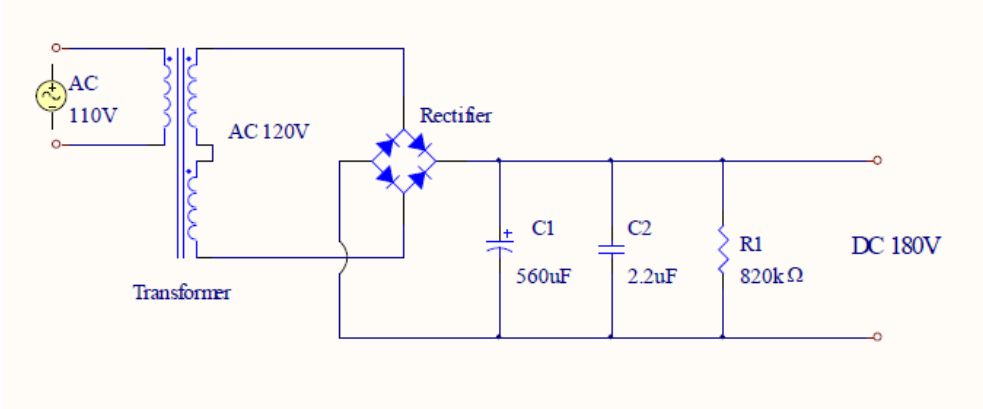

Figure 5.4: DC power supply for triple probe biasing.

There are three sets of DAQ systems for STOR-M operations with different sampling rates. As described previously, the sampling rate f_s for the edge plasma fluctuation measurements should satisfy 68 kHz$<$ f_s $<$65 MHz in STOR-M. Therefore, a high sampling rate DAQ system - NIPXI-1033 by National Instruments - is used. The sampling rate is set to 1 MHz for the GAM experiments.

5.3 Design of Probes Ring and Probe Array Systems for GAM Study in STOR-M

With one movable triple probe, we can only detect the plasma parameters radial profiles but not the GAM features in the poloidal direction. Another two sets of Langmuir probe systems are designed particularly for the GAM searching experiments.

5.3.1 Probes Ring System

A probe ring is designed to detect the ion saturation current fluctuations simultaneously on different poloidal positions in the STOR-M tokamak, as shown in Figure 5.7. This probe ring consists of eight identical Langmuir probes to measure ion saturation currents in the poloidal direction at the tokamak edge. The angular separation between two adjacent probes is $45°$, and the probe tips

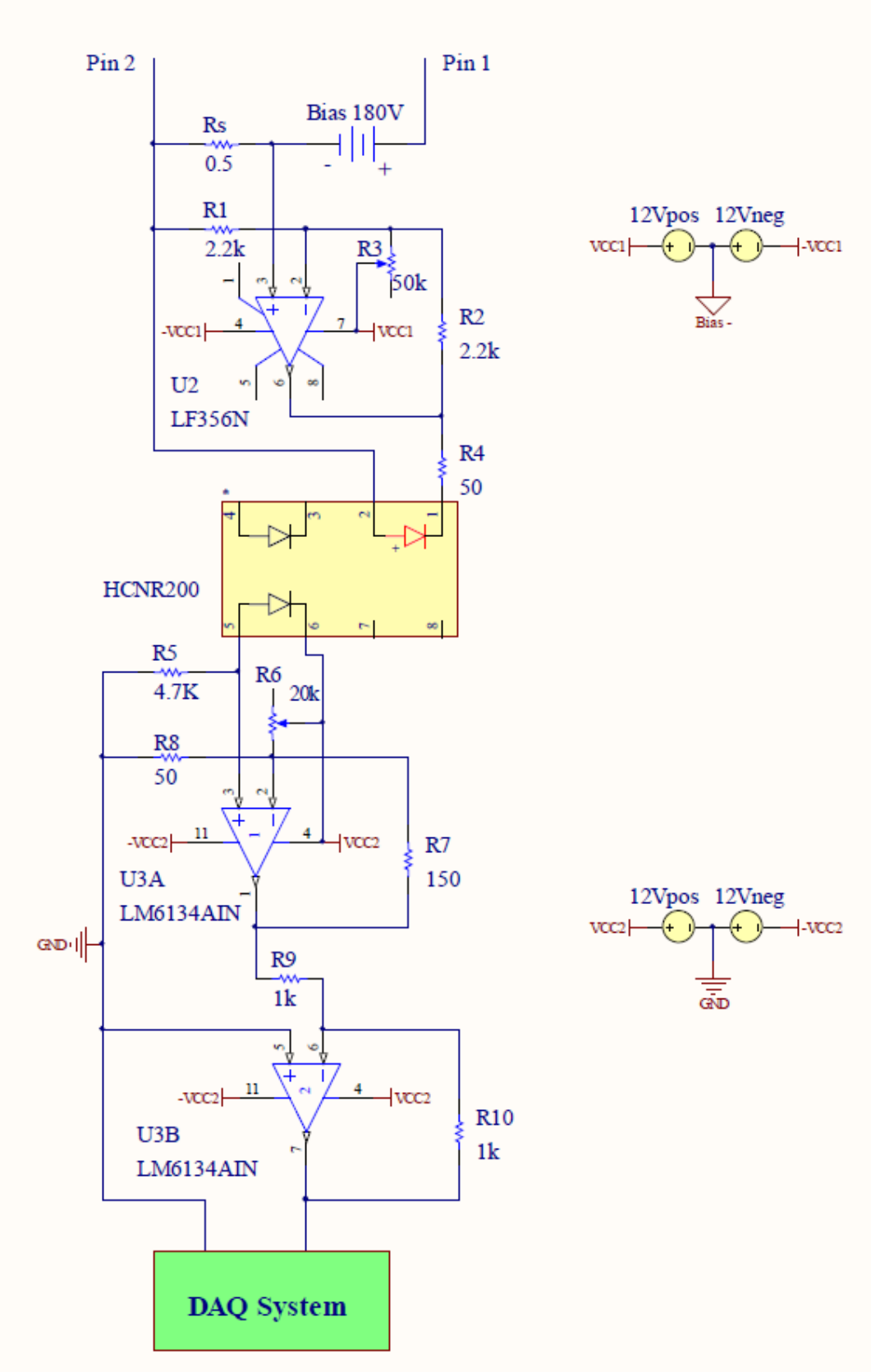

Figure 5.5: Isolation amplifier circuit for ion saturation current measurement in STOR-M.

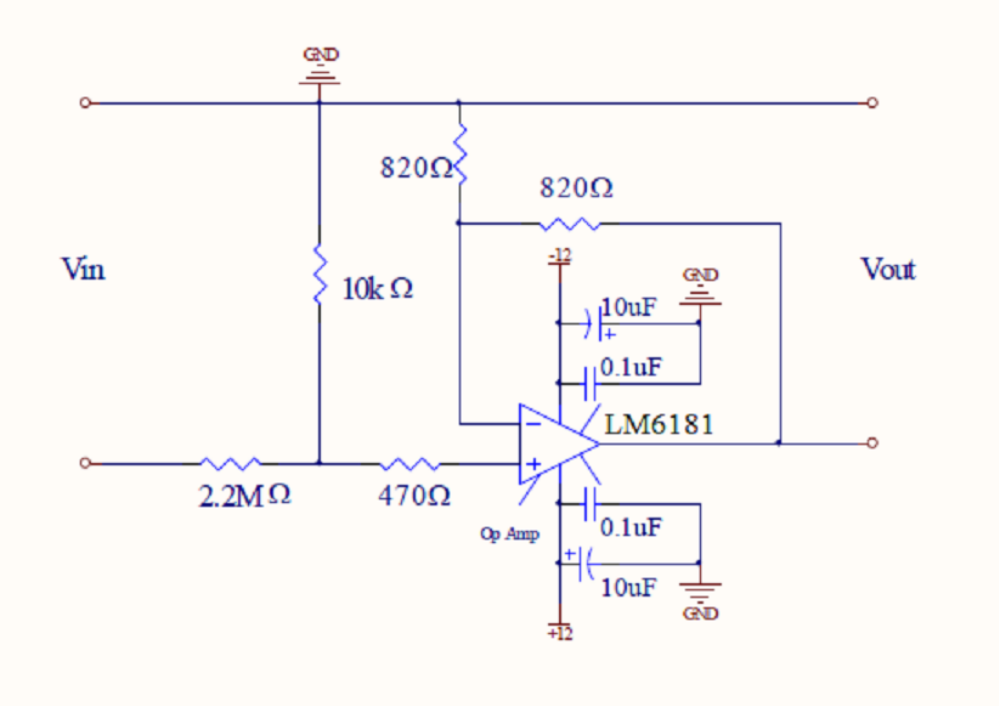

Figure 5.6: Voltage divider with cable driver circuit for probe voltage measurements.

Figure 5.7: Used probes ring for GAM identification experiments in STOR-M.

are positioned at about r=12 cm. Due to the limitation of the port size, the array frame is composed of two half-rings connected together with hinges. The detailed structure is presented in Figure 5.8. A half ring can rotate with respect to the axis to form a circular ring in Figure 5.8(b).

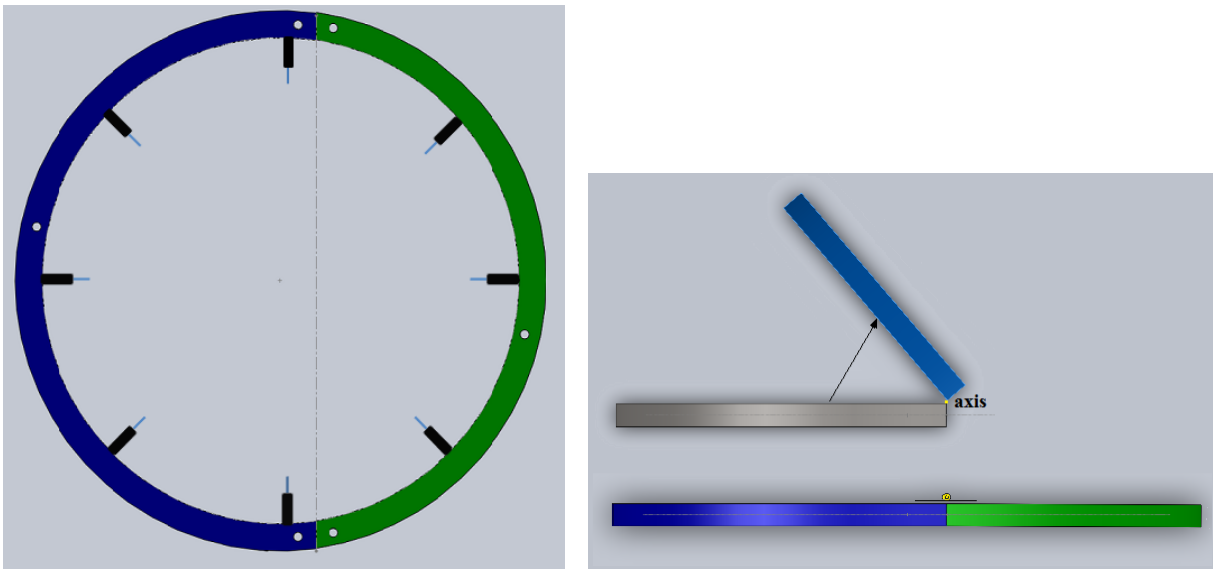

(a) The Front View of the Two Half Rings. (b) The Rotation of the Two Half Rings from the Top View.

Figure 5.8: The ring probe array schematic.

The ring can be folded first to insert into STOR-M through the top vertical Port 11. After being fully located in the vessel chamber, it can be unfolded to compose a complete ring in the chamber. Two supporting stands are mounted on the top vertical Port 11 and the side Port 3 respectively. Then the ring frame can be fixed along the chamber's inner cross-section by being attached to those supports.

Each probe in the ring has two isolated tungsten tips to measure the plasma density fluctuations. Each tip's dimension is 0.08 cm diameter with 3 mm length. One tip of the probe is biased by a large enough DC voltage, and it will draw the ion saturation currents from the edge plasma. The other tip can measure the poloidal profile of the plasma floating potentials. It can also be used as a backup tips during the experiment.

5.3.2 Trident Probe Array System

Besides the probe ring, a trident probe array is designed to have smaller poloidal separations ($\sim 12^{\circ}$) for the edge density fluctuation measurements. The trident probe array consists of a triple probe in the center and two double probes on either side, as shown in Figure 5.9.

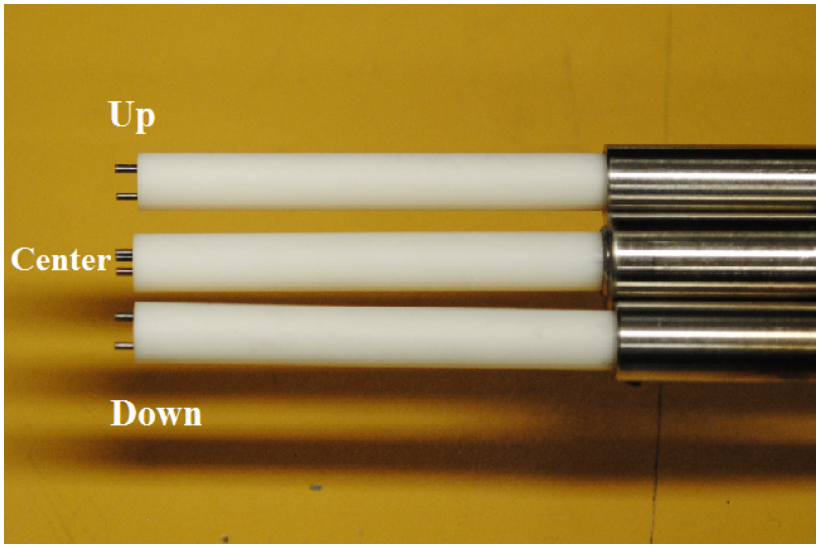

(a) Side View of Trident Probe Array.

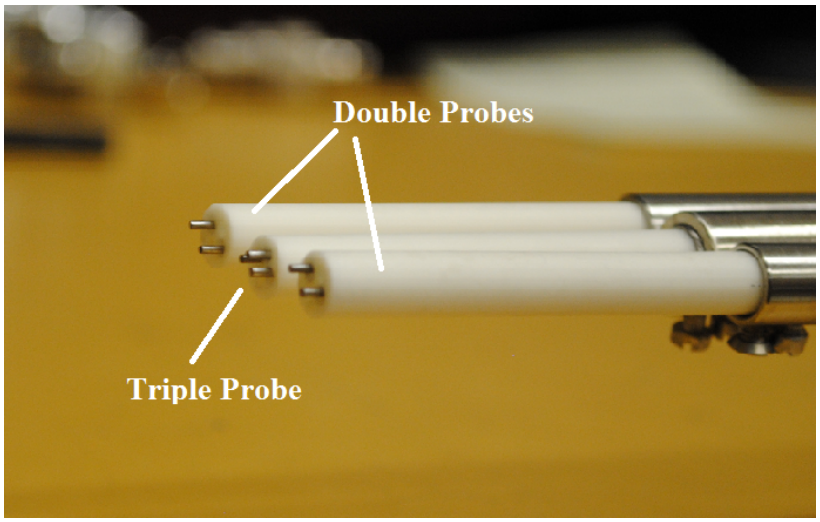

(b) Tip View of Trident Probe Array.

Figure 5.9: Trident probes arrays in STOR-M.

The central triple probe will provide the edge electron temperature as a reference parameter for the other double probes' density measurements. Every probe tip is made of a pure tungsten rod, and has a diameter of 0.089 cm with a length of 2 mm exposed in the plasma. Similar with the

triple probe, the probe array is also mounted on a scalable manipulator. The deepest radial position that it can reach is r=11.75 cm without being damaged by plasma. This probe array is installed on Port 4 with the triple probe on the Port 7-1, separated 90° toroidally. This configuration offers a chance to investigate toroidal edge plasma fluctuation properties.

CHAPTER 6

EXPERIMENTS RESULTS AND ANALYSIS

A series of experiments was conducted to search for the resistive GAM in the STOR-M tokamak. The experiments are performed in the ohmic L-mode and the resonant magnetic perturbation (RMP) environments. The triple probe, the probe ring and the trident probe array are installed to monitor the plasma density fluctuations at the STOR-M edge. The preliminary results are presented and discussed in this chapter.

6.1 Normal Ohmic Heating Discharges Experiment

In STOR-M, hydrogen plasma is initiated by a radio-frequency (RF) microwave (4 MHz, 10 kW). This pre-ionization stage improves the shot-to-shot reproductivity and saves magnetic flux in the iron core transformer. Afterwards, the ohmic heating discharge system drives a toroidal plasma current in the seed plasma. The plasma ionization rate increases with increasing plasma temperature during the initial current ramping up phase (10 ms). Then a constant plasma current is maintained resulting in a low loop voltage of $V_L \leq 3$ V. The ohmic heating discharge system in STOR-M consists of the iron core transformer (eight-turn primary winding) and three capacitor banks (including a 20 mF bias bank, a 200mF fast bank for the current ramp-up and a 10F slow bank for maintaining the plasma current) to produce the primary current waveforms. The capacitor bank voltage values are set according to the experiment requirements. In the GAM experiments, the usual voltage settings are listed below:

(1) The bias bank: 100 V;

(2) The fast bank: 165 V$\sim$175 V (450 V maximum);

(3) The slow bank: 60 V$\sim$70 V (100 V maximum).

6.1.1 Plasma Conditioning

The tokamak chamber needs to be exposed to the atmosphere when the probes are installed. Residual carbon and oxygen remain on the chamber's stainless steel surface during this time and become the dominant impurities in the STOR-M tokamak. Those near surface impurities can degrade the vacuum and react with the hydrogen atoms chemically to form water, carbon oxides and hydrocarbons, which are then dissociated and ionized by the plasma affecting the plasma confinement. Thus, it is important to perform plasma discharge cleaning of the tokamak chamber surface once the chamber has been opened.

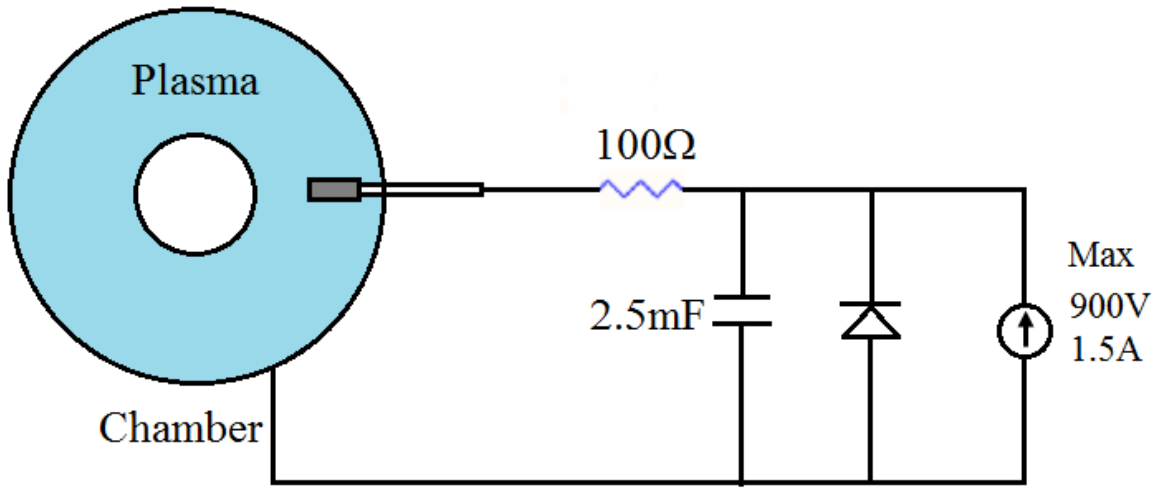

Figure 6.1: Schematic of glow discharge circuit in STOR-M.

However, the normal ohmic discharges are inefficient for the chamber cleaning, which usually requires several hundreds of conditioning discharges. Another more efficient chamber cleaning method, the DC glow discharge cleaning (GDC), can speed up the tokamak chamber cleaning. A stainless steel anode is inserted into the chamber, and the chamber wall is the cathode, as shown in Figure 6.1. An adjustable power supply (up to 900 V, 1.5 A) with a 2.5 mF capacitor bank is used to initiate the gas breakdown. In STOR-M, GDC is started at a gas pressure of around 8×10^{-2}Torr. The glow discharge needs to be maintained for half an hour with a stable 400 mA discharge current and a stable gas pressure of 1×10^{-2} Torr in the chamber. After the glow discharge cleaning, the

remaining gas needs to be pumped out of the chamber until the vacuum reaches 1×10^{-7} Torr. Then new pure hydrogen gas needs to be refilled into the STOR-M tokamak chamber to 1.2×10^{-4} Torr for the additional normal ohmic discharge conditioning. After that, only about a hundred plasma conditioning discharges are needed before the experiments can start.

6.1.2 Low Confinement Mode (L-mode)

During a considerable number of plasma conditioning discharges, the plasma position control feedback system needs to be adjusted to keep the plasma in the chamber center. When the impurities on the wall are cleared out, the loop voltage will drop significantly to about 3 V, and then the plasma is ready for the experiments.

An ohmic discharge without intentional manipulation can only generate a low confinement mode (L-mode) plasma. Figure 6.2 shows typical waveforms of plasma parameters during a good L-mode ohmic discharge in the STOR-M tokamak. In this discharge, $B_T \simeq$0.6 T. The plasma current excesses 20 kA, and the loop voltage is about 3 V during the current flat-top period (10$\sim$30 ms). High plasma current and low loop voltage indicate a low resistivity, thus a high average electron temperature in the plasma column. The quality of plasma is highly sensitive to the gas pressure in chamber during the discharge:

(1) Lower pressure can induce easier break-down, but also produce massive run-away electrons, which can damage the chamber wall and internal probes. Those run-away electrons will increase the unwanted hard x-ray emission level.

(2) Higher pressure can reduce the run-away electrons but degrade the plasma confinement. The plasma will become unstable, resulting in a shorter discharge time.

Therefore, it is important to keep a constant gas pressure for the series of discharges. During the L-mode experiments, hydrogen gas is fed into the STOR-M tokamak chamber constantly to keep the gas pressure at about 1.2×10^{-4}Torr, and gas puffing maintains the plasma density.

6.1.3 Triple Probe Measurements

The triple probe is used to measure the electron density (n_e), the electron temperature (T_e), the floating potential (V_f) and the plasma space potential (V_p) of the plasma in STOR-M. Figure 6.3

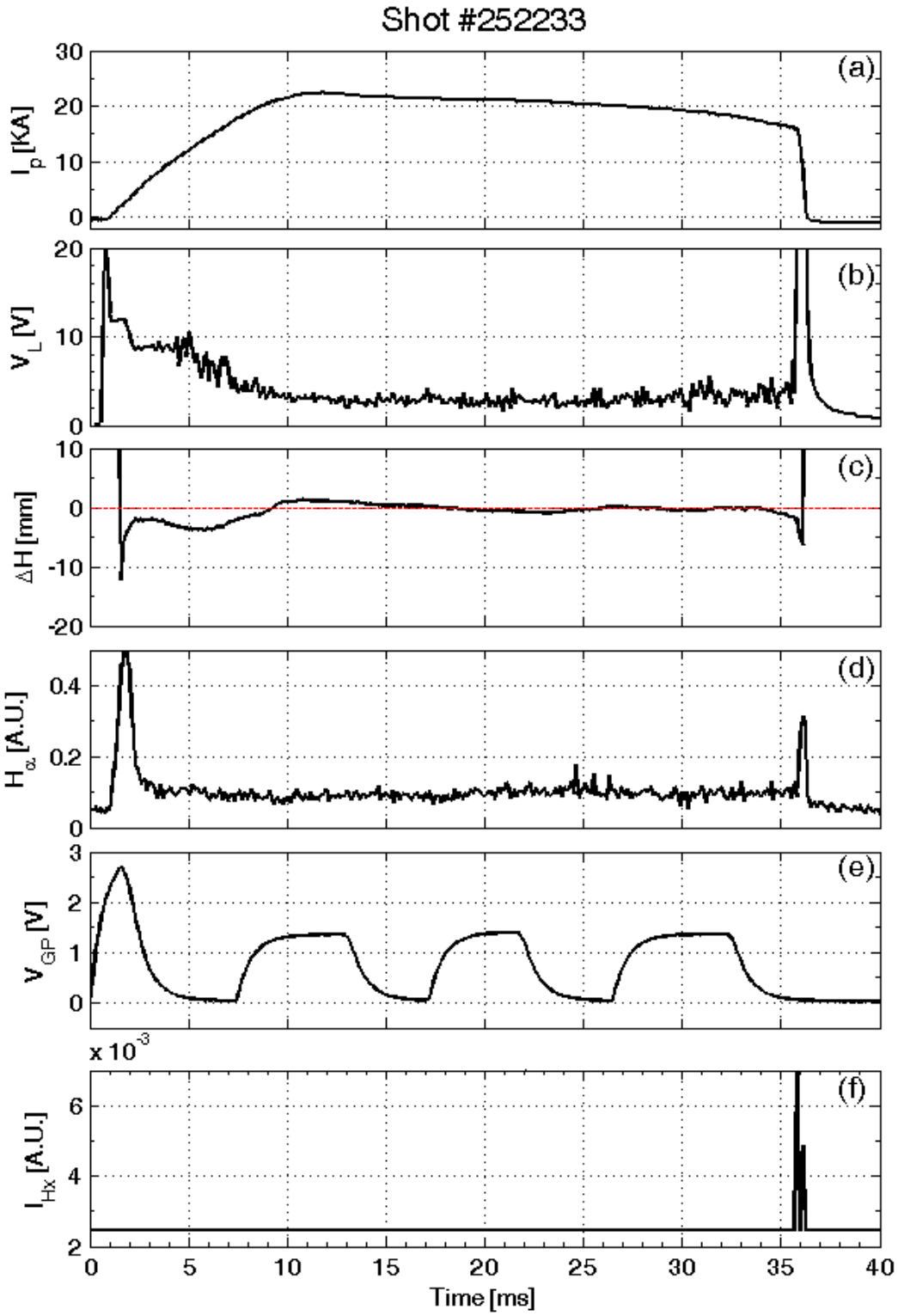

Figure 6.2: Typical waveforms of an ohmic discharge in STOR-M. (a) Plasma current. (b) Loop voltage. (c) Horizontal position. (d) H_α radiation. (e) Sequence of the gas puffing voltage signals. (f) Hard X-ray emission.

shows an averaged waveforms of n_e, T_e, V_f and V_p from the triple probe measurement of the same shot as Figure 6.2. The averaging time window is 1ms. In this shot, the plasma parameters at the tokamak edge are stable during the current flat-top period (10$\sim$30 ms). The ion saturation current is about 0.04 A with about 20eV local electron temperature. The local floating potential V_f and the plasma space potential V_p are around 20 V and 70 V, respectively. These results match the historical edge plasma parameters in reference [5]. The electron density of the edge plasma can be evaluated based on Eq. 6.1,

$$n_e = e^{1/2} \frac{I_{is}}{qA_s} \sqrt{\frac{m_i}{k_B T_e}}, \tag{6.1}$$

where the charge number $q = 1$ (hydrogen case) in STOR-M. The calculation result indicates the edge plasma density is about 0.9×10^{12}cm^{-3} in this shot position.

Changing the triple probe's radial positions shot-by-shot, the radial profiles of four major plasma parameters (n_e,T_e,V_f and V_p) at the STOR-M edge(r=11.75 cm$\sim$13 cm) and SOL region (r=13 cm$\sim$15 cm) are shown as Figure 6.4 under the L-mode discharge condition. The average is taken over the flat-top period of the discharges (10-20 ms). Obviously, the plasma parameters are consistent with the historically records. The plasma tends to have lower density and temperature in more outside area, and it is relatively stable within the 1cm area inside the limiter (r=12 cm$\sim$13 cm).

The Fourier analysis is used to obtain the spectra of the edge plasma parameters' fluctuations, as shown in Figure 6.5. It is clear that the auto-power spectrum of the ion saturation current fluctuation ($\widetilde{I}_{is}/I_{is}$) has similar characteristics to the density fluctuation ($\widetilde{n}_e/n_e$) spectrum in the frequency region for the GAM research, $f \simeq 10 \sim 50$ kHz. In other words, the temperature fluctuation ($\widetilde{T}_e/T_e$) does not affect the $\widetilde{n}_e/n_e$ spectrum properties in this region. Therefore, the auto-power spectrum of $\widetilde{I}_{is}/I_{is}$ can be used to represent the spectral features of $\widetilde{n}_e/n_e$. It is only necessary to measure the ion saturation current fluctuation $\widetilde{I}_{is}/I_{is}$, rather than both the temperature fluctuation $\widetilde{T}_e/T_e$ and ion saturation current fluctuation $\widetilde{I}_{is}/I_{is}$, for the following GAM experiments. The probe ring and the trident probe array systems use this assumption to reduce the probe tip number, and thereby simply the design and mitigate the multiple tips' interferences to the signals.

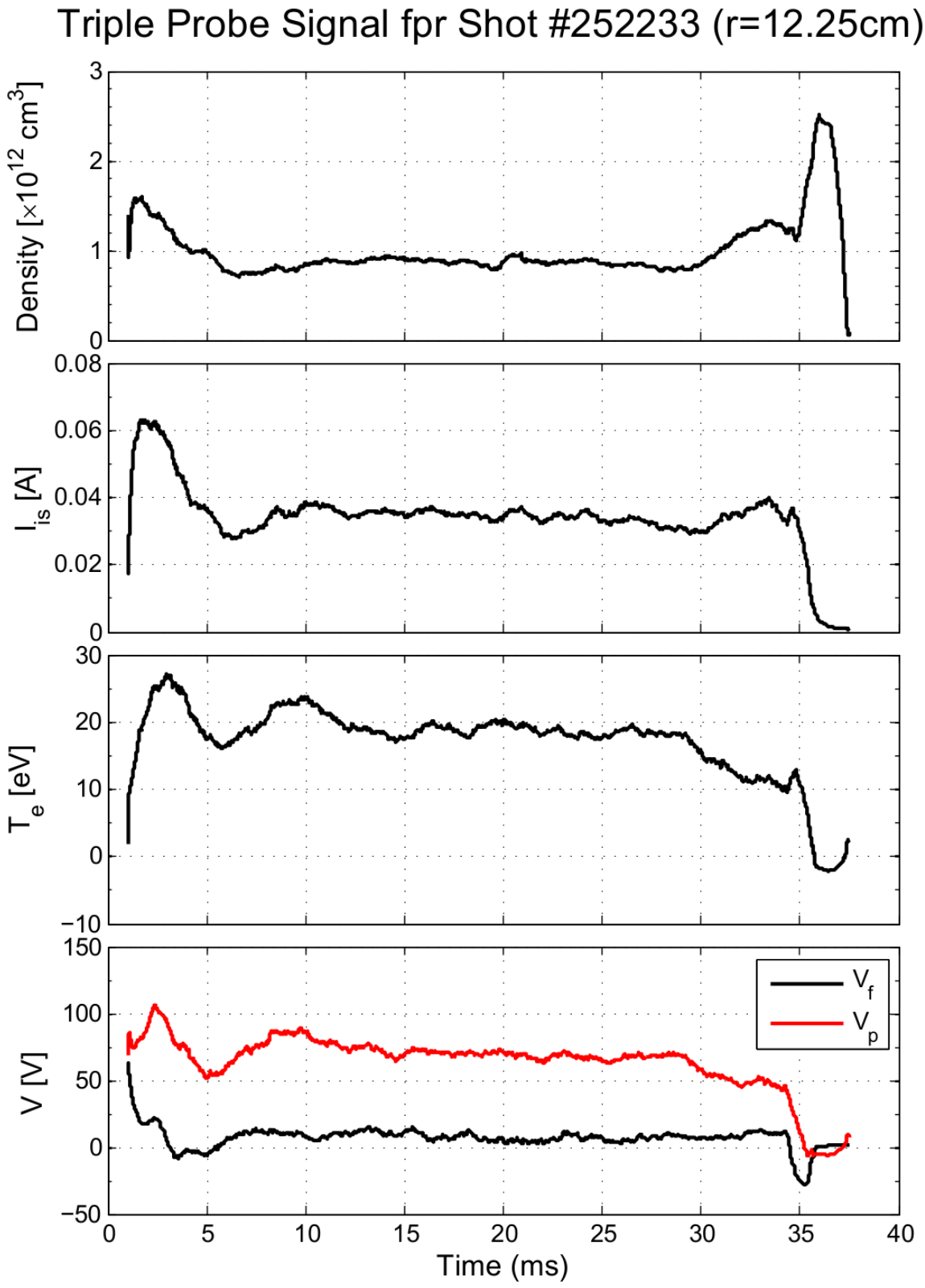

Figure 6.3: A typical triple probe evolution signals in the STOR-M L-mode discharge.

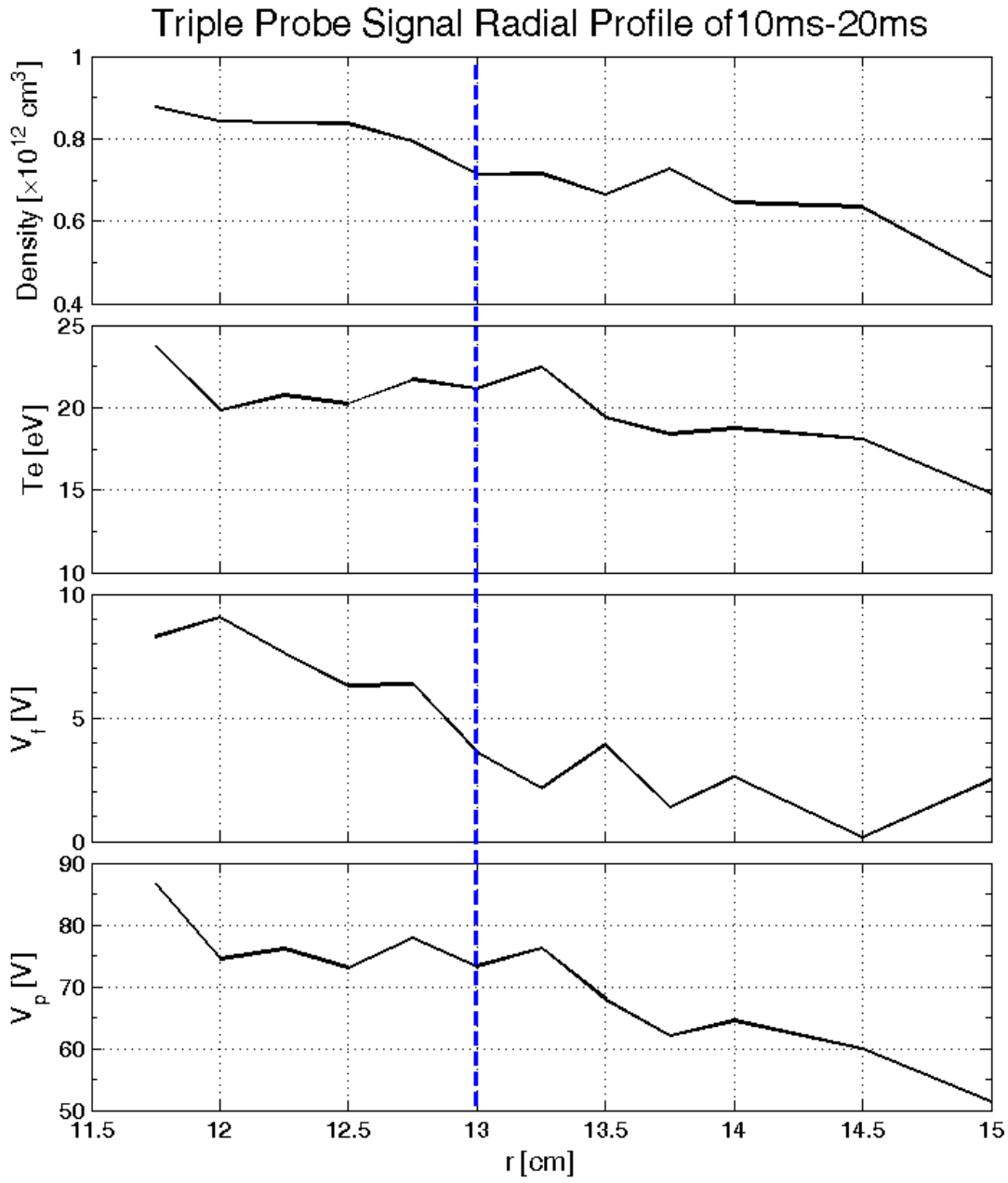

Figure 6.4: Radial profile diagram of plasma parameters in the STOR-M edge region. The blue line indicates the limiter position.

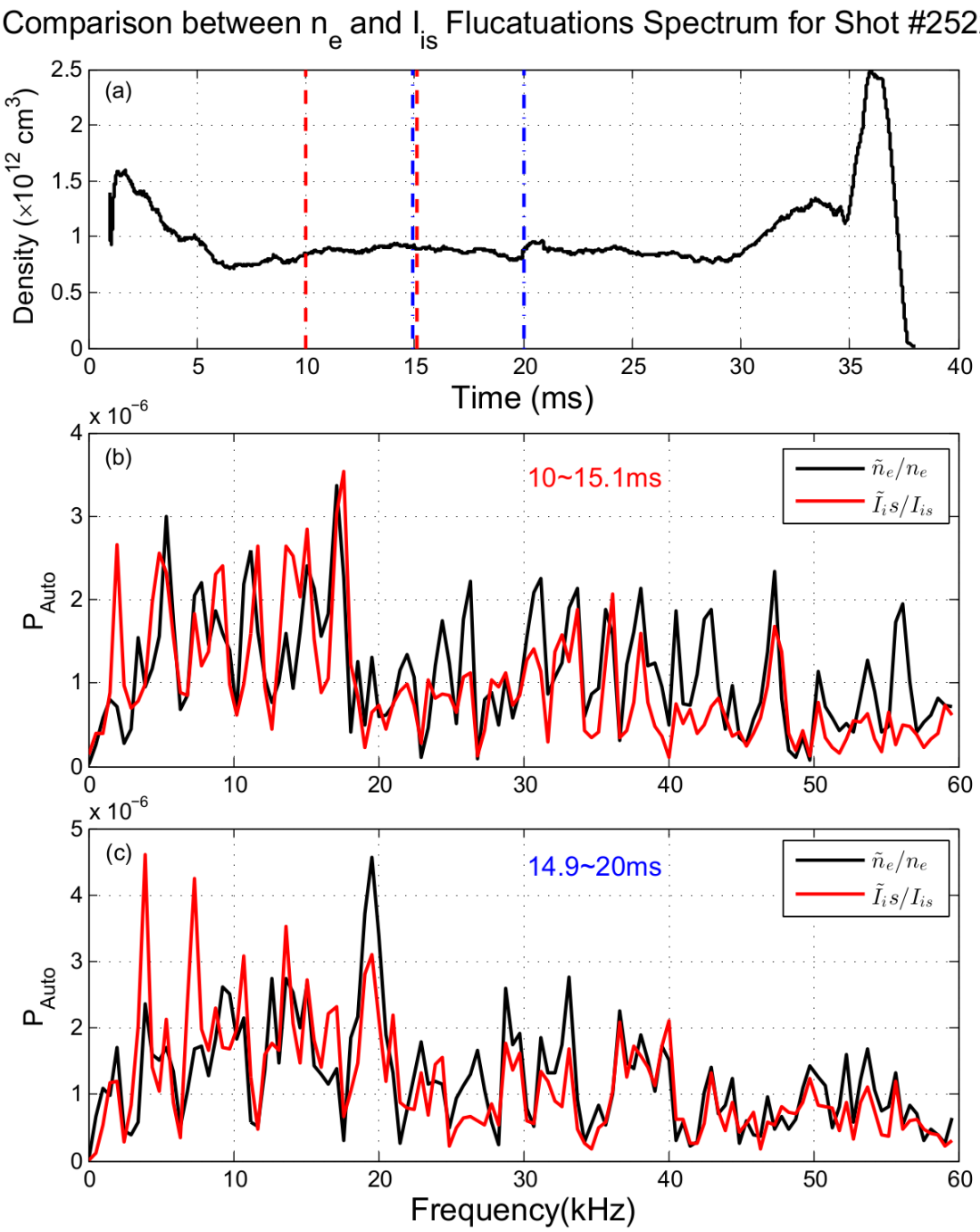

Figure 6.5: $\widetilde{I}_{is}/I_{is}$ and $\widetilde{n}_e/n_e$ auto-power spectra from the triple probe signal in STOR-M(r=12.25 cm). The dashed red lines and blue lines in (a) indicate the analyzed two time segments of the auto-power spectrum (b) and (c).

6.1.4 Ring Probe Array Measurements

Since GAMs were reported to be observed usually in the L-mode plasma, the GAM search experiments are carried out in L-mode operation of STOR-M. According to the analysis of the triple probe signals mentioned earlier, the density fluctuation spectrum properties are not subject to the temperature fluctuation effects in the interested frequency range, which means that the ion saturation current fluctuation spectrum features can represent the density fluctuation features for the GAM research.

However, the first recorded signals from the probes on the ring array already show abnormal behaviour. It turns out, that 5 probes were burned out during the conditioning stage. Figure 6.6 shows the damaged probes with their locations in the ring. Luckily, the top and bottom probes (probe 1 and 5) are unaffected, where the GAM oscillation amplitude is expected to have its maximum. So the GAM search experiments can still be performed.

After analyzing over 50 L-mode discharges, several shots are found to have GAM-like features in the ion saturation current fluctuations frequency spectrum. Figure 6.7 shows a typical GAM-like peak in the frequency spectrum. The analysis time window is from 10 ms to 13 ms of the discharge time. The auto-power spectrum of the magnetic fluctuation signals from 4 Mirnov coils evenly distributed in the poloidal direction indicates that the major MHD instabilities peak at about 29 kHz$\sim$47 kHz, while the auto-power and cross-power spectrum between the probes 1 and 5 of the ion saturation current fluctuations indicate a peak at about f =20 kHz.

The same feature is found with the wavelet analysis method within the same time window, as shown in Figure 6.8. It is clear that the ion saturation current (indicating density) fluctuations from the top and bottom probes have a common characteristic oscillation of f =21 kHz at about 11.2 ms time (red spots), while the magnetic fluctuations coincide with the density fluctuations at about 16 kHz, 30 kHz or over 30 kHz, but not at around 20 kHz region. Therefore, the 20 kHz density oscillation likely has nothing to do with the MHD oscillations, and GAM could explain the oscillation. The classical Winsor's GAM frequency ω_{Ge} $\approx$18 kHz when the edge temperature $T_e \approx 20$ eV (r=12 cm), which is lower than the observed frequency in this shot. However, the classical GAM frequency is just a rough approximation. In the STOR-M edge collisional plasma, the ion temperature is higher than the electron temperature. The resistive GAM dispersion relation

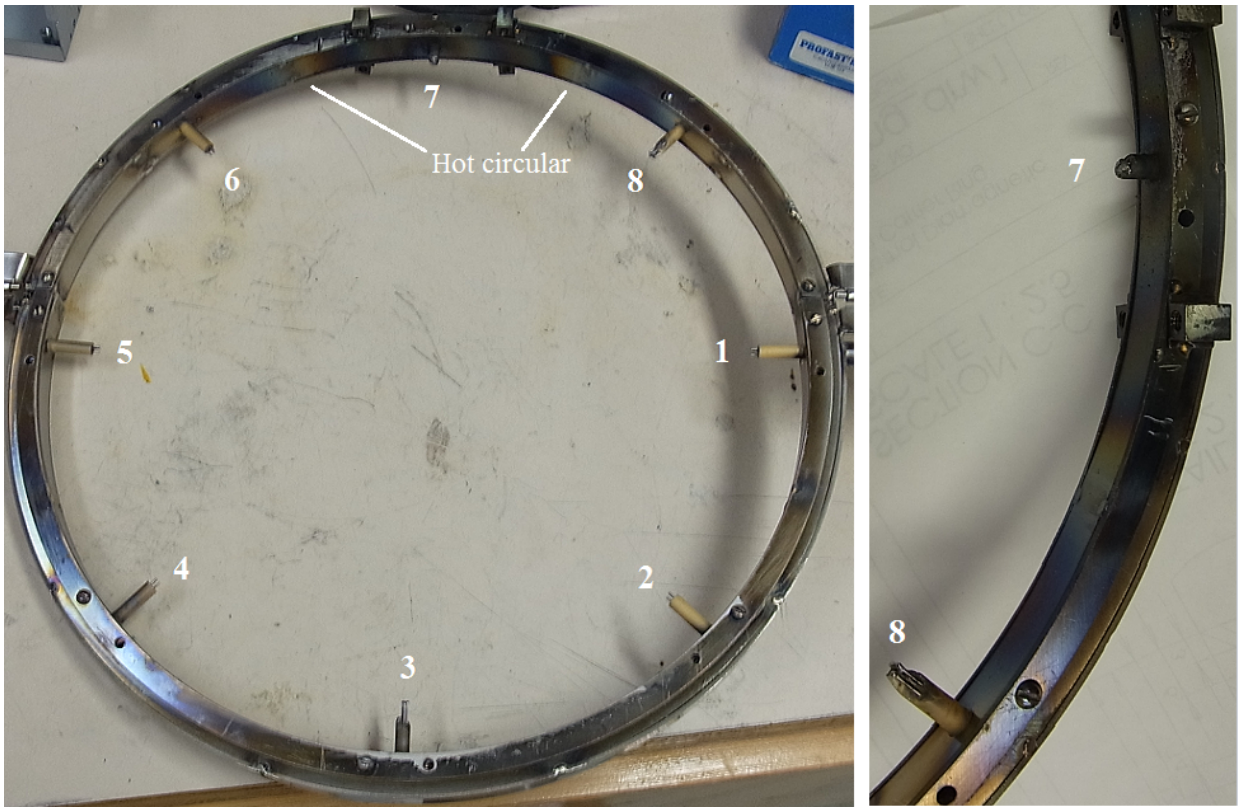

(a) Picture of the uninstalled ring probe array with the burned-out probes.

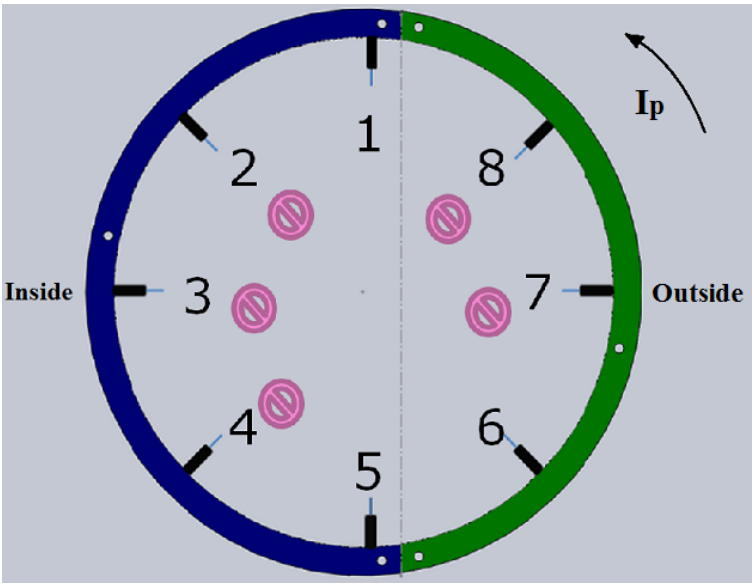

(b) Illustration of the burned-out probe positions on the ring and a closer view of some burned-out probes.

Figure 6.6: Picture of the damaged probes on the ring probe array in STOR-M. Probes 2, 3, 4, 7 and 8 are damaged.

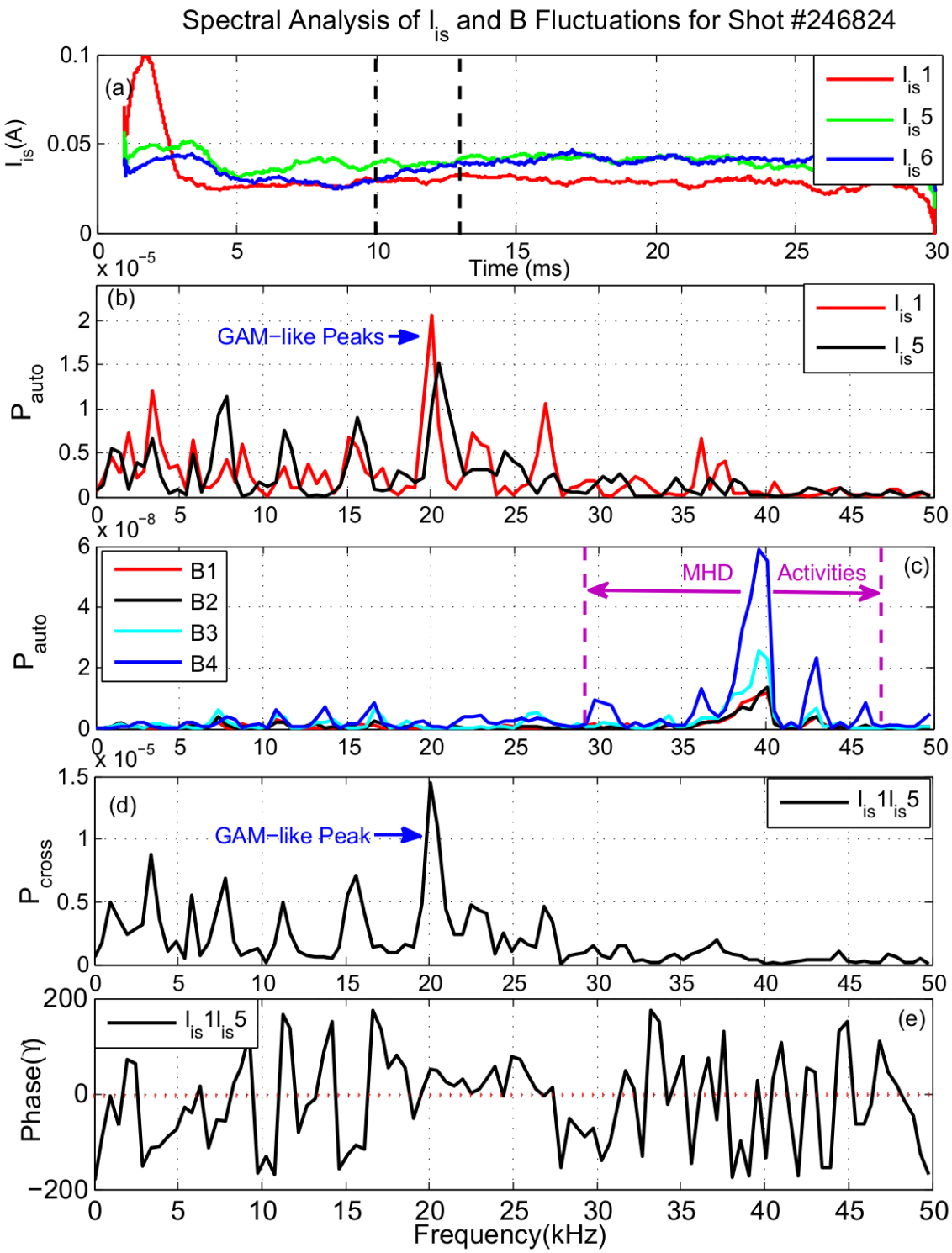

Figure 6.7: GAM-like feature in Fourier spectra from the ring probe array signals during the STOR-M L-mode discharge(r=12 cm). (a) Averaged I_{is} waveforms from probes 1, 5 and 6, and the dashed black lines represent the analyzed time segment for the spectra below. (b) Auto-power spectrum of I_{is} from Probes 1(top) and 5(bottom). (c) Auto-power spectrum of Mirnov coils signals. (d) Cross-power spectrum of I_{is} between probes 1(top) and 5(bottom). (e) Cross-power phase spectrum of I_{is} between probes 1(top) and 5(bottom).

gain in Chapter 3 could provide a more accurate assessment of the GAM frequency at the STOR-M edge.

According to RFEA [2] and triple probe measurements, the ion-electron temperature ratio T_i/T_e is about $1.4 \sim 1.65$ around $r = 12$ cm in STOR-M. The previous triple probe measurements indicate that T_e is about 20 eV and n_e is about 0.8×10^{12} cm^{-3} in the edge region. Accordingly, the $b_s \simeq 0.01 \sim 0.5$, while the electron-ion collision frequency $\nu_e \approx 30$ GHz, and the relative collision rate ω_χ/ω_{De} is 0.0001 to 0.01. The calculation of the characteristic resistive GAM frequency distribution is shown in Figure 6.9. It shows that the damping is low ($Im(\frac{\omega_{GR}}{\omega_{Ge}})$>-0.045), and the relative resistive GAM frequency is about 1.13 to 1.77 times the classical Winsor's GAM frequency, $\frac{\omega_{GR}}{\omega_{Ge}} \simeq 1.13 \sim 1.77$. As a result, the expected resistive GAM frequency is about 20$\sim$31 kHz under similar condition.

The experimental results from the ring probe array measurements suggest that the GAM-like peak is at a frequency of about 20$\sim$21 kHz. This falls within the theoretical resistive GAM frequency range, 20$\sim$31 kHz. Therefore, the experimental result is consistent with the theoretical prediction in STOR-M. However, the phase analysis doesn't reveal that the signals of probes 1 and 5 are anti-phased. So this oscillation may not have $m = 1$ standing wave mode structure. In fact, the phase spectrum (Figure 6.7(e)) indicates a stable phase region around 20 kHz, which implies the particularity of poloidal mode structure for the 20 kHz oscillations. However, due to the lack of the whole poloidal distributed probes measurements, the phase analysis is too rough to give a valid conclusion on the poloidal mode structure in STOR-M.

6.1.5 Trident Probe Array Measurements

Due to the unavailability of the other 5 probes in the probe ring system, the movable trident probe array is used as a back-up plan for the GAM search experiments in STOR-M. However, the limitation of available ports for installing the probe resulted in a equatorial plane position of the chamber cross-section, where the GAM activities in density fluctuations are supposed to be weakest. It is expected to see no GAM features in the center triple probe signal, while the spectrum of the other two side probes signals can have small GAM-like peaks. However, the analysis results doesn't follow this prediction. Figure 6.10 shows a GAM-like peak at about 22 kHz while the local

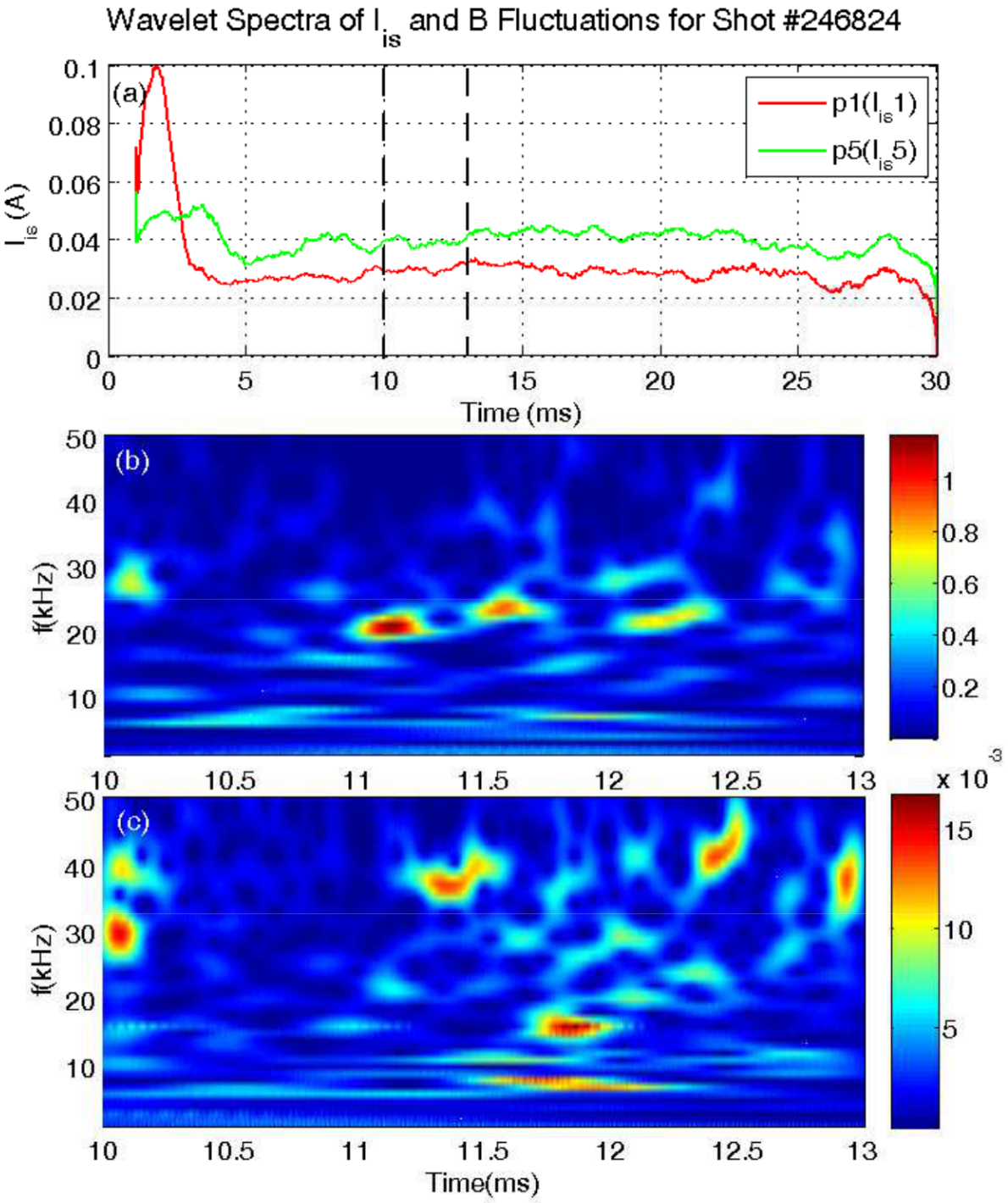

Figure 6.8: GAM-like feature in the wavelet spectra from the ring probe array signals during the STOR-M L-mode discharge. (a) Averaged I_{is} waveforms from probes p1 and p5 (top and bottom), and the dashed black lines represent the analyzed time segment for the spectra below. (b) Wavelet cross-power spectrum of p1 and p5. (c) Wavelet cross-power spectrum of p1 and B1(Mirnov coil signal).

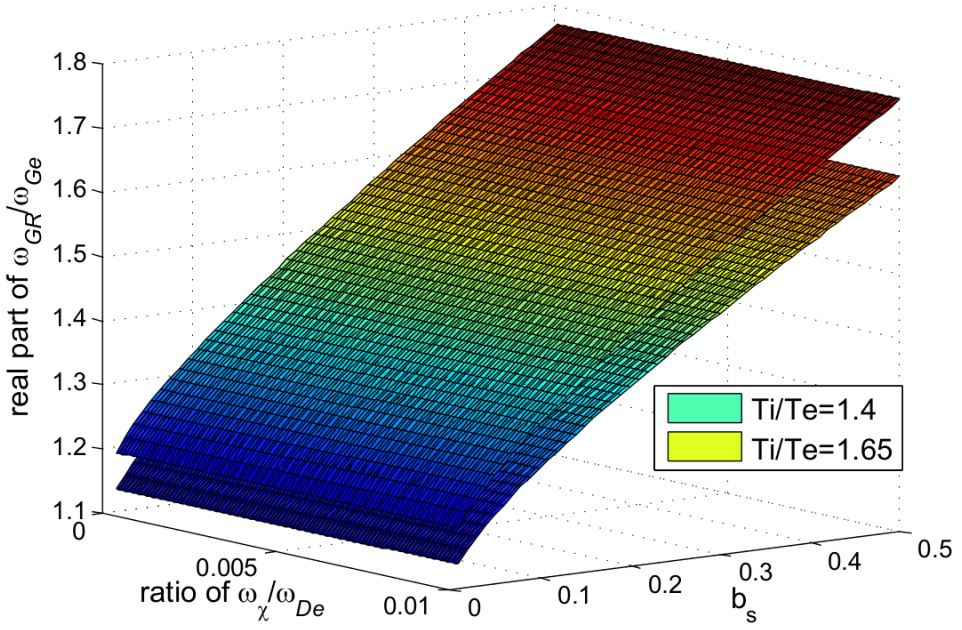

(a) Real solution part of the relative resistive GAM frequency at the STOR-M edge $\frac{\omega_{GR}}{\omega_{Ge}}$.

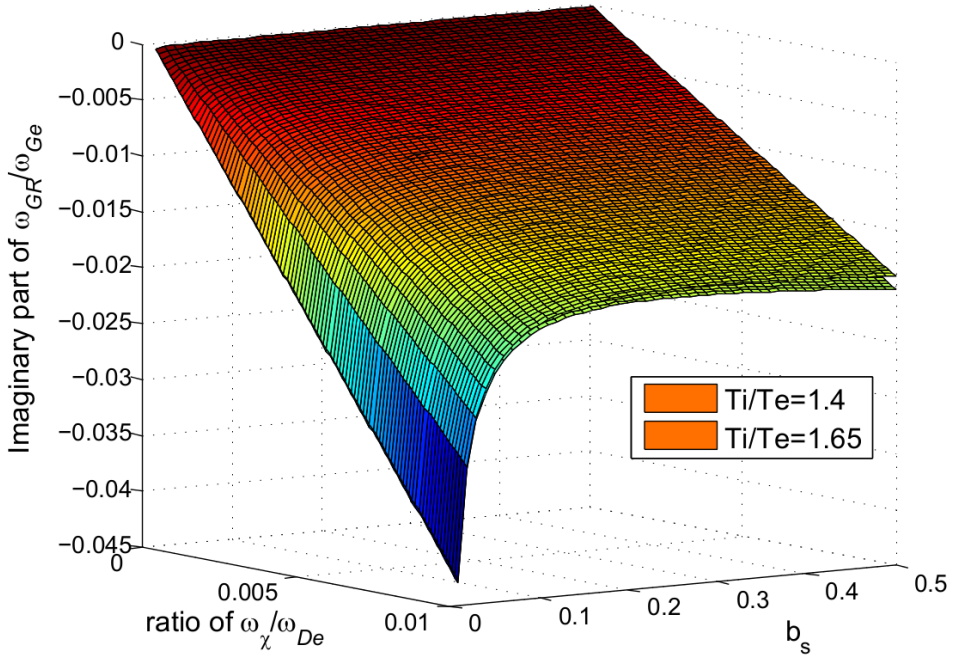

(b) Imaginary solution part of the relative resistive GAM frequency at the STOR-M edge $\frac{\omega_{GR}}{\omega_{Ge}}$.

Figure 6.9: Relative resistive GAM frequency theoretical results at the STOR-M edge. The $\frac{\omega_{GR}}{\omega_{Ge}}$ ratio diagram in terms of b_s and $\frac{\omega_\chi}{\omega_{De}}$.

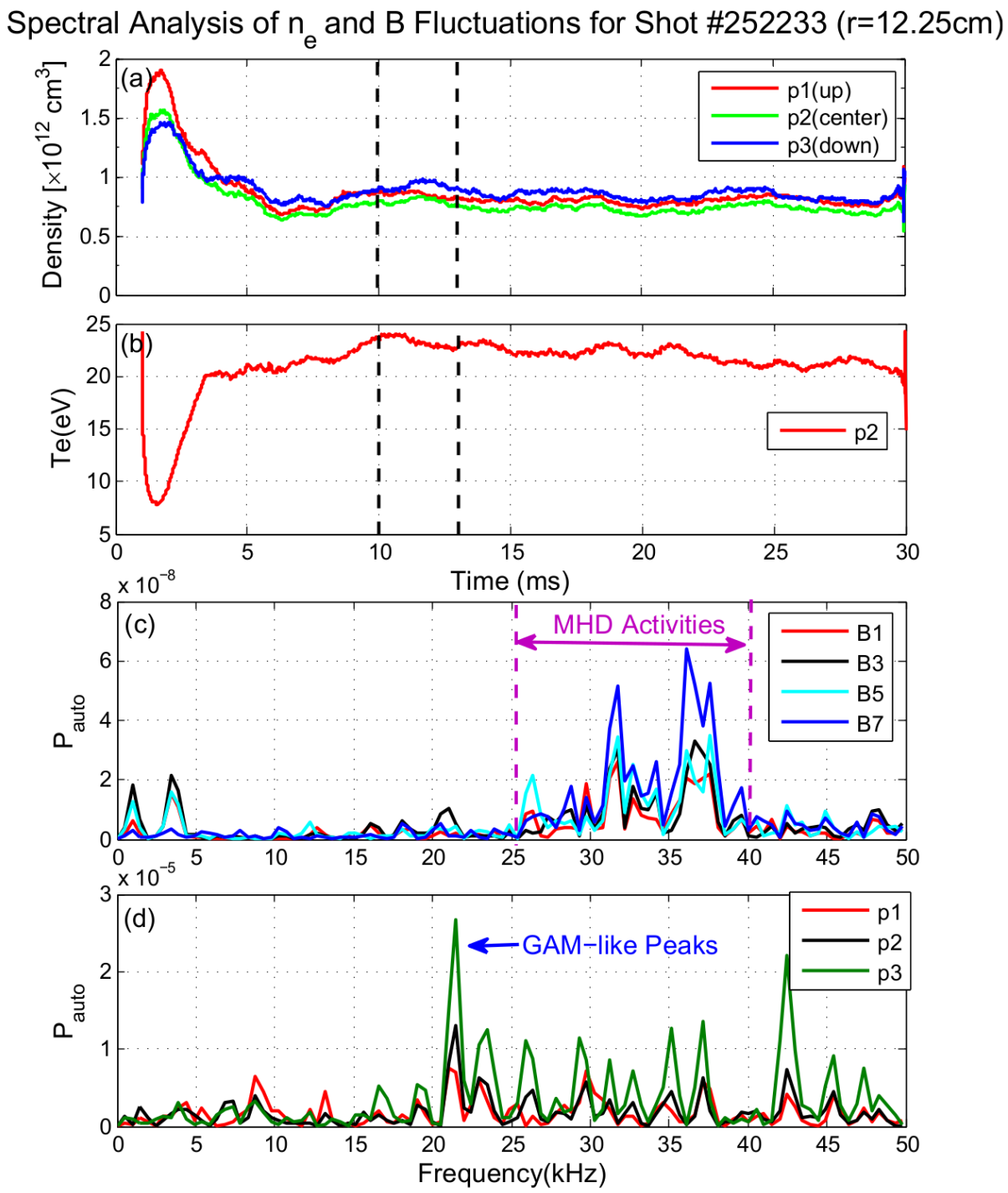

Figure 6.10: GAM-like feature in Fourier spectra from the trident probe array signals during the STOR-M L-mode discharge(r=12.25 cm). (a) Averaged n_e waveforms from probes 1(up), 2(center) and 3(down), and the dashed black lines represent the analyzed time segment for the spectra below. (b) Averaged T_e waveform from the center probe 2. (c) Auto-power spectrum of Mirnov coils' signals. (d) Auto-power spectrum of n_e from the trident probe array's signals.

temperature is about 23 eV and MHD activities focus on 25∼40 kHz. The classical Winsor's GAM frequency is thereby about 19 kHz, and the theoretical resistive GAM frequency should be in the range of 21.5∼34 kHz. Again, the theoretical and experimental results agree with each other.

Gradually changing the trident probes position to r=11.75 cm, 12 cm, 12.5 cm and 12.75 cm gradually (edge plasma), profiles are created with several L-mode discharges at each position. Similar peaks are found in the density auto-power spectrum at the position of r=12 cm and 12.5 cm (different with MHD activities frequency region), but not at the r=11.75 cm and 12.75 cm (more random-like peaks in the target frequency region). Accordingly, it can be concluded that the GAM-like peaks appear at the relative radius $\rho \simeq 0.92 \sim 0.96$ region in STOR-M. The trident probe signals properties don't fit the mode structure predictions. Therefore, the uncertainty of the conclusion is still an unsolved issue for the above GAM search experiments.

6.2 Resonant Magnetic Perturbation (RMP) Experiment

From the analysis above, it is noticed that the MHD signals frequencies are really close to the GAM-like signals frequencies in the STOR-M edge plasma. It degrades the credibility of the previous results. If the MHD can be suppressed successfully, it may provide a better environment for the GAM search experiments. Another series of experiments are conducted accordingly with the resonant magnetic perturbation (RMP) technique, which uses external resonant helical magnetic fields to suppress the major MHD instabilities. Investigating the poloidal profile of density fluctuations in such condition would provide a more clear picture on how the low frequency MHD instabilities effects on the GAM-like phenomena.

In the STOR-M tokamak, the RMP is induced by two sets of helical coils in series, with poloidal and toroidal mode numbers $m = 2, n = 1$. Two capacitor banks - a 50 mF, 450 V fast bank, and a 420 mF, 100 V slow bank - are employed to generate the RMP current pulse. The current can approach 1200 A and 1700 V. Figure 6.11 shows a typical waveforms of an ohmic discharge with 8 ms RMP pulse starting at 20 ms during a discharge in STOR-M. The major effect of RMP field is the suppression of the major MHD instabilities (30∼40 kHz), as measured by Mirnov coils (Figure 6.12).

It is clear that during the RMP pulse (20∼28 ms), the fluctuation amplitude of the magnetic

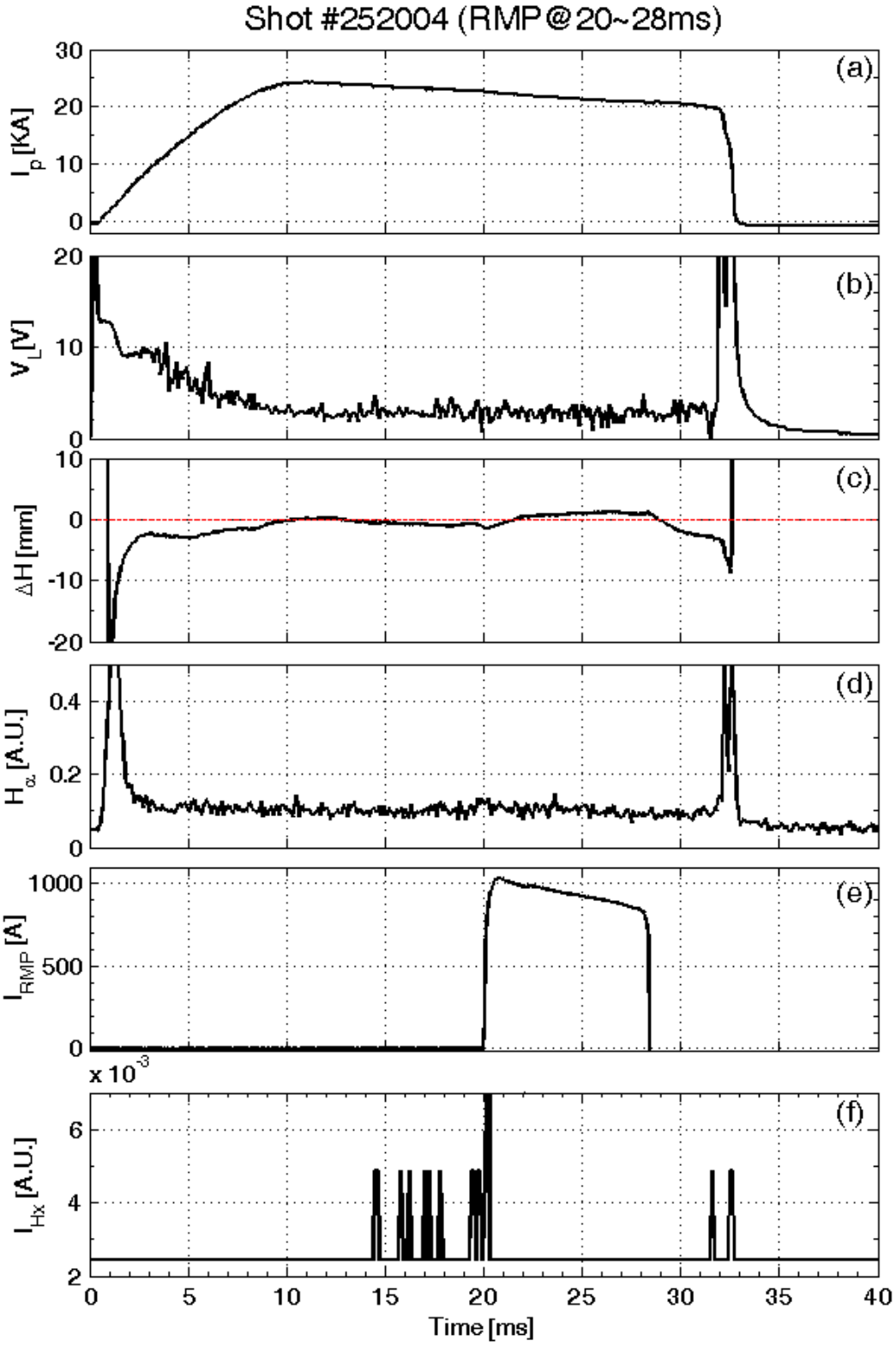

Figure 6.11: The waveforms of an ohmic discharge with RMP (20-28 ms) in STOR-M.(a) Plasma current. (b) Loop voltage. (c) Horizontal position. (d) H_α radiation. (e) RMP pulse. (f) Hard X-ray emission.

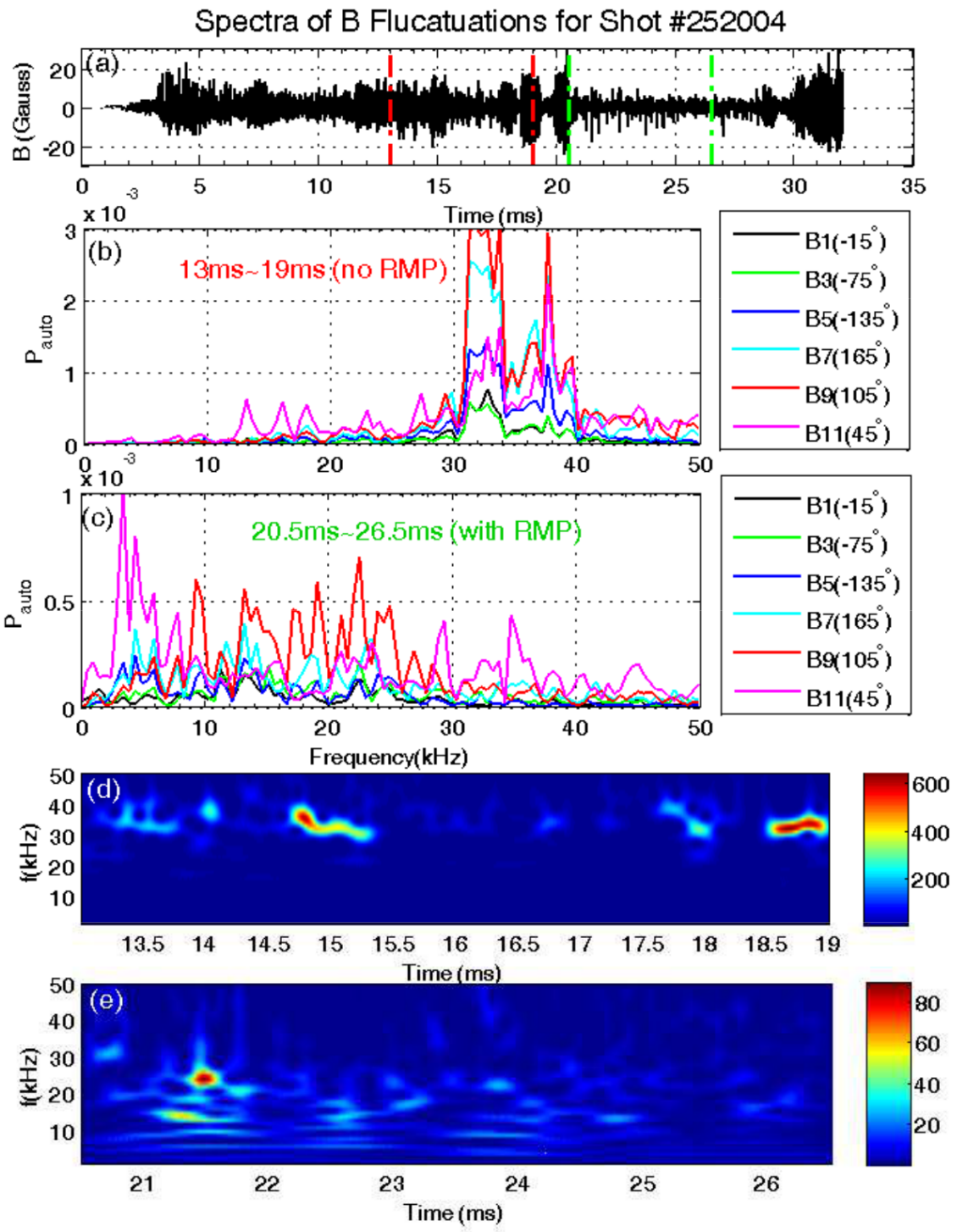

Figure 6.12: Suppression of major MHD fluctuations(30∼40 kHz) due to RMP in STOR-M. (a) Illustration of B fluctuation($\widetilde{B}$) from a Mirnov coil signal: the red lines represent the time segment without RMP, while the green lines represent the time segment with RMP. (b) Auto-power spectrum of $\widetilde{B}$s without RMP. (c) Auto-power spectrum of $\widetilde{B}$s with RMP. (d) Wavelet cross-power spectrum of B5B9 without RMP (13∼19 ms). (e) Wavelet cross-power spectrum of B5B9 with RMP (20.5∼26.5 ms).

field is decreased, and the major MHD activities at about 30∼40 kHz is suppressed. The relative low frequency magnetic fluctuations (<26 kHz) dominate the power spectrum, according to the fast Fourier transform(FFT) auto-power analysis and the wavelet cross-power analysis before (13∼19 ms) and after (20.5∼26.5 ms) RMP triggered. In the wavelet spectrum, a major peak of 25 kHz frequency appears at about 21.5 ms discharge time, as shown in Figure 6.12(e). This is very close to the resistive GAM-like frequencies observed in the previous experiments. Therefore, it is necessary to confirm experimentally that the previous GAM-like peaks are not caused by the low frequency MHD instabilities.

6.2.1 Trident Probe Array Measurements

Since the previous GAM-like frequency was found at about r=12 cm∼12.5 cm by the trident probe array, the trident probe array was positioned at r=12 cm and 12.5 cm to monitor the density fluctuations in the similar ohmic heating discharges with RMP pulse circumstance. The electron density and temperature evolution diagrams as Figure 6.13(a)and(b) (the same shot as in Figure 6.12) suggest that the plasma density and temperature increased slightly by the RMP pulse. Figure 6.13(c)-(f) shows a typical FFT spectrum of the density fluctuations at r=12 cm before and during the RMP pulse in this discharge. The FFT analysis time window is 3 ms with about 0.5 kHz frequency resolution. It can be seen that the density fluctuation amplitude is generally suppressed during the RMP pulse in the 0∼50 kHz frequency range, compared with the case without RMP shown in Figure 6.13(c) and (e). In addition, the lower frequency (<20 kHz) fluctuation is suppressed more severely than the higher frequency components. However, there is no clear clue of resistive GAM-like peaks and MHD activities.

Further cross-power analyses using FFT and wavelet methods are employed to the electron density($\widetilde{n_e}$) and the magnetic fluctuations($\widetilde{B}$) before and during the RMP pulse during the same discharge, as shown in Figure 6.14. The FFT cross-power spectrum of $\widetilde{n_e}$ and $\widetilde{B}$ indicates the suppression of major MHD activities as well (Figure 6.14(a)-(b)). Comparing the wavelet cross-power spectrum of $\widetilde{n_e}$ and $\widetilde{B}$ with the spectrum of $\widetilde{n_e}$ from probe 1(up) and probe 3(down), there are some interesting features have been found in Figure 6.14(c)-(f):

(1) Before the RMP pulse(13-16 ms), there is a peak in the MHD and the density fluctuations

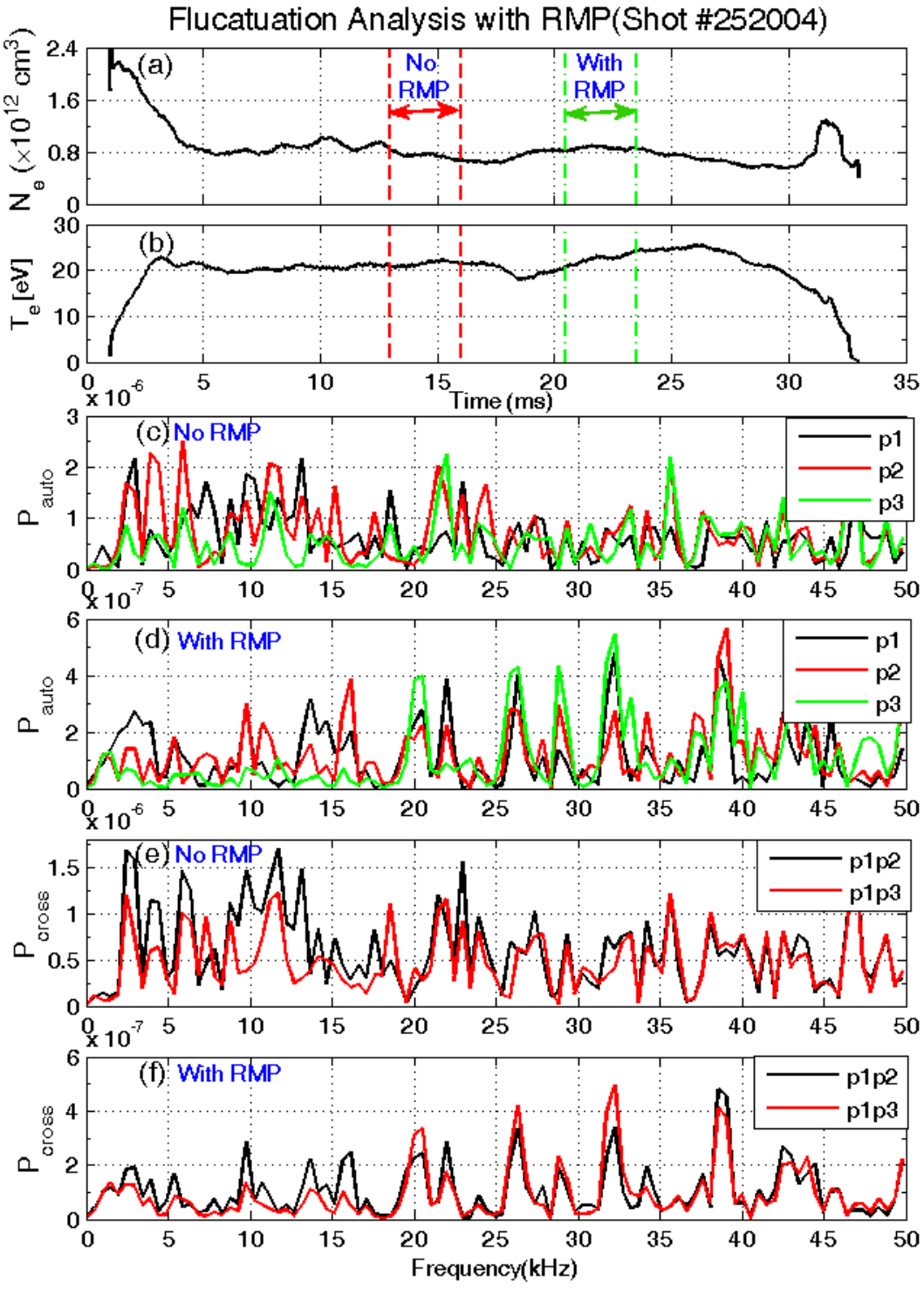

Figure 6.13: n_e fluctuations analysis with RMP discharge in STOR-M(r=12 cm). (a) Averaged n_e waveform from probes 2(center), and the dashed red(green) lines represent the analyzed time segments for the spectra below. (b) Averaged T_e waveform from the center probe 2. (c) Auto-power spectrum of $\widetilde{n_e}$ without RMP (13∼16 ms). (d) Auto-power spectrum of $\widetilde{n_e}$ with RMP (20.5∼23.5 ms). (e) Cross-power spectrum of $\widetilde{n_e}$ without RMP (13∼16 ms). (e) Cross-power spectrum of $\widetilde{n_e}$ with RMP (20.5∼23.5 ms).

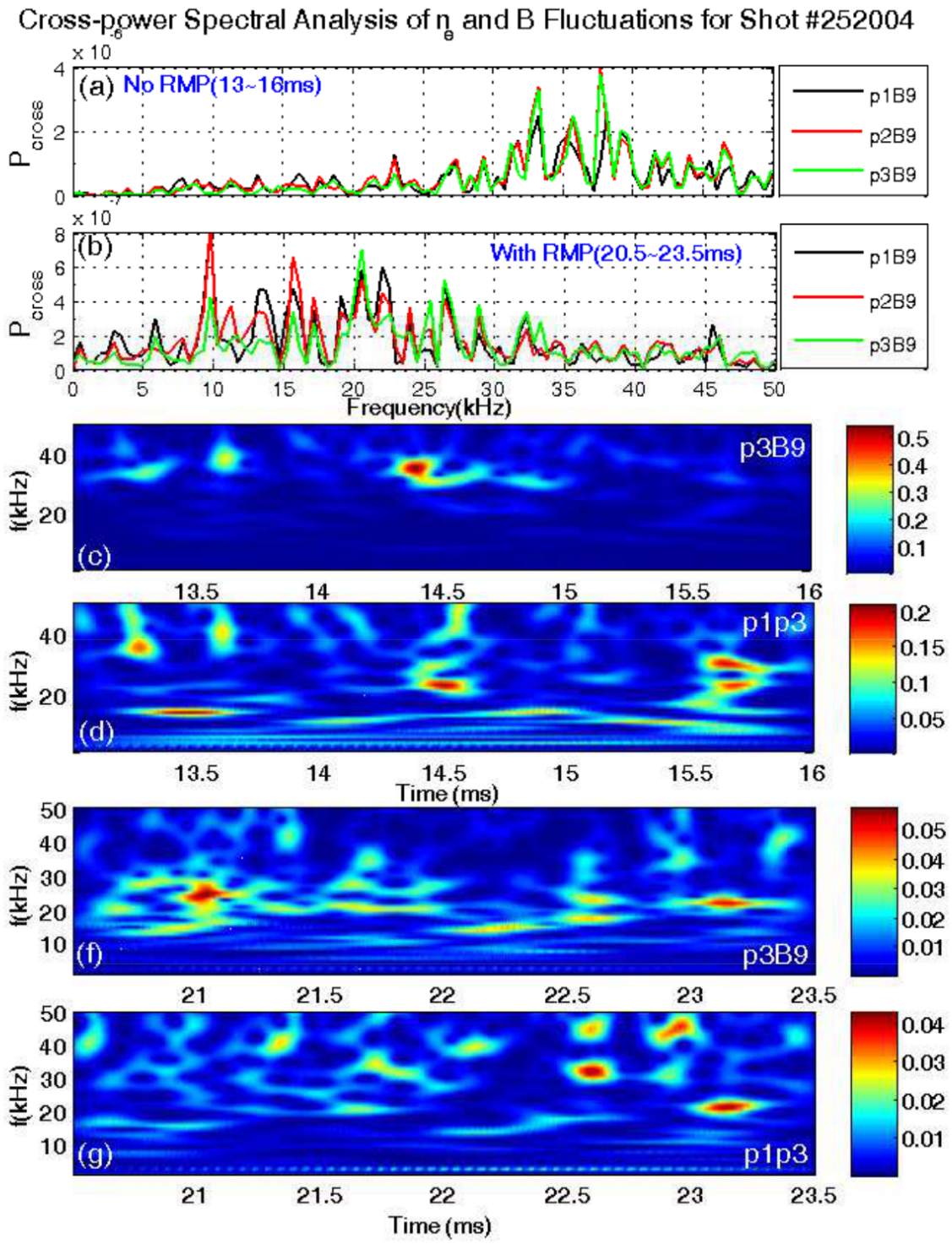

Figure 6.14: Ne and B fluctuations analysis with RMP discharge in STOR-M. (a) Cross-power spectrum of $\widetilde{n_e}$ and $\widetilde{B}$ without RMP (13∼16 ms). (b) Auto-power spectrum of $\widetilde{n_e}$ and $\widetilde{B}$ with RMP (20.5∼23.5 ms). (c) Wavelet cross-power spectrum of $\widetilde{n_e}$ and $\widetilde{B}$ without RMP (13∼16 ms). (d) Wavelet cross-power spectrum of $\widetilde{n_e}$s from probe 1 and 3 without RMP (13∼16 ms). (e) Wavelet cross-power spectrum of $\widetilde{n_e}$ and $\widetilde{B}$ with RMP (20.5∼23.5 ms). (f) Wavelet cross-power spectrum of $\widetilde{n_e}$s from probes 1 and 3 with RMP (20.5∼23.5 ms).

cross-power around the frequency of 36 kHz at 14.4 ms in Figure 6.14(c). But the density fluctuations cross-power of the up and down probes' signals has a different characteristic oscillation frequency of 23 kHz at 14.5 ms, as shown in Figure 6.14(d). Apparently those two peaks are independent activities, and the lower frequency one may be GAM.

(2) During the RMP pulse(20.5-23.5 ms), the MHD instabilities and density fluctuations cross-power spectrum peak frequency drops to 25 kHz at 21 ms, as shown in Figure 6.14(e). It is mainly because the MHD instabilities characteristic frequency drops to 25 kHz as discussed in Figure 6.12 before. However, the density fluctuations cross-power of the up and down probes(p1 and p3) doesn't have a similar frequency peak in Figure 6.14(f). It indicates that the 25 kHz MHD activities have no effect on the edge plasma density fluctuations.

(3) There is another 23 kHz frequency peak at about 23 ms in the density fluctuations cross-power spectrum of the up and down probes during the RMP pulse, as Figure 6.14(f), while the cross-power spectrum of $\widetilde{n_e}$ and $\widetilde{B}$, as Figure 6.14(e), has the same feature. Therefore, such low frequency density fluctuations may be related to the low frequency magnetic field fluctuations.

The similar features can be found in the density and magnetic fluctuations when the trident probe array is at r=12.5 cm. Based on the above relationship of MHD activities with the density fluctuations found in RMP experiments, it may be confirmed that the around 20 kHz low frequency density fluctuations found in previous experiments are not related to the low frequency($\leq$25 kHz) MHD activities. In other words, GAM may exist in STOR-M, and its characteristic frequency is about 20$\sim$23 kHz at the STOR-M edge region r=12$\sim$12.5 cm ($\rho \simeq 0.92 \sim 0.96$).

CHAPTER 7

CONCLUSIONS AND FUTURE WORK

7.1 Conclusions

The focus of this thesis is to revisit GAM theory and to carry out experiments in the STOR-M tokamak to identify GAM. Experimental studies show GAM has only been observed in the tokamak edge area, which is not predicted in Winsor's classical GAM model. At the tokamak edge region, the perturbed parallel current $J_{\|}$ is not negligible, and the key cross-field charge neutrality condition $\nabla \cdot \mathbf{J}_{\perp} = 0$ in Winsor's model becomes questionable as a consequence. Therefore, in the theory part of this thesis, the electromagnetic two fluid analysis is applied to GAM first as Ref. [37], and it is found that GAM couples with Alfvén mode and tends to stabilize the ballooning mode. The coupling between the electromagnetic GAM and Alfvén oscillations has already been investigated earlier in theory [28]. To explain the established GAM experimental results, a resistive GAM theory is developed using the resistivity condition in the plasma edge. In this theory, electron collision rate is implemented into two-fluid analysis and the gyro-kinetic formulation in the tokamak geometry, and a resistive GAM dispersion relationship is derived as a result. This theory predicts that the plasma resistivity can kill the parallel net current caused by the geodesic plasma compressibility in tokamak. Such a mechanism satisfies the cross-field charge neutrality condition, and Winsor's classical GAM model becomes logical on this premise. This also explains the fact that GAM exists in the resistive region in a tokamak. Therefore the resistive GAM theory is more plausible than Winsor's classical GAM theory.

Following this theory, some experiments are performed to search for the resistive GAM in the STOR-M tokamak edge plasma. Triple probes and single biased probes are used to measure the local plasma density n_e or the ion saturation current I_{is} and electron temperature in the STOR-M

edge plasma. A ring probe array and a trident probe array are designed to measure the poloidal and radial profiles of density fluctuations in the STOR-M tokamak edge region during the L-mode discharges and during the RMP phase. Some encouraging and interesting results are found as described below:

(1) According to the FFT and wavelet analyses, the signals of up($\theta = 90°$) and down($\theta = -90°$) probes in the ring probe array yield GAM-like peaks around 20 kHz in the ion saturation current (plasma density) fluctuations during the L-mode discharges. This frequency matches the resistive GAM theory predictions for the edge plasma parameters ($n_e \simeq 0.4 \times 10^{12}$ cm^{-3}, $T_e \simeq 20$ eV) at the radial position $r = 12$ cm. The power spectrum of magnetic fluctuations have peak at a higher frequency range 25$\sim$40 kHz. However, the phase of the cross-power of the up and down probes doesn't reveal the predicted anti-phase feature based on the GAM's theory.

(2) In L-mode discharges, similar GAM-like peaks are also found at about 20$\sim$23 kHz in plasma density fluctuations measured by the movable trident probe array. Depending on the radial position of the trident probe, those frequencies are different from the main MHD fluctuation frequency, 15$\sim$40 kHz.

(3) Changing the radial position of the trident probe array, the GAM-like features only clearly appear within r=12$\sim$12.5 cm. Outside this region, there are no clear GAM-like peaks in the spectra of density fluctuations, and the peaks of similar amplitudes are more randomly distributed.

(4) In the L-mode discharges when the RMP is applied, the dominant MHD fluctuation frequency appears around 25 kHz, which is very close to the measured GAM-like frequency. A detail comparison between the density fluctuations and magnetic fluctuations wavelet spectra suggests that the low frequency MHD fluctuations and the low frequency density fluctuations are not strongly correlated.

In summary, resistive GAM theory predicts that the GAM can only appear in the tokamak edge collisional plasma. GAM phenomena are identified experimentally in the r=12$\sim$12.5 cm range during the STOR-M L-mode discharges. The observed characteristic frequencies of the density fluctuations appears to be consistent with the resistive GAM theoretical predictions. However, the experimental results didn't confirm the $m = 1$ poloidal mode structure for the density fluctuations, which leaves room for further theoretical and experimental investigations of the GAM phenomena.

7.2 Future Work

In this thesis, GAM is studied theoretically and positive experimental identification of GAM in the STOR-M tokamak is made. The observed characteristic frequencies of the GAM in STOR-M agree with the resistive GAM theory prediction. However, some further clarifications are needed in the future experiments.

Firstly, most of the probes in the ring probe probes burn out before the actual experiment starts, and the mode analysis using the remaining probes was unable to verify the theoretical prediction of $m = 1$ poloidal mode structure for GAM. However, recent results from the correlative reflectometry measurements in T-10 didn't produce the $m = 1$ structure neither [46]. More experiments are needed to confirm the mode structure of GAM. Improving the signal-noise ratio, using more advanced and accurate diagnostic tools and getting more accurate plasma magnetic field mode structure will help to improve the credibility of the observed mode structure. On the other hand, the theory reinvestigation and simulations are also needed to confirm the actual mode structure of GAM under a wider range of plasma parameters.

Secondly, the GAM phenomena are found in the r=12$\sim$12.5 cm edge region in the 20$\sim$23 kHz frequency range using the trident probe array. However, the array is unfortunately restricted by the limited available ports to locate at the midplane of the chamber. This position is supposed to have the weakest GAM oscillations in the density fluctuations, which may have potentially reduced the possibility to find the GAM. More experiments are definitely needed to measure the density fluctuations at the poloidal positions where GAM is stronger ($\theta = \pm 90^{\circ}$).

The experimental work in this thesis concentrates on investigating the poloidal distribution of density fluctuations to search for GAM. Further experiments to identify the toroidal GAM mode by measuring density fluctuations and plasma potential fluctuations can be carried out in STOR-M. It will also provide a more clear picture of the GAM mode structure and the underlying physical mechanism.

More theoretical and experimental investigations of plasma turbulences and fluctuations can be carried out in the future to solve the jigsaw puzzle of GAM's interactions with other physical processes in the tokamak edge plasma. This includes examination of GAM's role in the edge plasma transport, as well as its effects on other instabilities in tokamak.

REFERENCES

[1] Jordan Edwin Morelli. *Plasma Position Control in the STOR-M Tokamak: a Fuzzy Logic Approach*. PhD thesis, University of Saskatchewan, 2003.

[2] W. Zhang. *Improved Ohmic Confinement Induced by Turbulent Heating and Electrode Biasing in the STOR-M Tokamak*. PhD thesis, University of Saskatchewan, March 1993.

[3] C. Xiao and *et al.* Design and Initial Operation of Multichord Soft X-ray Detection Arrays on the STOR-M Tokamak. *Rev. Sci. Instrum.*, 79:10E926, 2008.

[4] D. Rohraff. Ion Temperature Measurements in STOR-M Boundary Plasma Using a Retarding Field Energy Analyzer. Master's thesis, University of Saskatchewan, 2009.

[5] K. M. Hthu. Edge Ion Temperature Measurement in the STOR-M Tokamak. Master's thesis, University of Saskatchewan, 2012.

[6] G.M. McCracken and P.E. Stott. *Fusion: The Energy Of The Universe*. Complementary Science Series. Elsevier Academic Press, 2005.

[7] European Commission. Directorate-General for Research Fusion Energy Research. *Fusion Research: An Energy Option for Europe's Future*. Office for official Publications of the European Communities, 2005.

[8] C.R.Nave. Hyperphysics. http://hyperphysics.phy-astr.gsu.edu/hbase/hph.html, 2005.

[9] Fusion For Energy. What is Fusion? http://fusionforenergy.europa.eu/understandingfusion/, 2012.

[10] International Energy Agency (IEA). Nuclear Fission and Fusion. http://www.iea.org/topics/nuclearfissionandfusion/, 2012.

[11] European Fusion Development Agreement (EFDA). Progress in Fusion. http://www.efda.org/2011/09/progress-in-fusion/?view=gallery-273, 2011.

[12] European Fusion Development Agreement (EFDA). Larmor Movement Inside the Plasma. http://www.efda.org/newsletter/efda-during-fp7-reinforced-coordination-of-physics-and-technology-in-eu-laboratories-part-3/, 2011.

[13] R. Snurr, D. Freude. Energy Fundamentals, 2011.

[14] JT-60U Team. JT-60U Experimental Report No. 46. Technical report, JAEA, August 1998.

[15] M. Kruskal and J. L. Tuck. The Instability of a Pinched Fluid with a Longitudinal Magnetic Field. *Proc. R. Soc. Lond. A*, 245(1241):222–237, 1958.

[16] R. J. Goldston. Scientific Progress in Magnetic Fusion, ITER, and the Fusion Development Path. Technical report, SLAC Colloquium, April 2003.

[17] N. Winsor, J. L. Johnson and J. Dawson. Geodesic Acoustic Waves in Hydromagnetic Systems. *Phys. Fluids*, 11:2448 – 2450, 1968.

[18] Z. Lin and *et al.* Turbulent Transport Reduction by Zonal Flows: Massively Parallel Simulations. *Science*, 281(5384):1835–1837, 1998.

[19] Z. Lin and *et al.* Gyrokinetic Simulations in General Geometry and Applications to Collisional Damping of Zonal Flows. *Phys. Plasmas*, 7(5):1857–1862, 2000.

[20] A. V. Melnikov and *et al.* Investigation of Geodesic Acoustic Mode Oscillations in the T-10 Tokamak. *Plasma Phys. Control. Fusion*, 48(4):S87, 2006.

[21] G. D. Conway and *et al.* Mean and Oscillating Plasma Flows and Turbulence Interactions across the L-H Confinement Transition. *Phys. Rev. Lett.*, 106:065001, Feb 2011.

[22] V. B. Lebedev and *et al.* Plateau regime dynamics of the relaxation of poloidal rotation in tokamak plasmas. *Phys. Plasmas*, 3:3023, 1996.

[23] P. H. Diamond and *et al.* Zonal Flows in Plasma-a Review. *Plasma Phys. Control. Fusion*, 47(5):R35–R161, 2005.

[24] Jeff Candy and Ron Waltz. Visualizations of Turbulence in a Tokamak are From Simulations by GYRO. General Atomics, 2004.

[25] DIII-D groups. Energy Production and End-Use Technologies. *ORNL Review*, 30(12), 1997.

[26] N.Miyato and *et al.* Global Structure of Zonal Flow and Electromagnetic Ion Temperature Gradient Driven Turbulence in Tokamak Plasmas. *Phys. Plasmas*, 11:5557, 2004.

[27] H. Sugama and T.-H. Watanabe. Collisionless Damping of Geodesic Acoustic Modes. *J. Plasma Physics*, 72:825, 2006.

[28] A. I. Smolyakov and *et al.* Kinetic Theory of Electromagnetic Geodesic Acoustic Modes. *Plasma Phys. Control. Fusion*, 50(11):115008, Oct 2008.

[29] H. Grad and H. Rubin. Hydromagnetic Equilibria and Force-Free Fields. In *Proceedings of the Second United Nations International Conference on the Peaceful Uses of Atomic Energy*, volume 31, pages 190–197, 1958.

[30] V.D. Shafranov. Plasma Equilibrium in a Magnetic Field. *Reviews of Plasma Physics*, 2:103, 1966.

[31] F. Troyon and *et al.* MHD-Limits to Plasma Confinement. *Plasma Phys. Control. Fusion*, 26:209, 1984.

[32] A. Hirose. *MHD Equilibrium and Stability*. Lecture Notes, 2006.

[33] A. Hirose, L. Zhang and M. Elia. Higher Order Collisionless Ballooning Mode in Tokamaks. *Phys. Rev. Lett.*, 72:3993–3996, 1994.

[34] J. P. Freidberg. *Ideal Magnetohydrodynamics*. Plenum Press, 1987.

[35] E. J. Strait and *et al.* Resistive Wall Mode Stabilization with Internal Feedback Coils in DIII-D. *Phys. Plasmas*, 11:2505, 2004.

[36] M. Okabayashi and *et al.* Stabilization of the Resistive Wall Mode in DIIIŰD by Plasma Rotation and Magnetic Feedback. *Plasma Phys. Control. Fusion*, 44:B339, 2002.

[37] A.Hirose and J. Weiland. Two-fluid Analysis of the Geodesic Acoustic Mode in Tokamaks. *AIP Conf. Proc.*, 1382:67972, Oct 2011.

[38] A. Hirose, L. Zhang and M. Elia. Ion Temperature Gradient-driven Ballooning Mode in Tokamak. *Phys. Plasmas*, 2:859, March 1995.

[39] A. Hirose, T. L. Kroeker and O. Ishihara. Resistive Boallooning Mode in Tokamaks. *Can J. Phys.*, 66:1069, May 1988.

[40] W. Zhang and *et al.* Control of the Floating Potential Fluctuations via Limiter Biasing in the Saskatchewan Torus-Modified (STOR-M) Tokamak. *Phys. Plasmas*, 1(11):3646, 1994.

[41] L. Spitzer. *Physics of Fully Ionized Gases*. New York: Interscience, 2nd edition, 1962.

[42] A. Nagashima and *et al.* A 2-mm Wave Digital Interferometer for Tokamak Discharges in the Upgraded DIVA. *Jpn. J. Appl. Phys.*, 17(7):1263–1270, July 1978.

[43] F. F. Chen. *Introduction to Plasma Physics and Controlled Fusion*. Springer, 2nd edition, 1984.

[44] K. Ohkuni and *et al.* Langmuir Probe Array for Edge Plasma Study on the Compact Helical System Heliotron/Torsatron. *Rev. Sci. Instrum.*, 70(1):419, Jan. 1999.

[45] M. A. Lieberman and A. J. Lichtenberg. *Principles of Plasma Discharges and Materials Processing*. Wiley-Interscience, 2nd edition, 2005.

[46] D.A. Shelukhin and *et al.* Spatial Structure of Density Fluctuations and Geodesic Acoustic Mode in T-10 Tokamak. *22nd IAEA Fusion Energy Conference*, 2008.